NTNU
Norwegian University of
Science and Technology

Master's thesis

2020

Fabian Skarboe Rønningen

Master's thesis

NTNU
Norwegian University of
Science and Technology
Faculty of Information Technology and Electrical
Engineering
Department of Electric Power Engineering

Fabian Skarboe Rønningen

Impedance-Based Stability Analysis and Adaptive Control of Grid-Connected Converter

June 2020

NTNU
Norwegian University of
Science and Technology

NTNU
Norwegian University of
Science and Technology

Impedance-Based Stability Analysis and Adaptive Control of Grid-Connected Converter

Fabian Skarboe Rønningen

Energi og Miljø
Submission date: June 2020
Supervisor: Prof. Olimpo Anaya-Lara
Co-supervisor: Dr. Raymundo Torres-Olguin

Norwegian University of Science and Technology
Department of Electric Power Engineering

Abstract

Over the last several decades, the penetration of power electronics connected to the grid has increased dramatically, and the trend is expected to further accelerate in the years to come. The main reason is the increased integration of renewable energy sources, as the majority are connected to the grid through power electronic converters due to the converter's ability to transform the energy from the source to a suitable form for injection to the power grid. The resulting impact in mitigating climate change problems is expected to be enormous, and it means that both generation and transmission, but also the consumers, are increasingly dependent on the power electronics technology. Accordingly, as the number of grid-connected converters continues to increase, so will its impact on power system dynamics and stability. Recently there have been several unexpected events of instability in power electronics dominated grids, apparently due to resonance between the converters and the grid. Therefore, to ensure the continued integration of renewable energy sources, the instability problems should be analyzed, and measures should be taken to avoid similar instability problems in the future.

There are several ways to assess the stability of the interaction between the grid and the converter, and one of them is the so-called small-signal impedance-based stability method, which is studied in this thesis. The first part of this thesis is dedicated to developing appropriate models for a specific converter, and the grid, so that this method can be applied. Then follows the main contributions of this thesis, two novel adaptive control methods based on changing the control parameters for the current controller and the phase-locked loop depending on the grid impedance. After the necessary methods were developed, they were implemented in simulation.

The simulation software Matlab was first used to implement the converter and grid models, then the adaptive control methods. The result of the first method, which only adapts the phase-locked loop parameters, proved to be effective in increasing the stability limit compared to other static methods. However, it also showed poor behavior under certain grid conditions, even compared to simple static methods. The second method adapted both the phase-locked loop and the current controller, and the implementation proved to be superior to all other static and adaptive methods tested. Finally, both of the methods were implemented in the time-domain in form of a Simulink model. In general, the results from the small-signal model translated well to the Simulink model, and also in this case, the second adaptive control method was highly effective under all grid conditions, until the stability limit was reached.

Sammendrag

De siste tiårene har andelen av kraftelektronikk tilkoblet strømnettet økt drastisk, og denne trenden er forventet å fortsette i årene som kommer. Hovedårsaken til er dette er den økte integrasjonen av fornybare energikilder, siden mesteparten av disse kildene er koblet til strømnettet via kraftomformere. Kraftomformerne har den egenskapen at de kan transformere energien til en passende form for innmating i strømnettet. Resultatet av dette for å bremse klimaendringer er forventet å være enorm, og det betyr at både produksjon og overføring, men også sluttforbrukere, er mer avhengige av kraftelektronikkteknologi. Samtidig som andelen nett-tilkoblede omformere fortsetter å øke, vil innvirkningen på strømnettets dynamikk og stabilitet påvirkes i større grad enn før. De siste årene har det vær flere uforutsette hendelser tilknyttet ustabilitet i kraftelektronikk-dominerte strømnett, tilsynelatende grunnet resonans mellom omformeren og strømnettet. For å sørge for en fortsatt integrasjon av fornybare energikilder, må disse problemene studeres nøyere, og passende tiltak må iverksettes for å unngå tilsvarende stabilitetsproblemer i fremtiden.

Det er mange måter å evaluere stabiliteten i interaksjonen mellom strømnettet og omformeren, og en av dem er den såkalte små-signal impedans-baserte stabilitetsmetoden, som er anvendt i denne oppgaven. Første del av oppgaven er derfor dedikert til å utvikle modeller for en spesifikk kraftomformer, og strømnettet, så denne metoden kan bli brukt. Deretter følger hovedbidraget i denne oppgaven, to nye adaptive kontrollmetoder som er basert på å endre kontrollsparemeterne for strømkontrolleren og fase-synkroniserings-kontrolleren basert på impedansestimatet av strømnettet. Etter metodene var utviklet ble de implementert som simuleringer.

Simuleringsverktøyet Matlab ble først brukt til å implementere omformer og strømnett modellene, og så de adaptive kontrollmetodene. Resultatet av den første metoden, som kun endret parameterne i fase-synkroniserings-kontrolleren, viste seg å være effektiv i å øke stabilitetsgrensen for systemet, sammenlignet med andre statiske kontrollmetoder. Men kontrolleren viste dårlig dynamisk ytelse under visse forhold. Den andre metoden endret både fase-synkroniserings-kontrolleren og strømkontrolleren, og resultatet viste seg å være bedre enn alle andre statiske og adaptive metoder den ble sammenlignet med, når det kom til dynamisk ytelse. Til slutt ble begge metodene implementert i tids-domene i form av en Simulink modell. Konklusjonen var at resultatet fra små-signal modellen kunne overføres til Simulink modellen. Også i dette tilfelle viste den multivariable adaptive kontrollmetoden seg i å være overlegen de andre metodene under alle forhold, helt til stabilitetsgrensen var nådd.

Preface

This Master's thesis was conducted at the Department of Electrical Power Engineering under the Faculty of Information Technology and Electrical Engineering at the Norwegian University of Science and Technology and in collaboration with SINTEF Energy Research in connection with the CINELDI project.

I would like to thank my supervisor Prof. Olimpo Anaya-Lara and co-supervisor Dr. Raymundo E. Torres-Olguin whose expertise and guidance made this thesis possible, and all their time and effort in helping me solve big and small problems during the work of this thesis. I would also like to thank Mr. Fredrik T.B.W Göthner for valuable programming help.

Trondheim, June 2020
Fabian Skarboe Rønningen

Table of Contents

List of Tables

List of Figures

Abbreviations

AC = Alternating Current
APPC = Adaptive Pole Placement Control
CC = Current Controller
DC = Direct Current
DG = Distributed Generation
FACTS = Flexible Alternating Current Transmission System
GNC = Generalized Nyquist Criterion
HIL = Hardware-in-the-Loop
HVDC = High Voltage Direct Current
IGBT = Insulated-Gate Bipolar Transistor
KCL = Kirchhoff's Current Law
KVL = Kirchhoff's Voltage Law
LHP = Left Half Plane
MLBS = Maximum Length Binary Sequence
MIMO = Multiple Input Multiple Output
NSGL = National Smart Grid Laboratory
NSC = Nyquist Stability Criterion
PRBS = Pseudo-Random Binary Sequence
PCC = Point of Common Coupling
PEC = Power Electronic Converter
PLL = Phase-Locked Loop
PV = Photovoltaic
PWM = Pulse Width Modulation
RES = Renewable Energy Sources
RHP = Right Half Plane
RVCP = Real Value of Critical Pole
SCR = Short Circuit Ratio
SG = Synchronous Generator
SISO = Single Input Singe Output
SNR = Signal-to-Noise Ratio
SPWM= Sinusoidal Pulse Width Modulation
WTV = Weighed Threshold Variable
2L-VSC = Two-Level Voltage Source Converter

Chapter 1

Introduction

The first chapter of this thesis serves as an introduction to the work done. First, the background for the thesis is explored, followed by the objectives and scope of the thesis. Lastly, sections on work methodology and thesis structure are presented.

1.1 Background

Over the last several decades, the penetration of power electronics connected to the grid has increased dramatically [1], and the trend is expected to further accelerate in the years to come [2]. The main reason for this is the increased integration of renewable energy sources, as the majority of them are connected to the grid through power electronic converters [3], due to the converter's ability to transform the energy from source to a suitable form for injection to the power grid. The resulting impact in mitigating climate change problems is expected to be enormous, and it means that both generation and transmission, but also the consumers, are increasingly dependent on power electronics technology. Accordingly, as the number of grid-connected converters continues to increase, so will its impact on power system dynamics and stability. Therefore, it is of great interest and importance to study the impact of increased power electronics integration.

Not only will the future grid most likely be power electronics dominated, but there will also be a shift from centralized to distributed generation [4]. This shift is another contribution to increased system dynamics, which requires the converters to operate under many different grid conditions. Converters often have a high level of controllability, and generally a fast response to system dynamics, which is a benefit when dealing with a wide range of different grid conditions. However, there have been unwanted effects related to instability of operation for grid-connected converters, for example, in wind power systems [5] and photovoltaic systems [6] [7]. Dynamics and stability of power electronic converters will also play a considerable factor for applications such as High Voltage Direct Current systems (HVDC), Battery Energy Storage Systems (BESS), Vehicle-to-grid (V2G) applications and Flexible Alternating Current Transmission System (FACTS) [2]. Power quality and stability problems for grid-connected converters have become a serious concern in the field of power electronics [8], and it has been suggested in the literature that the cause of this instability often can be related to the resonance between the converters and the grid. One promising method to study this interaction is the use of impedance-based modeling, first suggested for grid-connected converters in [9], and later expanded greatly. This research area has been subject to increased interest over the last years [1], and will be further studied in this thesis.

Power electronics converters can be represented by their small-signal impedance equivalents [10], and if the converter is modeled by its small-signal equivalent impedance, and the grid impedance is estimated, relations between these two parameters can be obtained and related to stability. There are several advantages to this approach, for example:

- Impedance-based stability assessment is well suited for a distributed control system, which matches the trend from the last paragraph.
- Suitable for real-time applications, as methods for real-time impedance estimation, has become more available in the last years [11], and the converter impedance can be modeled directly.
- Lower computational burden compared to many other methods [8].
- Facilitates plug-and-play capabilities, as the stability assessment and control can be performed locally in the converter control system.
- Suitable in the case of islanded microgrids.

Moreover, as the grid impedance varies considerably during a day [12], the use of grid impedance estimation is an excellent opportunity for adaptive control based on the real-time grid impedance estimate. It has been shown, for example in [13], that adapting the PLL bandwidth based on the grid impedance can extend the stability limit of the system. If the converter is current-controlled, it has also been shown that the current controller can be adapted based on the grid impedance [14]. Accordingly, this thesis will aim at developing adaptive control methods based on converter and grid impedance models.

Before impedance-based stability analysis and eventual adaptive control can be explored, a specific converter has to be selected, and for this thesis, the Two-Level Voltage Source Converter (2L-VSC) is selected. This converter is used over a wide range of applications, mainly due to its capability for bidirectional power flow and possible implementation of high-performance control systems in forms of current, voltage, and power control [14]. Therefore, this converter is considered to have an important role in maintaining the safe, stable and high-quality operation of renewable energy-based distributed power generation [15], both today and in the future.

Furthermore, previous results [16] indicated that Single Input Single Output (SISO) converter and grid models were inadequate to capture the effect grid impedance and PLL dynamics had on system stability. This naturally also means this cannot be used for any adaptive control since the system modeling is not accurate enough. Results from the literature [13] showed that only when a detailed Multiple Input Multiple Output (MIMO) converter model was created, the underlying reason for why the PLL introduces stability problems appears, therefore this will be done in this thesis. First, when an accurate model is developed, simulated, and verified to represent a real system accurately, adaptive PLL control can be explored. Since the PLL is not the only controller in the grid-connected converter in this thesis, also an attempt to implement general multivariable adaptive control where all control parameters are included will be investigated.

1.2 Objectives

The main objective of this thesis is to develop adaptive control methods for the grid-connected 2L-VSC, based on the small-signal impedance-based converter and grid models. Extra emphasis will be on system simulation to uncover the underlying dynamics. Secondary objectives include:

- Examine theoretical results from the literature for SISO and MIMO modeling of the 2L-VSC connected to the grid with LCL-filter.
- Examine the literature for stability criteria and find a fitting one for the developed converter models, and that can be used directly for developing a novel adaptive control method.
- Examine the literature for possible methods for grid impedance estimation and suitability for real-time implementation.
- Develop an adaptive control method for the PLL based on changing grid impedance. Use the knowledge gained to develop a more general multivariable adaptive control algorithm where all relevant control parameters in the converter are taken into account, not just the PLL.
- Implement the developed method in a simulation environment suitable for implementation in a laboratory environment at the National Smart Grid Laboratory (NSGL) operated by NTNU and SINTEF Energy Research in Trondheim, Norway.
- If time and other factors allow, implement the methods in a laboratory environment.

1.3 Scope

To achieve the objectives defined in the last section, certain limitations must be established. The following list is will serve as the scope of this thesis.

- The 2L-VSC is the only considered converter in this thesis. Furthermore, the converter is modeled as an average model, which limits the frequency range of interest.
- The only considered grid filter is the LCL-filter, mainly because this is the filter in the laboratory setup in the NSGL, but also because this is the most common solution is similar studies from the literature, and it is common in the industry [15]. No active damping methods for the LCL-filter will be considered.
- The only considered grid synchronization method is the Synchronous Rotating Frame Phase-Locked Loop (SRF-PLL).
- The converter is operated in current-controlled mode in the dq-frame. The control parameters in the d-frame will always be the same as the q-frame, for simplicity. No DC-side outer voltage control loop is considered. No power control is considered either, and the converter only injects active power to the grid, when in steady-state. The converter will operate in inverter mode for the entirety of the thesis. No specific application like solar of wind will be considered.
- The grid impedance estimation part itself will not be a major objective in this thesis. Therefore, any modeling or simulation that needs the grid impedance estimate, it is assumed to be accurate and available. However, a brief description of the different methods will be presented, and the selected method for eventual laboratory implementation is described in Appendix J.
- Under changing grid impedance, it is assumed that it is mainly the grid inductance that changes. For an explanation for why this is chosen, see Appendix B.4.
- In all simulations considered, one specific system will be studied. This is considered the base-case, and it is set to closely resemble one of the existing laboratory setups at the NSGL operated by NTNU and SINTEF Energy Research. However, the control system for this setup will naturally be developed in this thesis. For details on this specific laboratory setup, and base-case control parameters, see Appendix G.

- A formal theoretical foundation of the adaptive control developed in this thesis is beyond the scope.

1.4 Methodology

As already implicitly presented earlier in the introduction, the development of the adaptive control methods will be done in an iterative approach, where possible strengths and weaknesses from the first adaptive method will be directly used in the second, more general method, if time and other factors allow. To summarize, the list below illustrates the general logic workflow of this thesis, and correspond to how the novel adaptive control methods are developed.

- Literature review on SISO and MIMO converter and grid modeling methods, and picking the methods that fit the small-signal impedance-based stability method.
- Base simulations to verify that the developed converter and grid models have a proper initial operation, before any stability analysis or adaptive control can be implemented. Also, ensure that a working representation without numerical errors and loss of relevant system dynamics are chosen, but at the same time have as simple models as possible. All this is covered in Appendix D.3 and D.4.
- Use of the small-signal impedance-based stability method, with modifications if necessary, to obtain a baseline for developing novel adaptive control methods.
- Develop the adaptive PLL method, implement this method, and use the results strengths and weaknesses to develop a more general multivariable adaptive control method.
- If time and other factors allow, implement the methods on a hardware-in-the-loop (HIL) laboratory environment at the NSGL. Compare the simulation results with the laboratory implantation. (NOTE: NSGL was closed from March to June 2020, which made any experimental verification impossible).
- Discuss the developed models and control methods and present possible further work.

1.5 Thesis Structure

This thesis is divided into five main chapters, where the first chapter serves as an introduction.

Chapter 2 covers the small-signal impedance-based methodology first, followed by sections on SISO and MIMO converter and grid models. Then, the relevant stability criterion is presented, which serves as a foundation for the adaptive control methods to be implemented later. This chapter is also supplied heavily by appendices because much of the underlying theory is not the main focus for this thesis, but still important. Therefore, Appendix A-E serves as the backbone of this chapter, and will be referred to when necessary. Appendix J, which covers grid impedance estimation methods, is also considered a supporting appendix for this chapter, since this topic is important for the stability criterion, but not considered a main objective.

Chapter 3 covers the main contribution of this thesis, where first the general adaptive control methodology is presented, followed by two sections, where the first one covers adaptive PLL control and the second covers multivariable adaptive control. This is naturally followed by an implementation in the form of a simulation of the developed adaptive control methods in Chapter 4 where first the methods are implemented, and later time-domain simulations are implemented to verify the adaptive controllers in the time-domain.

Chapter 5 is the final main chapter of this thesis, where results are discussed and concluded, before possible further work is presented.

After this follows the supporting appendices for this thesis, which is selected to be quite detailed to meet all the objectives defined earlier, and make this thesis as complete as possible, without losing the red line in the main part of the thesis. The appendices will be referred to when necessary during the whole main part of this thesis.

Chapter 2

Impedance-Based Modeling and Stability Analysis

This chapter considers the main theoretical foundation of this thesis, first impedance-based converter and grid modeling, and after that, the stability analysis.

Section 2.1 briefly presents the selected method and its advantages to model the problem at hand. Section 2.2 introduces the concept of the impedance-based stability criterion and applies it directly to the system under study. Section 2.3 is the most important part of this chapter, where the MIMO converter and grid models that will be used for the entirety of this thesis are derived and presented before the stability criterion is used. Section 2.4 elaborates on the system representation that will be used in the rest of the thesis, as this has to be clarified for further work.

2.1 Small-Signal Impedance Method

This section introduces the selected modeling method, namely the small-signal impedance method. The section is kept brief, for compactness, and if the reader is interested, Appendix C considers both the small-signal method in general, as well as the fundamentals of impedance-based analysis. As explained in the introduction, this thesis is concerned with a specific converter, in particular, and the background theory on this converter, and its operation, is considered in Appendix B.

As briefly mentioned in the introduction, there are many ways to assess the stability of a dynamical system. To guide the further discussion on which method is appropriate for this thesis, consider the illustration in Figure 2.1, that shows different power system stability methods, and highlights the important categories for this thesis.

In general, power electronics systems are non-linear time-varying systems. To tackle the nonlinearities introduced by the switching dynamics in the converter, the first choice in this thesis is to have an average model of the converter. Having an average model implies that the response over one switching period is averaged. This is compared to discrete-time analysis, where the switching dynamics are modeled accurately. The obvious advantage of this choice is that the analysis gets simplified at the expense of accuracy. However, this thesis is

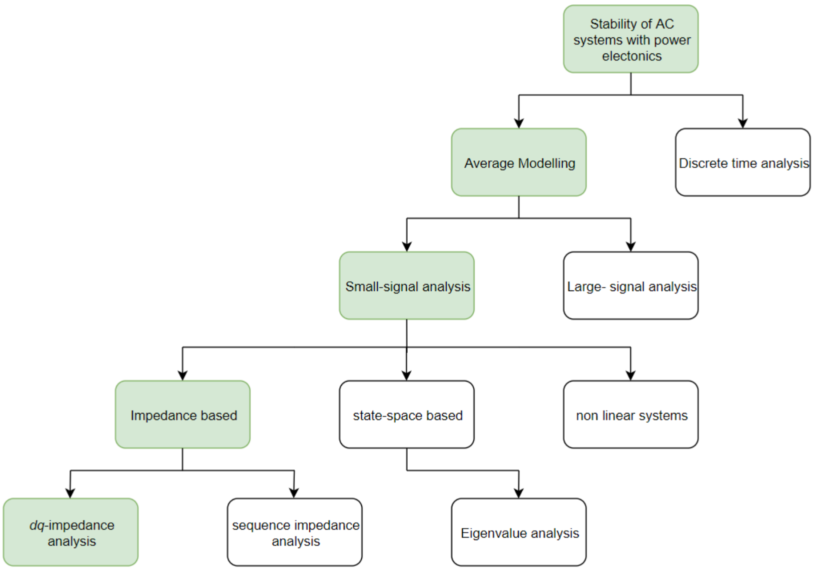

Figure 2.1: Overview of some power system stability methods, where the methods relevant for this thesis are highlighted.

concerned with frequency analysis well below the switching frequency, so the average modeling technique is preferred. Furthermore, small-signal analysis is chosen, as it is wanted to analyze the system close a certain operating point, and maintain stability when subjected to small disturbances. Other forms of power system stability, such as transients stability, sub-synchronous stability, mid-term and long-term stability will not be focused on in this thesis. Other typical power system stability measures such as voltage stability and rotor angle stability are not relevant and will not be considered either.

Small-signal analysis can be divided into many different subcategories, and in this thesis impedance-based small-signal analysis is considered. This was motivated in the introduction to the thesis, so no further elaboration will be provided here, and Appendix C is also available as background material. In [10] it was shown to great detail the similarities, differences, advantages, and disadvantages between dq-domain or the sequence domain for modeling of the converter-grid system. In this thesis, the dq-domain is chosen.

In small-signal impedance-based analysis, the term *impedance* refers to the small-signal transfer function from current to voltage [10]. Early work within the field on impedance-based analysis include [19], and today this method is a widely used technique for a range of different applications [10]. When considering impedance modeling of three-phase systems there are several complicating factors compared to a single-phase system, or a DC-system for that matter. The first factor is that a three-phase system is generally represented by 3x3 matrix equations, not like a simple scalar DC-system. Secondly, a three-phase system does not have a small-signal equilibrium point, since most of the state variables (e.g. currents and voltages) are oscillating with the fundamental frequency. Both challenges can be tackled by certain assumptions and techniques. First, it is assumed that the system is operated in balanced operation i.e. the sum of the phase currents is zero at all times. This leaves one degree of freedom, and the system dimensions can be reduced from 3x3 to 2x2. To solve the problem of oscillating state variables, a coordinate transformation can be performed. A common transformation is the abc-dq transformation, which is described in Appendix A, together with the abc-$\alpha\beta$

transformation, and therefore it is only repeated in (2.1) for completeness.

$$\begin{bmatrix} v_d \\ v_q \end{bmatrix} = \frac{2}{3} \begin{bmatrix} cos(\theta) & cos(\theta - \frac{2\pi}{3}) & cos(\theta + \frac{2\pi}{3}) \\ -sin(\theta) & -sin(\theta - \frac{2\pi}{3}) & -sin(\theta + \frac{2\pi}{3}) \end{bmatrix} \begin{bmatrix} v_a \\ v_b \\ v_c \end{bmatrix} \tag{2.1}$$

In steady-state, v_d and v_q will then be seen as DC-signals. The fact that this transformation introduces a steady-state operating point gives the possibility to apply standard control theory without further complications.

The small-signal impedance definition follows directly from considering Ohms law in the dq-domain, as shown in (2.2).

$$\begin{bmatrix} v_d \\ v_q \end{bmatrix} = \begin{bmatrix} Z_{dd} & Z_{dq} \\ Z_{qd} & Z_{qq} \end{bmatrix} \begin{bmatrix} i_d \\ i_q \end{bmatrix} \tag{2.2}$$

Naturally, v_d, v_q, i_d and i_q must also be small-signal variables for this to hold. This is also known as the generalized Ohms law, where the impedance is a 2x2 matrix, not a scalar or a complex number. To simplify notation, the impedance transfer function matrix is defined as $\mathbf{Z_{dq}}$ from now. Z_{dd} represents the voltage response in the d-channel, when the d channel current is perturbed, and Z_{qq} represents the voltage response in the q-channel, when the q channel current is perturbed [13]. The two off-diagonal elements in $\mathbf{Z_{dq}}$ represents the coupling between the two axis, i.e. if they are non-zero the two axis affects each other. What this actually means will be more clear when an actual system is modelled in the dq-domain in Subsection 2.3.1.

However, before a complete MIMO model in the dq-domain is derived, a natural starting point would be to assume that the d and q axis are completely decoupled. If that is the case, there are no dynamics between the two, and they can be studied separately. This will also make the derivation of the stability criterion much simpler. Therefore, the next section assumes that d and q axis are completely decoupled, and there are no additional dynamics that affect one channel differently than another. Then, only one channel needs to be studied, and the choice is arbitrary as the two will give the same result when all the assumptions above are used.

2.2 SISO Impedance-Based Stability Criterion

This section introduces the concept of impedance-based stability assessment in a simplified manner, specifically for the grid-connected 2L-VSC. All derivations is based on own previous work in [16] and results from the literature, mainly in [10], [11] and [18].

As mentioned in the introduction, this thesis is concerned with the stability of one converter in particular, the three-phase 2L-VSC with LCL- filter grid connection. This topology, all relevant components, and a simplified current-control structure can be seen in Figure 2.2.

The converter topology, its filter, grid synchronization mechanisms, and conventional control methods are covered in detail in Appendix B, therefore most of the background on the converter itself theory will not be repeated here. But a summary is provided below.

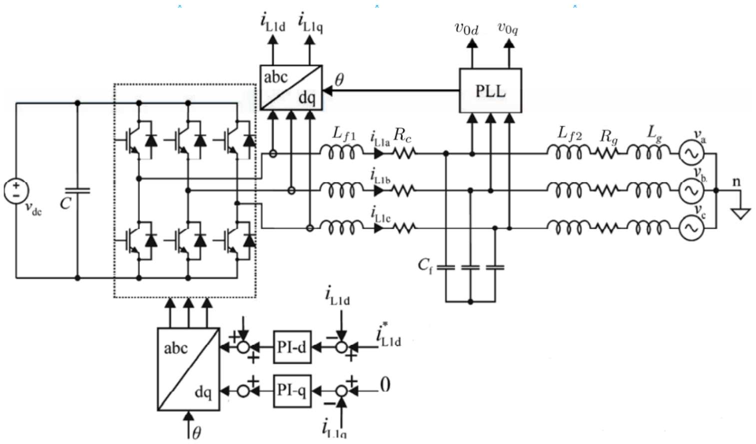

Figure 2.2: System and simplified control topology.

The DC-supply voltage source, V_{dc}, supplies a three-phase bridge structure consisting of six transistors, each with an anti-parallel diode. This naturally forms the actual converter. The converter is connected to the grid with the LCL-filter, here chosen to be represented by the first filter inductor, L_{f1}, and equivalent converter resistance, R_c, followed by the filter capacitor C_f in parallel, and the second filter inductor, L_{f2}. The grid itself is represented by a voltage source and series impedance elements L_g and R_g. Furthermore, the necessary measurements to perform dq-current control is both a current measurement and a grid voltage measurement. As described in Appendix B, there are several ways to do this, but for this thesis, the current measurement is selected to be before the filter capacitor node, seen from the converter, v_0. At this node, the voltage measurement is done, which is used by the PLL to calculate the d and q axis components of the grid voltage v_{0d} and v_{0q}, and provide a reference for the calculation of the d and q axis currents i_{L1d} and i_{L1q}. The phase reference is also needed in the $dq - abc$-transformation when the dq-domain control signals are converted back to abc domain PWM signals in the bottom of the figure. This whole process is covered more detailed in the Appendix, and other relevant details will be presented later when they are needed.

As defined in the scope, an average model of the converter is assumed, with balanced three-phase operation, so a single-phase equivalent circuit can be used to represent the same system, as shown in Figure 2.3.

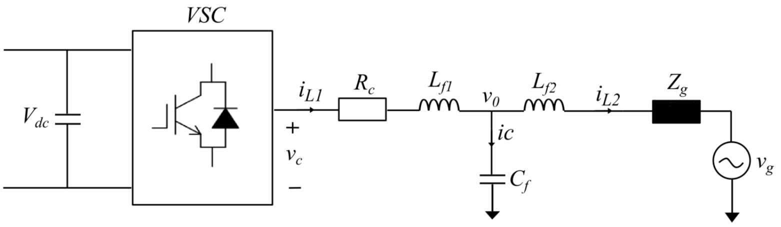

Figure 2.3: Single-phase equivalent circuit of 2L-VSC connected to the grid with a LCL-filter.

By applying Kirchhoff's Voltage Law (KVL) from the inverter terminals to the node v_0, which can be defined as the Point of Common Coupling (PCC), the relation in (2.3) is obtained. Z_{L1} is the impedance of the first filter inductor L_{f1} and the equivalent converter resistance, R_c.

$$-v_c + i_{L1}Z_{L1} + v_0 = 0 \tag{2.3}$$

To ease notation, a new variable Y_0=$\frac{1}{Z_{L1}}$ is introduced and (2.3) is solved for the injected inverter current i_{L1} in (2.4).

$$i_{L1} = Y_0 v_c - Y_0 v_0 \tag{2.4}$$

The expression in (2.4) can be represented by its equivalent block diagram in shown below in Figure 2.4.

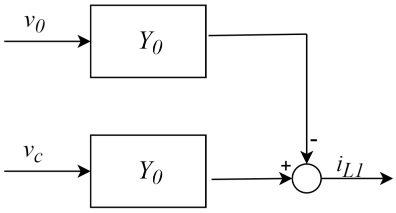

Figure 2.4: Equivalent block diagram of (2.4).

To further expand on the model, the control mode must be considered. As specified earlier, the converter is operated in current-controlled mode. In Figure 2.5 the model is further expanded by introducing the current controller block, G_{pi}, and the PWM dynamics block G_{PWM}. This approach neglects further dynamics such as PLL dynamics, outer control loops and various delays to get a simple illustration of the concept before more details are added. The input control reference in the current reference, i^*_{L1}.

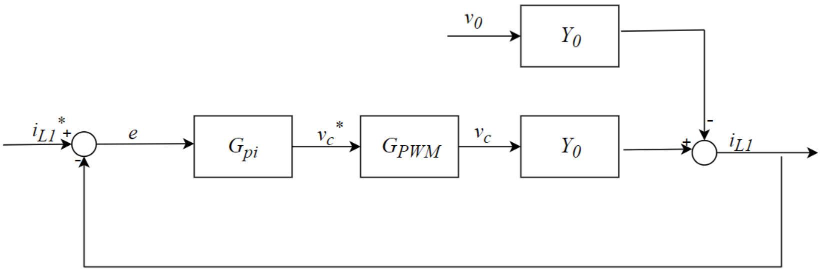

Figure 2.5: Simplified current-controlled converter equivalent block diagram.

To get a relation between the three variables of interest together, which is i_{L1}, i^*_{L1} and v_0, two new transfer functions are introduced in (2.5) and (2.6).

$$Y_{oi} = \frac{Y_o}{1 + G_{pi}G_{PWM}Y_0} \tag{2.5}$$

$$G_{cli} = \frac{G_{pi}G_{PWM}Y_0}{1 + G_{pi}G_{PWM}Y_0} \tag{2.6}$$

The interpretation of G_{cli} is the current reference-to-output transfer function, and Y_{oi} is the simplified equivalent output admittance of the converter. Now i_{L1} can be expressed in as simple way as in (2.7) and the equivalent block diagram in Figure 2.6.

$$i_{L1} = G_{cli} \cdot i_{L1}^{*} - Y_{oi} \cdot v_0 \tag{2.7}$$

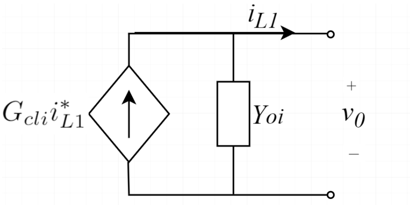

Figure 2.6: Simplified equivalent circuit of a current-controlled VSC.

Figure 2.6 represents the VSC when the PCC is set right after the first filter inductor, seen from the converter. This point is selected as the PCC for the whole thesis for consistency, and is elaborated on in Appendix B.3. The next step is to connect the VSC to the grid, and derive the stability criterion.

To derive the stability criterion, two possible approaches are illustrated in Figure 2.7. Figure 2.7a directly corresponds to Figure 2.3 earlier in this section where the two other filter components are included. In Figure 2.7b an alternative approach is taken where filter components are considered to be a part of the grid impedance. In this thesis the latter approach is taken, as the stability criterion will become slightly simpler, and also this approach is the most used one in the literature. Previous work done in [16] showed that the same stability conclusion was achieved regardless of which approach that was taken, and in fact the two methods are equivalent.

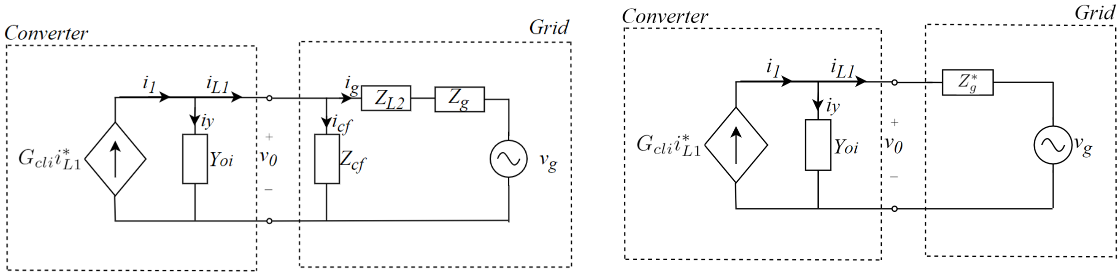

(a) Converter-grid model with filter parameters explicitly modeled.

(b) Converter-grid model with filter parameters considered as part of grid impedance.

Figure 2.7: Two different converter-grid models.

Therefore, the simplest equivalent circuit is chosen for further work. Now the goal is to link the circuit in Figure 2.7b to the Nyquist stability criterion. To get a block diagram with the variables of interest, Y_{oi}, Z_g^*, v_g, G_{cli} I_{L1} and I_{L1}^*, and remove variables not of interest, v_0, i_1, i_y, Kirchhoff's Current Law (KCL) is considered in (2.8) and relevant variables are substituted in (2.9). KVL is further considered in the right closed-loop of Figure 2.7b, to get an expression for v_0 in (2.10) and the final expression can be seen in (2.11).

$$i_{L1} = i_1 - i_y \tag{2.8}$$

$$i_{L1} = G_{cli} i_{L1}^* - Y_{oi} v_0 \tag{2.9}$$

$$v_0 = I_{L1} * Z_g^+ v_g \tag{2.10}$$

$$i_{L1} = G_{cli} i_{L1}^* - Y_{oi} i_{L1} * Z_g^* - Y_{oi} v_g \tag{2.11}$$

Moreover, (2.11) can be expressed by its equivalent block diagram, as seen in Figure 2.8.

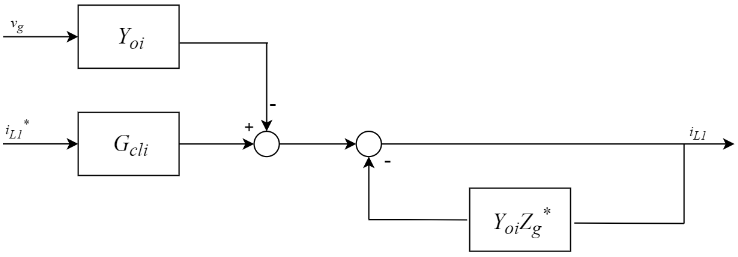

Figure 2.8: Equivalent block diagram of equation (2.11).

This block diagram can now be used to determine stability. However, some assumptions for the system needs to be made and clarified.

- *Assume that the branch $G_{cli} i_{L1}^*$ is stable.* This corresponds to assuming that the converter is stable when not connected to the surrounding grid. This would be a prerequisite, as connecting an already unstable converter to the grid makes no sense.

- *Assume that the branch $Y_{oi} v_g$ is stable.* The expression for Y_{oi} incorporates several other transfer functions as shown in (2.5), and stability may not be obvious. But as the equivalent circuit in Figure 2.3 shows, this corresponds to connecting an ideal voltage source to the terminals of the equivalent circuit and letting the current reference be zero. This would also be a prerequisite to connect to the grid in the first place, so the assumption is justified.

Now that other sources of instability are eliminated, the stability of the system in Figure 2.7b only depends on the feedback loop consisting of Y_{oi} and Z_g^*. The parts of the block diagram that is known to be stable are removed, and the simple block diagram in Figure 2.9 is the only part left.

The product $Y_{oi} Z_g^*$ is the so-called minor loop gain, and the stability of the system is governed by the interaction between the equivalent converter admittance and the grid impedance. It is further assumed that Y_{oi} and

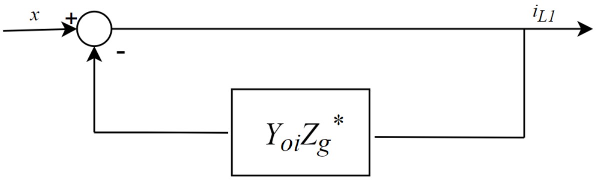

Figure 2.9: Feedback loop consisting of converter admittance Y_{oi} and grid impedance Z_g^*.

Z_g^* is stable on its own, as this corresponds to a stable grid [11]. The closed-loop transfer function, denoted L_{cl} here, is shown in (2.12). The product of Z_g^* and Y_{oi} is called L from now.

$$L_{cl} = \frac{1}{1 + Y_{oi}Z_g^*} = \frac{1}{1 + L} \tag{2.12}$$

The expression in (2.12) closely resembles the one that was used when deriving the General Nyquist stability criterion in Appendix D. For L_{cl} to be stable it cannot have any RHP poles, which will be determined when the denominator $1 + L$ is zero. As the numerator is not of importance with regards to stability, an equivalent expression for (2.12) is presented in (2.13).

$$L'_{cl} = \frac{L}{1 + L} \tag{2.13}$$

L_{cl} and L'_{cl} will have the same poles, and L'_{cl} is on the exact form used for determining stability with the Nyquist stability criterion. Therefore, with the assumptions made, the grid-connected VSC in Figure 2.7b is stable if the Nyquist plot of $Y_{oi}Z_{th}^*$ does not encircle the point (-1,0) in the complex plane. The same naturally holds if L_{cl} do not have any poles in the RHP.

This criterion is as useful as it is elegant, as stability can be directly related to only two variables, equivalent converter admittance, and the grid impedance. Now, this is only a half-truth, because the transfer function Y_{oi} is an aggregate of other transfer functions and parameters, and it is definitely not trivial to get a reliable and accurate estimate for the grid impedance. Both of these topics will naturally be explored further in this thesis.

A quick demonstration of this criterion was done in previous work in [16], and some results are highlighted in Figure 2.10. The Nyquist plots for $Y_{oi}Z_g^*$ were plotted for three different grid impedance cases, resulting in three different Nyquist plots. The pole-zero plot and step response in the injected current is also included to illustrate the relation the Nyquist curves have to other well-known tools to determine stability. It is evident that the high impedance case moves the critical poles closer to the RHP and also that the step response is slower and has higher overshoots.

This result illustrates the power of impedance-based analysis. However, previous work showed that this simple criterion fails to predict the stability limit accurately. In the figure for the ”High grid impedance” case, the models predict that the system is stable, but other more complicated switched models implemented in Simulink showed that this high grid impedance was far above the stability limit. There are several reasons why this is the case, and they will not be discussed in detail here, because the SISO criterion will not be used anyway. But for now, the most obvious reasons are all the simplifications done in the derivations, especially the assumption that the system is decoupled, and the PLL has no effects. This is inaccurate and is shown numerous times in the literature, for example in [10] and [13]. Therefore, the next section will cover

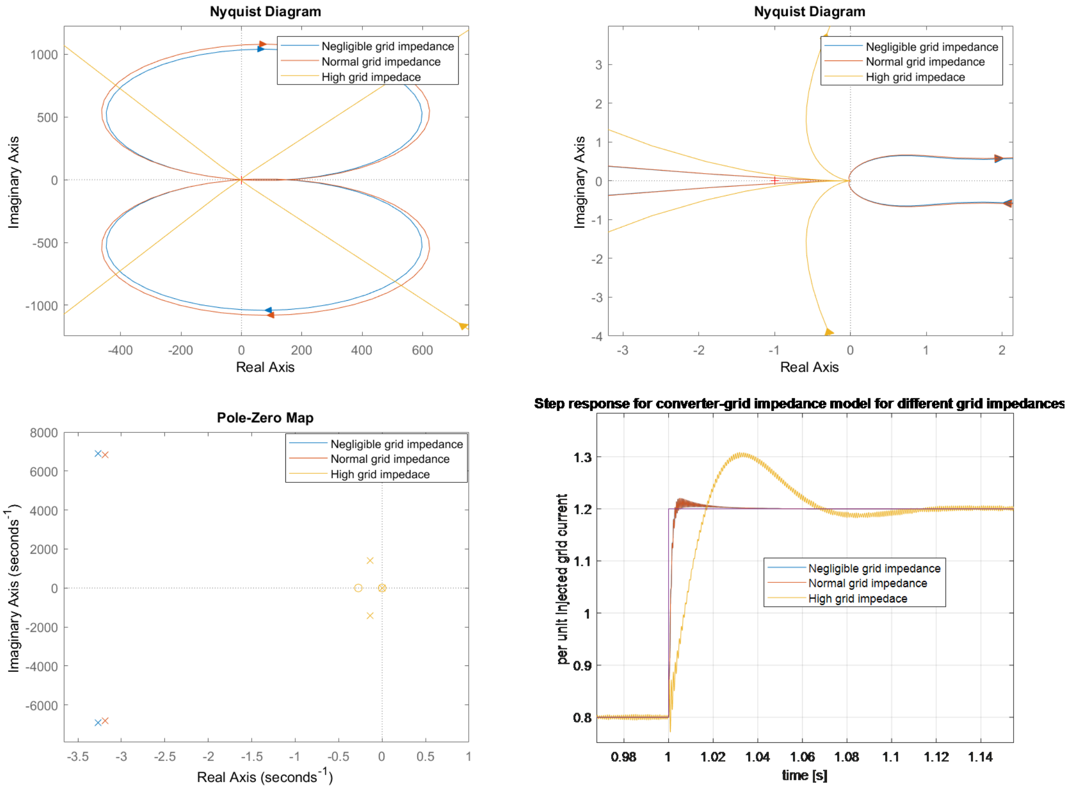

Figure 2.10: Nyquist curves, pole placement and step response for $Y_{oi}Z_g^*$ for three cases of grid impedance.

impedance-based converter modeling in a more general way, where the aim is to end up with the generalized stability criterion for the MIMO converter-grid system, where among other PLL dynamics are taken into account.

2.3 MIMO Impedance-Based Stability Criterion

This section aims to develop more detailed converter and grid models, to serve as a foundation to the Generalized Nyquist Stability Criterion (GNC) for MIMO systems. The basics of the GNC is described in Appendix 2.3, and will therefore be directly applied here. As mentioned in the introduction, literature in the last decade [21], [22], [23] discovered that the PLL has negative impact on system stability. To investigate this further, the converter modeling in this section is based largely on the model in [13] which was a further improvement of the model in [23].

2.3.1 Converter Modeling in dq-reference frame including PLL dynamics

To guide the derivation of the MIMO converter model, the exact same converter-grid system from Figure 2.2 in last section will be explored, the only difference is that more details will be included in the MIMO case. Small-signal models for this converter topology with grid connection is well documented in the literature, for example in [13], [23], [24] and [27] , therefore no derivation will be presented here, and the final result is presented in Figure 2.11. All the variables are the same as last section, except for the dq-frame duty cycle variables d_d, d_q, D_d, and D_q, which all are new. Steady-state values are denoted with uppercase letter, and small-signal variables with lowercase letters. For the small-signal variables, the usual tilde is dropped to ease notation, and if the variable is written in lowercase it is implied that it is a small-signal variable. The convention for the direction of converter current, DC-side current and converter impedance should be noted, which is out of the converter into the grid, as the converter is operated in inverter mode for the entirety of this thesis, in line with the scope. Now this has nothing to do with the underlying dynamics, as it is just a convention, but it results in that some of the transfer function matrices in this section have different signs compared to the model in [13], which is the main inspiration for the MIMO converter model in this thesis. The workflow to derive a complete MIMO model based on this figure is to first derive a complete model for the power stage, and then controller transfer functions.

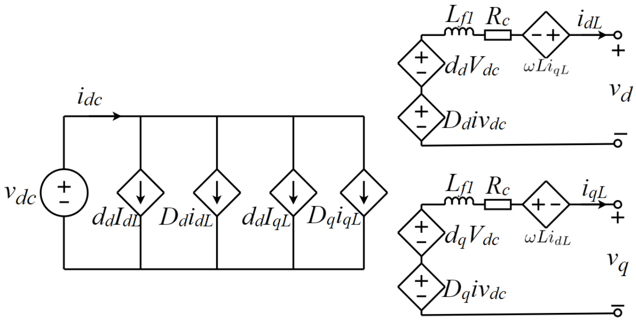

Figure 2.11: Small-signal model of converter in dq-domain.

From Figure 2.11 it is evident that for the power stage, there are two relevant transfer function matrices that need to be presented, when the dc-side voltage dynamics are neglected:

- Inductor current vector to grid voltage vector transfer function matrix, $\mathbf{Z_{out}}$.
- Duty cycle vector to inductor current vector transfer function matrix, $\mathbf{G_{id}}$.

The output impedance of the power stage is relatively straight forward, and can be found from Figure 2.11 by setting d_d, d_q, and v_{dc} to be zero.

$$\mathbf{Z_{out}} = \frac{\mathbf{v}}{\mathbf{i_L}} = -\begin{bmatrix} R_c + sL_{f1} & -\omega L_{f1} \\ \omega L_{f1} & R_c + sL_{f1} \end{bmatrix} \tag{2.14}$$

The dd and qq components of the output open-loop impedance of the converter is the same as the impedance of the first filter inductor in the LCL-filter, with one inductive and one resistive component. In the dq and qd channels, the entries represent the coupling effect of the dq-transformation. As mentioned before, more details on complexities introduced by the dq-transformation and conventional current control to handle this can be found in appendix A and B.3, respectively.

The transfer function matrix $\mathbf{G_{id}}$ can be derived in the exact same manner, only difference is that this time the grid voltage perturbations are set to zero instead of the duty cycle perturbations. The result is presented in (2.15).

$$\mathbf{G_{id}} = \frac{\mathbf{i_L}}{\mathbf{d}} = \frac{V_{dc}}{(R_c + sL_{f1})^2 + (\omega L_{f1})^2} \begin{bmatrix} R_c + sL_{f1} & \omega L_{f1} \\ -\omega L_{f1} & R_c + sL_{f1} \end{bmatrix} \tag{2.15}$$

This completes the description of the power stage of the converter, and it is illustrated by the MIMO power stage block diagram in Figure 2.12.

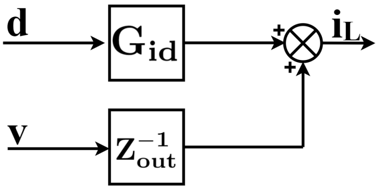

Figure 2.12: MIMO power stage small-signal block diagram.

To explain why it is necessary to introduce the PLL dynamics, consider the illustrations in Figure 2.13.

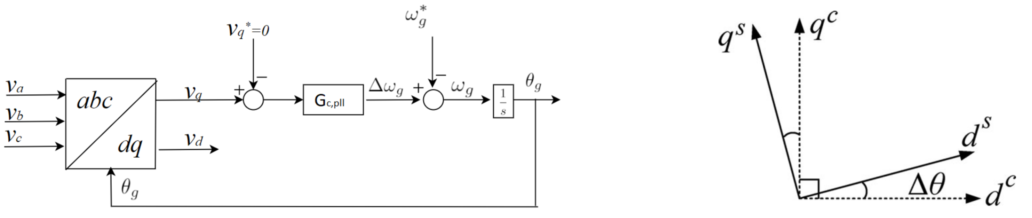

(a) SRF-PLL block diagram.

(b) System and controller dq-reference frames [13].

Figure 2.13: SRF-PLL block diagram and illustration of difference in system and controller reference frame when system is disturbed from steady-state.

In Figure 2.13a, the block diagram of a SRF-PLL from Appendix B.2 is repeated. The operation and function of the PLL is covered in the appendix, and will therefore not be repeated here, only the relevant transfer functions will be listed. The PLL controller is of type PI, so the open-loop transfer function from input v_q to output θ_g is

$$H_{pll} = G_{c,pll}\frac{1}{s} \tag{2.16}$$

when $G_{c,pll}$ is the PLL PI controller represented by

$$G_{c,pll} = K_{p,pll} + \frac{K_{i,pll}}{s} \tag{2.17}$$

This results in the large-signal closed-loop PLL transfer function , T_{pll} being equal to the expression in (2.18) [12].

$$T_{pll} = \frac{V_d^s H_{pll}}{1 + V_d^s H_{pll}} \tag{2.18}$$

However, it is the small-signal transfer function that is of interest, which is derived for example in [13] and [27], which is equal to the expression in (2.19) defined as G_{pll}.

$$G_{pll} = \frac{G_{c,pll}}{s + V_d^s G_{c,pll}} \tag{2.19}$$

The second part of the figure, Figure 2.13b, is the important part for considering the effect the PLL has for small-signal stability analysis. When the converter is in steady-state, the PLL has locked the input phase to the output phase, and the converter has accurate information about the grid angle and frequency. However, if the PLL is subject to a small disturbance, the PLL will introduce additional dynamics to the system. To understand the effect this has, there should be two dq-reference frames, and this is what is illustrated in Figure 2.13b. When the d-axis of the converter is not perfectly aligned with the system d-axis, the two reference frames is represented with superscripts c and s respectively, where the controller dq-frame is defined by the PLL and the system dq-frame is determined by the grid voltage. The result is that the PLL act a a bridge for small-signal perturbations in the system domain to the converter domain.

It is intuitive that this must have some implications for the system dynamics, so to formulate it mathematically, transfer function matrices for mapping between the two frames must be defined. The mapping between the two reference frames can be defined by the rotation matrix $\mathbf{T_{\Delta\theta}}$, where $\Delta\theta$ is the angle between the two reference frames [13].

$$\mathbf{T_{\Delta\theta}} = \begin{bmatrix} cos(\Delta\theta) & sin(\Delta\theta) \\ -sin(\Delta\theta) & cos(\Delta\theta) \end{bmatrix} \tag{2.20}$$

Then, the system and controller frame voltages, current and duty-cycles can be directly related by this matrix as

$$\mathbf{v^c} = \mathbf{T_{\Delta\theta}}\mathbf{v^s}, \mathbf{i^c} = \mathbf{T_{\Delta\theta}}\mathbf{i^s}, \mathbf{d^c} = \mathbf{T_{\Delta\theta}}\mathbf{d^s} \tag{2.21}$$

To get an intuitive explanation to why this matters to the operation of the converter, consider the following argument. When a disturbance in the grid voltage occurs, this moves the system away from steady-state and triggers $\mathbf{T}_{\boldsymbol{\Delta}\theta}$ to be different from the identity matrix. This results in an incorrect reference angle as input to the abc-dq block before the current controller, which again results in incorrect duty cycle calculations from the controller in the dq-frame. When the dq-abc transformation is performed to get back to the abc-frame, once again the incorrect angle is used, which finally results in incorrect PWM signals. This process is shown in Figure 2.14, where the two colors clearly shows the two different reference frames, and how this influences correct operation of the control system [23] where small-signal errors gets a propagation path from the grid to the converter, through the PLL.

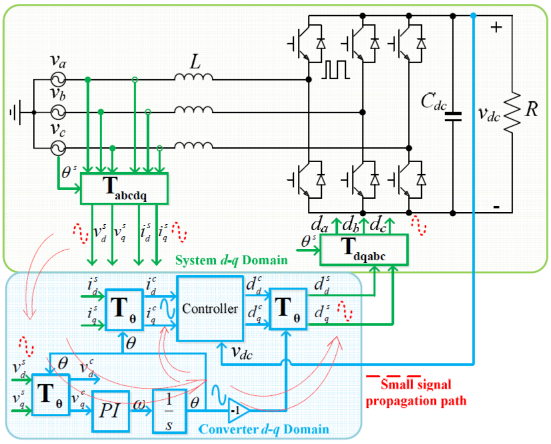

Figure 2.14: Non-ideal PLL operation that creates two dq-reference frames [23].

To translate this effect into a small-signal model represented by transfer function matrices, three new transfer function matrices are considered; $\mathbf{G^v_{PLL}}$, $\mathbf{G^d_{PLL}}$ and $\mathbf{G^i_{PLL}}$. They are defined as:

- $\mathbf{G^v_{PLL}}$ transfer function matrix from system voltage to controller voltage in dq-frame.
- $\mathbf{G^d_{PLL}}$ transfer function matrix from system voltage to controller duty cycle in dq-frame.
- $\mathbf{G^i_{PLL}}$ transfer function matrix from system voltage to controller current in dq-frame.

For compactness, the transfer functions matrices are not derived here, but complete derivations and explanations for the transfer function matrices, and how to find the steady-state duty-cycle vector for a given operating point can be found in Appendix E. The result is:

$$\mathbf{G^v_{PLL}} = \begin{bmatrix} 1 & V_q^s G_{pll} \\ 0 & 1 - V_d^s G_{pll} \end{bmatrix} \tag{2.22}$$

$$\mathbf{G^d_{PLL}} = \begin{bmatrix} 0 & -D_q^s G_{pll} \\ 0 & D_d^s G_{pll} \end{bmatrix} \tag{2.23}$$

$$\mathbf{G^i_{PLL}} = \begin{bmatrix} 0 & I_q^s G_{pll} \\ 0 & -I_d^s G_{pll} \end{bmatrix} \tag{2.24}$$

To complete the converter MIMO model, four more effects needs to be considered, measuring, sampling, filtering and delays.

Effects from measuring, sampling and filtering naturally comes from the current and voltage measurements, due to the various processes the signal conditioning gives. A simple way to model the combined effect of measuring, sampling and signal conditioning effects of the filter is a low pass filter. For now this will be approximated to a second order low-pass filter. Therefore the filter transfer function matrix, denoted $\mathbf{K}$, with cutoff frequency ω_n and damping ζ is equal to

$$\mathbf{K} = \begin{bmatrix} \frac{\omega_n^2}{s^2+2\zeta\omega_n s+\omega_n^2} & 0 \\ 0 & \frac{w_n^2}{s^2+2\zeta\omega_n s+\omega_n^2} \end{bmatrix} \tag{2.25}$$

Due to the use of digital control and PWM there will be a time delay in the system, often represented by a first order Padé approximation with time constant T_{del}. T_{del} is equal to $\frac{1.5}{f_{sw}}$, and the transfer function matrix $\mathbf{G_{del}}$ is modelled as a first order Padé approximation, which is a fairly standard way to model delays [13]. By having a first order approximation compared to second order or higher, unnecessary complexity in the final system representation is also avoided.

$$\mathbf{G_{del}} = \begin{bmatrix} \frac{1-0.5T_{del}s}{1+0.5T_{del}s} & 0 \\ 0 & \frac{1-0.5T_{del}s}{1+0.5T_{del}s} \end{bmatrix} \tag{2.26}$$

Now the effects of the five new transfer functions $\mathbf{G^v_{PLL}}$, $\mathbf{G^d_{PLL}}$, $\mathbf{G^i_{PLL}}$, $\mathbf{G_{del}}$ and $\mathbf{K}$ can be added to the power stage MIMO block diagram from Figure 2.12. This is presented in Figure 2.15a.

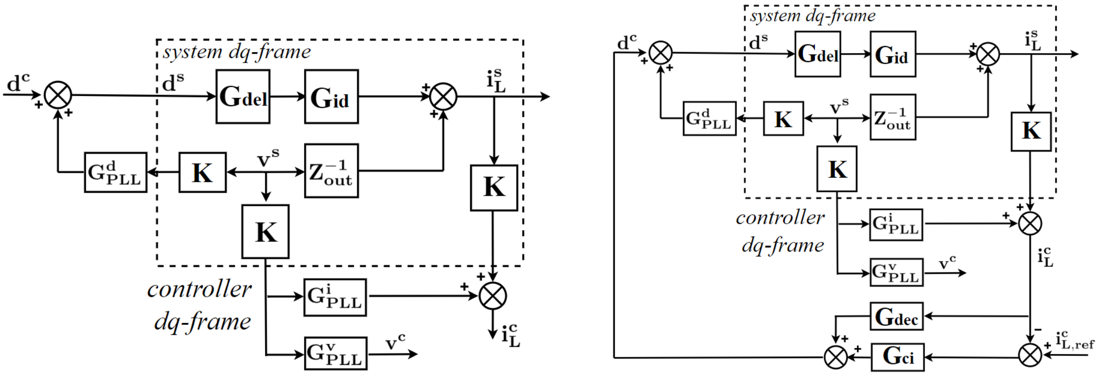

(a) Small-signal converter model with PLL dynamics.

(b) Small-signal converter model with PLL dynamics and closed-loop control.

Figure 2.15: Converter small-signal models.

Figure 2.15a still shows the basic power stage configuration from Figure 2.12, as $\mathbf{G_{id}}$ and $\mathbf{Z^{-1}_{out}}$ can be recognised at the top of the figure with he same inputs and output as before. But the major difference being the two dq-frames denoted with superscript c and s as described before and added transfer function matrices for filtering and delays. For, example to get a relation between the system voltage vector $\mathbf{v^s}$, consisting of the elements v^s_d and v^s_q, they have to go through $\mathbf{G^v_{pll}}$ to get the controller version of the grid voltage, $\mathbf{v^c}$.

Therefore, the dotted line marks the border between the system and the controller, and to go from one to the other $\mathbf{G^v_{pll}}$, $\mathbf{G^i_{pll}}$ or $\mathbf{G^d_{pll}}$ must be used.

However, from Figure 2.15a alone it is not evident where the controller duty cycle vector $\mathbf{d^c}$ comes from, and therefore the loop has to be closed. As the converter is operated in current-controlled mode, the inductor current with system reference, $\mathbf{i_L}^\mathbf{s}$, is measured, gets filtered and affected by $\mathbf{G^i_{PLL}}$ to get the controller reference inductor current, $\mathbf{i_L}^\mathbf{c}$. The loop is closed by comparing the inductor current vector with the reference, feed it thought the current controller transfer function matrix, $\mathbf{G_{ci}}$, and add the decoupling transfer function matrix $\mathbf{G_{dec}}$. $\mathbf{G_{ci}}$ and $\mathbf{G_{dec}}$ is defined by (2.27) and (2.28) and is in line with standard theory presented in Appendix B.3.

$$\mathbf{G_{ci}} = \begin{bmatrix} K_p + \frac{K_i}{s} & 0 \\ 0 & K_p + \frac{K_i}{s} \end{bmatrix} \tag{2.27}$$

$$\mathbf{G_{dec}} = \begin{bmatrix} 0 & \frac{-\omega L_c}{V_{dc}} \\ \frac{\omega L_c}{V_{dc}} & 0 \end{bmatrix} \tag{2.28}$$

Figure 2.15b shows the final MIMO converter model that will be used in this thesis. To use the GNC, the converter can now be represented by its closed-loop converter output impedance, defined as $\mathbf{Z_{oi}}$, which furthermore defines the closed-loop converter output admittance $\mathbf{Y_{oi}}$. With this notation, the MIMO criterion will be in line with the SISO criterion from last section. All transfer function matrices used in the final expression are defined earlier in this section, and the final expression can be seen in (2.29).

$$\mathbf{Z_{oi}} = (\mathbf{Z_{out}^{-1}} + \mathbf{G_{id}}\mathbf{G_{del}}((-\mathbf{G_{ci}} + \mathbf{G_{dec}})\mathbf{G^i_{pll}} + \mathbf{G^d_{pll}})\mathbf{K})^{\mathbf{-1}} \cdot (\mathbf{I} + \mathbf{G_{id}}\mathbf{G_{del}}(\mathbf{G_{ci}} - \mathbf{G_{dec}})\mathbf{K}) \tag{2.29}$$

Furthermore, $\mathbf{Y_{oi}}$ defined as the inverse of $\mathbf{Z_{oi}}$.

$$\mathbf{Y_{oi}} = \mathbf{Z_{oi}^{-1}} \tag{2.30}$$

Obviously, it is difficult to say anything general about the expression in (2.29). Therefore, it could be useful to look at the bode plot representation of $\mathbf{Z_{oi}}$. Two examples from the literature was chosen, with very different operating points and variables. The result can be seen in Figure 2.16. In both cases the converter output impedance $\mathbf{Z_{oi}}$ is calculated as in (2.29).

Although the two figures have some small differences, the general shape of the four magnitude plots and the four phase plots are the same, and some of the shapes can be explained quite easily. In Appendix C.2 fundamental building blocks for the converter model is created, to build a fundamental understanding of the more complex Bode plots in Figure 2.16, which will help to understand better the bode plots in Figure 2.16.

The dd-channel shows current source behavior in the low and medium frequency range. What this means is naturally dependent on the selected parameters in the PI controller, but the general shape of an open-loop PI controller can be recognized in this frequency range for both plots. After a certain frequency, e.g., around 100 Hz in Figure 2.16b, the magnitude stops being shaped by the current controller, and the power stage starts to dominate. This is because at high frequencies, the filter inductors will dominate the behavior. How smooth this transition is, depends on the system and controller parameters, and in these two figures, the first one looks smoother, without that necessarily have anything to say for system performance. More plots for

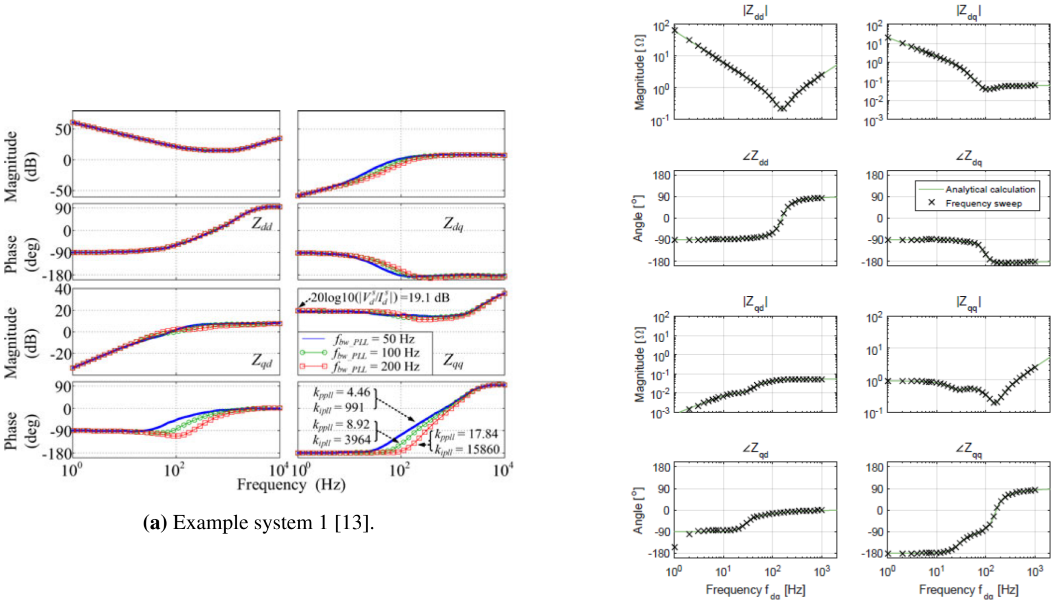

(a) Example system 1 [13].

(b) Example system 2 [10].

Figure 2.16: To examples converter systems represented by its MIMO dq-impedance bode plots.

these behaviors can be found in Appendix C.2.

For the bode plot in Figure 2.16a, in the dq and qd-channels, the amplitude is very small within the current controller's bandwidth, which makes sense, because the control system can decouple the d and q axis to a high degree, and at higher frequencies, they behave as the power stage, just at the dd-channel. But for the other plot, the amplitude of the dq-channel differs.

The most interesting result from the two plots is the qq-channel because it shows that Z_{qq} behaves as a negative incremental resistance within PLL bandwidth, which is a common source for instability in power electronic systems [13]. In [13] and [27] it is further stated that the negative resistive behavior is not just the case for the SRF-PLL but also more advanced synchronization methods such as the Decoupled Double SRF-PLL (DDSRF-PLL). In [26] it is stated that before similar MIMO converter modeling, negative incremental resistance was only found in constant power loads. Another thing to add is that the negative resistive behavior is only present when the converter is operated in inverter mode, which it is this thesis. This becomes most clear in Figure 2.16a where it is shown that for a higher PLL bandwidth, there is a wider frequency range of negative resistive behavior.

Earlier in this section, it was explained how the PLL is a bridge for small-signal perturbations from the system domain to the controller domain, but it was not clear from this description alone why this leads to negative resistive behavior. Also the term ”negative resistive behavior” may be unclear in itself, as this is not something that occurs in passive electrical circuits. And even though the concepts of two frames were introduced, this does give an intuitive explanation for why this behavior occurs.

Therefore, consider the phasor diagram of the converter when it is operated in inverter mode, and the current direction is defined to be positive into the converter, and a perturbation in the system voltage occurs. Naturally, the direction of the current makes no difference to the result, but the argument and result become more clear if the positive current direction is into the converter.

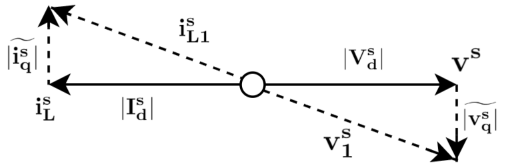

Figure 2.17: Phasor diagram of the converter with a perturbation in q-channel.

Consider the situation when the current vector of the inverter, $\mathbf{I}^{\mathrm{s}}_{\mathrm{L}}$, is synchronized with the grid voltage vector, $\mathbf{v}^{\mathrm{s}}$, so that only real power is injected to the grid. In this case, the current vector has no q-component therefore $\mathbf{I}^{\mathrm{s}}_{\mathrm{L}}= |\mathbf{I}^{\mathrm{s}}_{\mathrm{d}}|$, and the grid voltage has no q-component so $\mathbf{v}^{\mathrm{s}}= |\mathbf{V}^{\mathrm{s}}_{\mathrm{d}}|$. With the current direction defined into the converter, the situation will be as figure 2.17 shows, $\mathbf{v}^{\mathrm{s}}$ and $\mathbf{I}^{\mathrm{s}}_{\mathrm{L}}$ are parallel, but pointing in the opposite direction. Then a voltage disturbance happens in the q-channel, and the grid voltage vector changes from $\mathbf{v}^{\mathrm{s}}$ to $\mathbf{v}^{\mathrm{s}}_{1}$ which has a q-component $\widetilde{\mathbf{v}^{\mathrm{s}}_{\mathrm{q}}}$. Because of the PLL, the current vector will rotate to keep synchronization with the voltage vector, but the current controller keeps the magnitude in the d-channel unchanged, leading to the situation where the current vector $\mathbf{I}^{\mathrm{s}}_{\mathrm{L}}$ changes to $\mathbf{I}^{\mathrm{s}}_{\mathrm{L1}}$. For this to happen, clearly $\mathbf{I}^{\mathrm{s}}_{\mathrm{L1}}$ must have a q-component, $\widetilde{\mathbf{i}^{\mathrm{s}}_{\mathrm{q}}}$. And here the core of the instability problem is visible, a voltage perturbation in one direction leads to a current response in the opposite direction, which is exactly what negative resistive behavior implies. Moreover, the amplitude of the qq-channel impedance can be calculated directly from the relations in the phasor diagram, as

$$Z_{qq} = -\frac{\widetilde{\mathbf{v}^{\mathrm{s}}_{\mathrm{q}}}}{\widetilde{\mathbf{i}^{\mathrm{s}}_{\mathrm{q}}}} = -\frac{|\mathbf{V}^{\mathrm{s}}_{\mathrm{d}}|}{|\mathbf{I}^{\mathrm{s}}_{\mathrm{d}}|} \tag{2.31}$$

This relationship is only valid within the bandwidth of the PLL, and can be verified when the Bode plot of $\mathbf{Z}_{\mathrm{oi}}$ from equation 2.29 in the qq-channel at low frequencies. An interesting feature from Z_{qq} in (2.31) is that apparently, an inverter with a high current rating has a low impedance in the qq-channel.

The fact that it is possible to shape the qq-channel converter impedance by changing the PLL bandwidth is something that clearly can be exploited in an adaptive control system, but that will be discussed in Chapter 3. Another interesting result presented in [13] is that no known method removes the negative resistive behavior of Z_{qq}, where different PLLs were tested, and it was also shown decoupling control does not affect the behavior. To see how this affects the stability of the system, first, a grid model has to be created, and then the MIMO stability criterion can be formed.

2.3.2 Grid Model in dq-reference frame

Even if an eventual laboratory implementation will use grid impedance estimation for determining the grid impedance, a theoretical model is needed to compare the data to and verify that the estimation process gives accurate results. Also, there must be a theoretical model in a Hardware-in-the-Loop (HIL) implementation, that usually takes place before an actual grid connection anyways. Moreover, all simulations before laboratory implementations needs a model, therefore this has to be considered.

Naturally, everything after the PCC, seen from the converter, is considered as part of the grid, and must therefore be considered when deriving the expression for equivalent grid impedance. In the previous section, when the SISO criterion was formulated, Figure 2.3 defined how the grid was modeled after the LCL-filter, seen from the converter. This circuit is the single-phase equivalent circuit, which is not valid anymore, so it is only used for illustration of the three-phase system. The figure is repeated below for clarity, and will be used as the basis for the MIMO case as well.

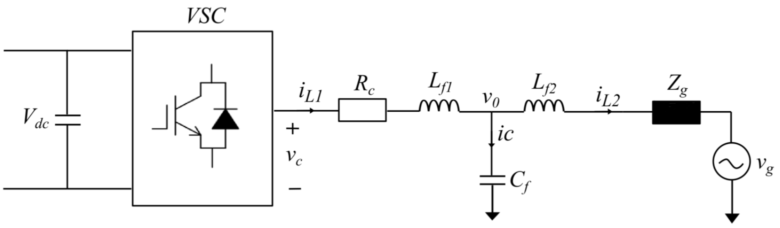

Figure 2.18: Single phase equivalent circuit of 2L-VSC connected to the grid with an LCL-filter.

In comparison to the SISO case, the grid and filter impedance elements are 2x2 matrices when modeled in the dq-domain, the dq-domain impedance for an inductor, a capacitor and resistor is listed below for clarity [10]

$$\mathbf{Z_{dq,Resistor}} = \begin{bmatrix} R & 0 \\ 0 & R \end{bmatrix} \tag{2.32}$$

$$\mathbf{Z_{dq,Inductor}} = \begin{bmatrix} sL & -\omega L \\ \omega L & sL \end{bmatrix} \tag{2.33}$$

$$\mathbf{Z_{dq,Capacitor}} = \begin{bmatrix} sC & -\omega C \\ \omega C & sC \end{bmatrix}^{-1} \tag{2.34}$$

Z_g is assumed to be mainly inductive and resistive, i.e. consist of a resistor and an inductor in series, R_g and L_g, the total dq-impedance model for the grid will have two main elements, the parallel filter element, and the serial filter and grid elements. If the former is defined as $\mathbf{Y_1}$, which in the no damping case just is the filter capacitor, and in the latter, the impedance is the sum of the second filter inductor, grid inductance, and grid resistance. The serial element is further inverted to form $\mathbf{Y_2}$, and then the total grid impedance is equal to the expression in (2.37).

$$\mathbf{Y_1} = \mathbf{Y_c} \tag{2.35}$$

$$\mathbf{Y_2} = \mathbf{Y_{Lf2}} + \mathbf{Y_{(R_g+L_g)}} \tag{2.36}$$

$$\mathbf{Z_{grid,tot}} = (\mathbf{Y_1} + \mathbf{Y_2})^{-1} \tag{2.37}$$

In this case, the grid forms a much simpler system than the large converter system from equation (2.29). It should be noted that without active or passive damping of the filter, more serious resonance problems than necessary will occur. The arguably most simple passive solution would be to add a resistor in series with the filter capacitor. For this thesis, no active damping is considered, as defined in the scope, and because filter design and analysis bring unwanted dynamics, the simplest solution is taken, where a resistor is added in series. To determine the size of this damping resistor, a common way to calculate it is presented in (2.38) [15].

$$R_d = \frac{1}{3w_{res}C_f} \tag{2.38}$$

where the resonance frequency of the filter (when the grid inductance is not taken into account) is

$$f_{res} = \frac{1}{2\pi}\sqrt{\frac{L_{f1} + L_{f2}}{L_{f1}L_{f2}C_f}} \tag{2.39}$$

It should be noted there exists more sophisticated ways to tackle resonance problems than adding a passive resistor to the filter, as this increases losses, but it is simple, effective, and in line with the scope of this thesis. Also, for the simulation cases later in this thesis, the actual numerical value of R_d is selected to be a bit lower than suggested by (2.38) for conservative measure compared to the real world.

In line with the scope of the thesis, different grid impedance estimation methods was investigated, and all the results can be found in Appendix J. Since it is not considered a main objective of the thesis, it is not included in the main part.

2.3.3 Final Stability Criterion for the MIMO Converter-Grid System

In the last two subsections, MIMO models for both the converter and the grid were derived, and finally, the GNC can be applied. As it was shown in section 2.2, the converter and grid can be represented by a small-signal Norton equivalent, which also holds for the MIMO case, where all circuit elements are vectors or transfer function matrices. Moreover, the same argumentation regarding stability from section 2.2 follows, so this will not be repeated. Therefore, also in the MIMO case, the stability only depends on the minor-loop gain. However, there are two important differences between the SISO and MIMO case.

The first difference is that, in general, matrix multiplication is not commutative. For the system under study here, that means that there are two possibilities on how the minor-loop gain $\mathbf{L}$ is defined. Consider the two possibilities in (2.40) and (2.41). The argument s is dropped to simplify notation for the rest of this chapter.

$$\mathbf{L_1} = \mathbf{Z_g Y_{oi}} \tag{2.40}$$

$$\mathbf{L_2} = \mathbf{Y_{oi} Z_g} \tag{2.41}$$

There are examples of both in the literature, where $\mathbf{L_1}$ appears in most of the cases, for example in [8], [13] and [27] and $\mathbf{L_2}$ was used in [11]. Using the same equations and substitutions from the SISO case it can be shown that $\mathbf{L_2}$ is the expression that will yield the correct result, given the underlying assumptions. However, in [25] it was documented to great detail that both the expressions will yield the same stability conclusion and that using the GNC on $\mathbf{L_1}$ could simplify the analysis compared to $\mathbf{L_2}$. Therefore, from now on, $\mathbf{L_1}$ is the expression that will be used for all purposes where the minor loop gain is needed.

The second difference is that the SISO Nyquist stability criterion cannot be used directly, and the Generalized Nyquist Stability Criterion (GNC) has to be used. This is covered in Appendix D.2, and therefore will not be covered in detail here, but summarized, it is the *eigenvalue loci* of $\mathbf{L_1}$ that cannot have any net encirclement's around (-1,0) in the complex plane if $\mathbf{L_1}$ itself has no poles in the RHP. For a 2x2 matrix, as $\mathbf{L_1}$ is, the GNC implies that there will be two eigenvalue loci, as $\mathbf{L_1}$ has two eigenvalues at each frequency it is evaluated at. This complicates the stability conclusion a bit, but still, it is a rather straight forward conclusion compared to many other methods.

Even though GNC applied on $\mathbf{L_1}$ is a simple and intuitive approach to determine stability for a given operating point, it could be challenging to use this criterion in an adaptive control approach. In [11] this was tried, where the eigenvalue loci proximity to the point (-1,0) in the complex plane was used as a parameter for the adaptive control. Even though this seems like a possible approach for ensuring stability for different grid conditions, the implementation did not work as expected, due to many different problems. Also, even though the loci of $\mathbf{L_1}$ is controlled, the pole plot of $\mathbf{L_1}$ still has to be considered for the stability analysis to be conclusive. However, if the complete closed-loop behavior is considered directly, repeated in Figure 2.19, then maybe the whole eigenvalue loci analysis can be avoided.

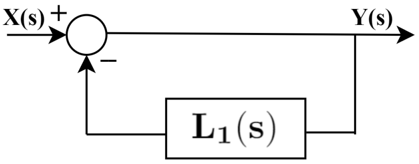

Figure 2.19: MIMO closed-loop.

The closed-loop transfer function is as follows:

$$\mathbf{L_{cl}} = (\mathbf{I} + \mathbf{L_1})^{-1} \tag{2.42}$$

where $\mathbf{I}$ is the 2x2 identity matrix. The GNC no longer is of any concern, and the poles and zeros of the closed-loop system can be found directly. As in SISO system, the closed-loop system will be stable if, and only if, there are no RHP poles for $\mathbf{L_{cl}}$. To illustrate that the use of the GNC and the pole placement of $\mathbf{L_{cl}}$ yields the same stability conclusion, an example from the literature [13] was implemented in Matlab. The eigenvalue loci for a system with two different sets of control parameters can be seen in Figure 2.20.

In both cases, $\mathbf{L}$ have no RHP poles, therefore the GNC dictates that the eigenvalue loci should have no net rotation around the point (-1,0). This is clearly not the case in Figure 2.20a where the Loci of λ_2 has net rotation around (-1,0). In Figure 2.20b, there is no net rotation, and therefore the system is stable. The same conclusion can be found the pole-zero plot of $\mathbf{L_{cl}}$ in Figure 2.20.

This leaves flexibility depending on the application. While the GNC is an intuitive graphical method, the pole placement of $\mathbf{L_{cl}}$ may be easier to use when an adaptive control scheme is to be implemented, as will be evident in Chapter 3. However, it should be noted that the definition of poles and zeros is not the same in the SISO and MIMO case, which complicates the discussion. Everything related to MIMO poles and zeros can be found in Appendix D.3.

Some other practical considerations should be taken into account before deciding between the use of the

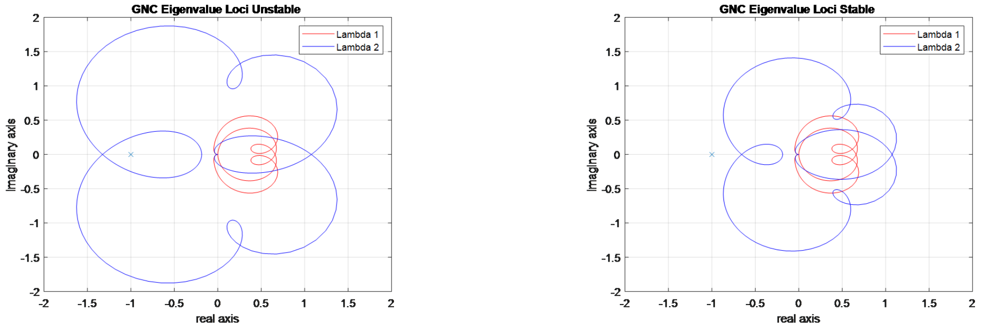

(a) GNC loci, unstable case.

(b) GNC loci, stable case.

Figure 2.20: Unstable and stable GNC loci for a system with different PLL control variables.

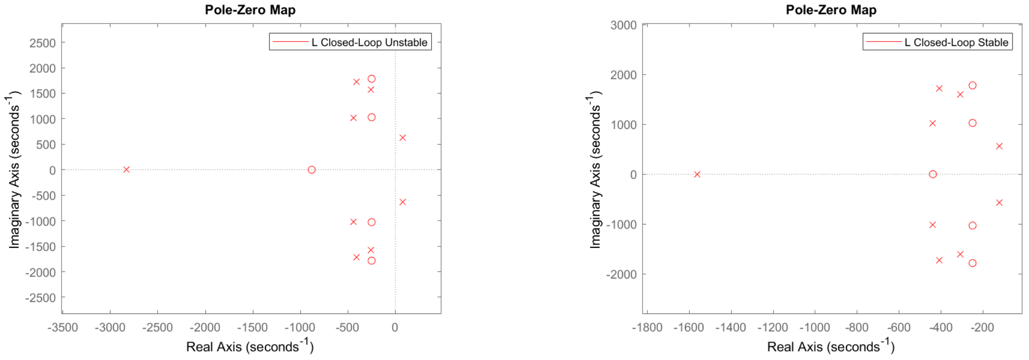

(a) Pole-zero plot, unstable case.

(b) Pole-zero plot, stable case.

Figure 2.21: Unstable and stable closed-loop pole-zero placement for a system with different control variables.

GNC or the pole placement method. One thing that affects both methods is the fact that the grid impedance is *estimated*, i.e., there is no predefined model or transfer function of the grid. This is not the case for the converter, where an impedance model can be calculated for all operating points and control parameters. The result of this has a very different effect on the two methods. Using the GNC this may be of little concern as the eigenvalue loci are calculated at every frequency anyway, and no model fitting to a transfer function matrix is necessary, but of course, it would work with model fitting as well. This gives flexibility, which is a clear advantage. For the pole placement method of $\mathbf{L_{cl}}$, there is need for a transfer function representation of $\mathbf{Z_g}$ i.e. after the grid impedance estimate is obtained this needs to be fitted to a model, and first then $\mathbf{L}$ and $\mathbf{L_{cl}}$ can be formed. As defined in the scope, the grid-impedance estimation process is not the main objective of this thesis, and previous work has been done on both grid impedance estimates and model fitting. So even though this, in general, is a great concern, it is not considered out of the scope in this thesis.

Another possible issue by analyzing the pole-placement of $\mathbf{L_{cl}}$ is that this abstraction leads to losing sight of the problem at hand. By blindly following the procedure of trusting that the modeling is correct, and determining control after this, one might miss the overall picture that is obtained with more graphical approaches of analyzing bode plots or eigenvalue loci. This again might lead to difficulties translating the results of the analysis into practical implementations.

Also, in general, numerical problems can be less of a problem in the graphical approaches, for example in the case where Matlab incorrectly calculates the placement of a pole and a zero, that in reality should be canceled. This is picked up when the bode plot is drawn and is generally not a problem, but by looking only at a pole-zero plot, one might believe that the system is unstable, but actually, there is only a numerical error.

Several other concerns need to be considered before implementation of the converter-grid system can be considered, also with simulations. Therefore, the next section will clarify these concerns and define the system representation and simplification the model will have in this thesis.

2.4 Considerations on System Representations

Assume that the complete converter model for $\mathbf{Z_{oi}}$ from (2.29) is used, and the corresponding converter admittance $\mathbf{Y_{oi}}$ is used in its complete form with no reductions. Also, a complete grid model is used to first form $\mathbf{L_1}$, and thereafter form $\mathbf{L_{cl}}$. This would be a MIMO system of a very high order, that could be very difficult to analyze, or even worse, try to develop an adaptive control system for. Not to mention the numerical problems that can arise when trying to work with such a system. Therefore, it should at least be considered to have some form of model reduction. This is done in it completeness in Appendix D.4 where first the motivation for model reduction is presented, and thereafter an investigation to whether it is valid to do it on the proposed model reduction without losing important system dynamics. This is not included in the main body of this thesis, because formal model reduction is outside the scope of this thesis and a rather pragmatic approach is taken in the appendix. However, it was concluded that for the scope of this thesis simplified versions of various transfer function matrices are going to be used, and some of the most important results are repeated here.

First of all, the filter transfer function matrix $\mathbf{K}$ was completely neglected, and set to the 2x2 identity matrix, when it was discovered that for the relevant frequency range it had little to no effect on system dynamics. Secondly, it was discovered that the decoupled version of the converter admittance matrix was a good approximation of the complete system. More precise, this means that the dq and qd elements of $\mathbf{Z_{oi}}$ were set to zero before it was inverted to form $\mathbf{Y_{oi}}$. Third, different versions of $\mathbf{L}$ were studied with and without the dq and qd decoupling for both the converter and the grid, and the result was that both grid decoupling and converter decoupling was a good approximation for the scope of this thesis. Therefore, the version of $\mathbf{L}$ that is to be used for the rest of this thesis are repeated below.

$$\mathbf{L(s)} = \mathbf{Z_{g,dec}Y_{oi,dec}} = \begin{bmatrix} Z_{g,dd} & 0 \\ 0 & Z_{g,qq} \end{bmatrix} \cdot \begin{bmatrix} Y_{oi,dd} & 0 \\ 0 & Y_{oi,qq} \end{bmatrix} = \begin{bmatrix} Y_{oi,dd}Z_{g,dd} & 0 \\ 0 & Y_{oi,qq}Z_{g,qq} \end{bmatrix} \tag{2.43}$$

As pointed out in the Appendix, there are many advantages of working with a diagonal transfer function matrix, and when $\mathbf{L}$ is diagonal, $\mathbf{L_{cl}}$ is also diagonal. This, and other properties that is a result of the diagonal version of the minor-loop gain becomes even more clear in Chapter 3 where the system dynamics is explored and adaptive control methods implemented.

Chapter summary

The list below shortly summarizes the main takeaways from this chapter:

- The selected SISO modeling of the converter-grid system is useful for forming the initial stability criterion, but it is inadequate for capturing the fundamental stability issues at high grid impedance levels, since the PLL dynamics are not captured.
- The fundamental problem of the PLL is captured by the selected MIMO converter model, and it shows that the converter has negative incremental resistance behavior within PLL bandwidth.
- Grid modeling in dq-domain is fairly straight-forward, and in the MIMO case the GNC can be used to determine stability. Furthermore, the user can either use the GNC on the open-loop minor-loop gain transfer function matrix $\mathbf{L}$, or use the closed-loop minor-loop gain $\mathbf{L_{cl}}$ pole placement to determine stability.
- It was discovered that a decoupled system representation was preferred for adaptive control, as it dramatically reduced the system order, without losing essential system dynamics.

Chapter 3

Impedance-Based Adaptive Control

This chapter presents the main new theoretical contributions of this thesis, which are two novel adaptive control methods for the grid-connected VSC. The first section covers the methodology that are common for both methods, before Section 3.2 derives an adaptive PLL method, and Section 3.3 derives the multivariable adaptive method where both the current controller and PLL is adapted based on the grid impedance.

3.1 Adaptive Control Methodology

First of all, it has to be clear what the control objective is, which in this thesis is formulated below:

"Stable operation of the converter for as high grid impedance value as possible, while at the same time ensuring good control performance under different grid conditions."

The last part of that statement is included because there exists the possibility of having real-time grid impedance estimates by using the method described in [11]. On the other hand, if this was not available, and simple static control had to be implemented, another possible control objective could be to have stable operation for as large as possible grid impedance, or sacrifice stability at high impedance levels to ensure good dynamic performance under normal grid conditions.

Secondly, a clear work methodology has to be established before system dynamics for different grid conditions are explored, where certain limitations has to be defined to limit the complexity. Starting with the grid modeling, the discussion in Appendix B.4 limits the grid impedance dynamics to change in equivalent grid inductance. The motivation and justification for this is done in the appendix, and it is also in line with the scope of this thesis, and the reasoning will therefore not be repeated here.

Only $\mathbf{L_{cl}(s)}$ and its pole placement will be considered for the adaptive control system. Another possible approach is looking at $\mathbf{L(s)}$ poles and the eigenvalue loci and in some way use the GNC. One possible way of using the GNC method would be to implement an adaptive control system that makes sure that the net encirclements of the two eigenvalue loci of $\mathbf{L_(s)}$ are in line with the GNC, which would be a very elegant solution. However, this was tried in [11] where some serious issues occurred, so this method was discarded. A method that could be easier to implement would be looking directly at the pole placements of $\mathbf{L_{cl}(s)}$ and derive some control law directly from its behavior, when the five varying variables $K_{p,pll}$, $K_{i,pll}$, K_p, K_i and

L_g are iterated over a large set of values. Moreover, the selected method for doing this is gain scheduling. This will be explained in more detail in the specific methods, but in general, the concept is based on predefined values for the control parameters based on simulation results. Another limitation defined in this thesis is that instead of trying to iterate over the five variables listed above, only three are chosen, as both the CC and PLL controllers are represented with a bandwidth variable. Naturally, there are many ways to combine a proportional and integral gain to form a specific bandwidth, so some interesting dynamics might be missed here, but this is regarded as out of the scope of this thesis. More on how the controller is represented by one variable can be found in Appendix F.

Once this is established, the next thing to consider is what type of control law should be implemented. In Appendix H, some of the background material for adaptive control is discussed, and some methods and categories are mentioned. The first thing that has to be taken into account before selecting an appropriate method is the nature of the system under study. In general, there are three different approaches for analyzing $\mathbf{L_{cl}(s)}$:

- **Symbolic computation**. When $\mathbf{L_{cl}(s)}$ is written on its symbolic form, the expression is too big to try to analyze in any possible way. Therefore, it should unfortunately be excluded to try to make an analytical relation between the grid impedance and the four control parameters and then relate that to the pole placement of $\mathbf{L_{cl}(s)}$.
- **Pseudo-symbolic computation**. Another possibility would be to implement a pseudo-symbolic representation where all variables except one, or the five variables of interest, is substituted by its numerical value. However, this does not change the problem either, because the roots of the system will still be on a form that is impossible to work with.
- **Pure numerical computation**. That means that $\mathbf{L_{cl}(s)}$ has to be studied numerically. Naturally, it is still possible to gain an understanding of the system by simulation over a large range of parameter values, but this does not result in a general analytical relation between the control parameters and the grid impedance. To understand if this has any implications for further work, once again it is referred to as the control objective stated earlier in this section. It does not matter how the control is implemented as long as the control objective is met. This is not true in the general case, as theoretical information about any system is vital, but for the scope of this thesis, a numerical method is the only one considered. The numerical solution may not be as elegant as an analytical control law would be, but this does not matter in the end if the same result is achieved.

Now that some limitations are set for $\mathbf{L_{cl}(s)}$, the possibilities have to be explored. As mentioned in Appendix H, there is a family of adaptive control methods called Adaptive Pole Placement Control (APPC), and a variant of this will further be considered. More specifically, the first adaptive control method in this thesis is concerned with the placement of the critical pole. From now on, the Real Value of the Critical Pole is defined as RVCP, which will be referred to a lot in the rest of this thesis. To illustrate the concept, consider Figure 3.1

Figure 3.1 shows the pole and zero placement for a stable case of $\mathbf{L_{cl}(s)}$ for an example converter-grid system described in Chapter 2. Figure 3.1a shows all the poles and zeros of $\mathbf{L_{cl}(s)}$, while Figure 3.1b only shows the poles and zeros closest to the RHP, including the critical pole that in this case is on the real axis. A very nice property of $\mathbf{L_{cl}(s)}$ is that it is diagonal with the system representation discussed in Section 2.4, which results in that the poles and zeros of $\mathbf{L_{cl}(s)}$ is the same as the poles and zeros of the individual transfer functions in $\mathbf{L_{cl}(s)}$. This means that it is relatively easy to track the pole trajectory of the critical pole, and even determine if this pole is a pole of the dd or qq channel of $\mathbf{L_{cl}(s)}$. As discussed earlier, the dd-channel is mostly related to the current control, while the qq-channel is mostly related to PLL control. With this in mind, the system dynamics can be investigated by simulating the system for a range of grid impedance and control parameter

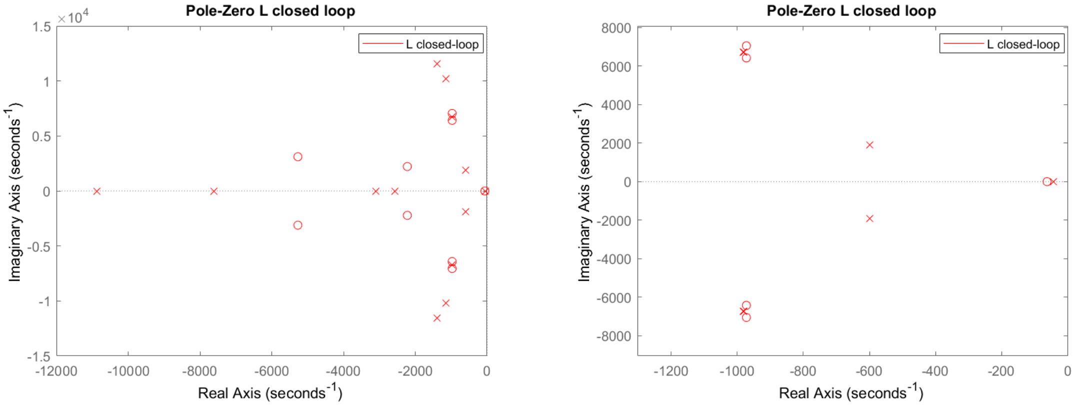

(a) Poles and zeros for an example system of $\mathbf{L}_{\mathbf{cl}}(\mathbf{s})$.

(b) Critical pole of $\mathbf{L}_{\mathbf{cl}}(\mathbf{s})$.

Figure 3.1: Complete Pole-Zero plot for $\mathbf{L}_{\mathbf{cl}}(\mathbf{s})$ and zoomed in to highlight critical poles of $\mathbf{L}_{\mathbf{cl}}(\mathbf{s})$.

values, and from this meaningful adaptive rules can be defined. This is what the next sections of this chapter will explore in detail.

Before a specific system can be explored more in detail, two different cases are defined. Results from the literature, and also own previous work in [16] indicate it is the PLL and not the current controller, that is the limiting factor regarding stability. As an introduction to this topic consider the two Pole-Zero plots in Figure 3.2.

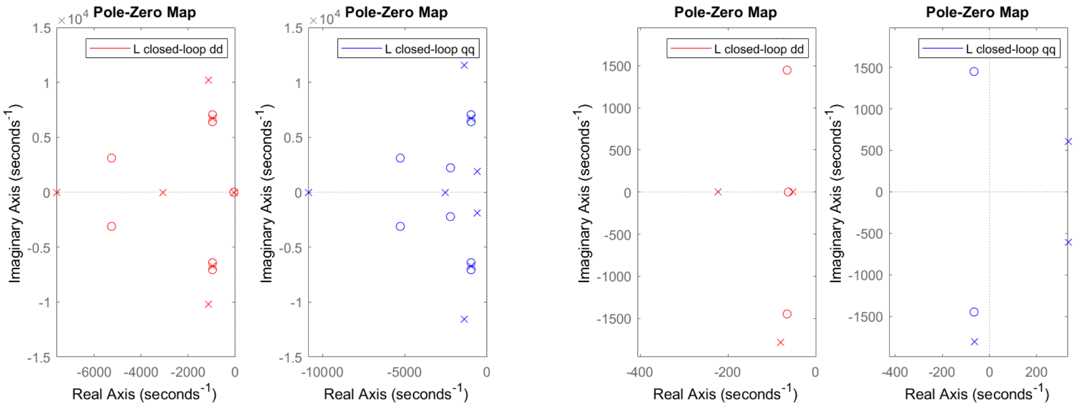

(a) Pole-Zero plot of $\mathbf{L}_{\mathbf{cl}}(\mathbf{s})$ split in *dd* and *qq* stable case.

(b) Pole-Zero plot of $\mathbf{L}_{\mathbf{cl}}(\mathbf{s})$ split in *dd* and *qq* unstable case.

Figure 3.2: Comparing stable and unstable case of $\mathbf{L}_{\mathbf{cl}}(\mathbf{s})$ when poles and zeros are split in *dd* and *qq* channel.

In the first plot, the same example system as earlier is considered, only this time the poles and zeros are split up in the *dd* and *qq*-channels. In the second plot, a much higher grid impedance is selected, and it shows that $\mathbf{L}_{\mathbf{cl,qq}}(\mathbf{s})$ is the entry of $\mathbf{L}_{\mathbf{cl}}(\mathbf{s})$ that have poles in the RHP, while $\mathbf{L}_{\mathbf{cl,dd}}(\mathbf{s})$ appears to be stable. Naturally, this results in the complete MIMO system to be unstable. This serves as a motivation to have an adaptive control system where the PLL controller is regulated depending on the grid impedance. This will be the first attempt to implement an adaptive control system and will be explored further in Section 3.2.

However, it would be obtuse to assume that there is no interaction between the PLL controller and the current controller. The controllers are part of the same closed-loop, and naturally, there will be some interaction. Subsection 2.3.1 indirectly described this interaction, as it is shown that a disturbance in the grid will propagate the error to the current controller via the PLL, as the PLL serves as the reference for the current controller. But compared to typical cascaded control, with for example inner current control and outer voltage control or power control, the interactions between the current controller and the PLL controller is more difficult to explain. Mathematically, it was described in Subsection 2.3.1, but this is not a very intuitive way to look at the problem. Also, this model does not give any clear guidelines on how to design and select the current controller and PLL controller parameters in relation to each other. Also, the literature is not very detailed on the interactions between current control and PLL, except for the relations already described in Subsection 2.3.1.

All of this taken into account, it should be considered to have an experimental approach to the multivariable adaptive control, as the underlying dynamics are very hard to describe and understand analytically, and also, develop adaptive control rules from. This was also pointed out in [65], where the conclusion was that a general multivariable parameter selection depending on grid conditions would be very complicated. Therefore, to avoid a complicated mathematical mess, that most likely would result in nothing useful, Section 3.3 will serve as an experimental approach to derive meaningful multivariable adaptive control based on the grid impedance.

3.2 Adaptive PLL Control

This section derives the complete adaptive PLL method used in this thesis. It is split into two subsections, the first one exploring and explaining system dynamics as a motivation for the specific method in the second subsection. Therefore, if the reader is only interested in the specific method, it is possible to jump directly to Subsection 3.2.2.

3.2.1 Conceptual Design of Adaptive PLL

This section aims to derive adaptive control rules between grid impedance estimates and PLL control parameters in the form of a gain schedule for the PLL. The first thing that must be established is a base-case system and verification that this base-case is stable. In this thesis, this is done for a specific system in Appendix F, where the methodology for finding appropriate starting parameters is presented, derived, and later verified with simulations by building the MIMO converter and grid models in Matlab. All other relevant parameters for the system under study is listed in Table G.2 in Appendix G.

After the base-case is established, further system dynamics can be explored, where the grid impedance range of interest has to be specified, and this range is split up in suitable simulation intervals. What this range of grid impedance is will depend on the specific system, but some general traits apply for all systems. To guide the discussion, consider Figure 3.3.

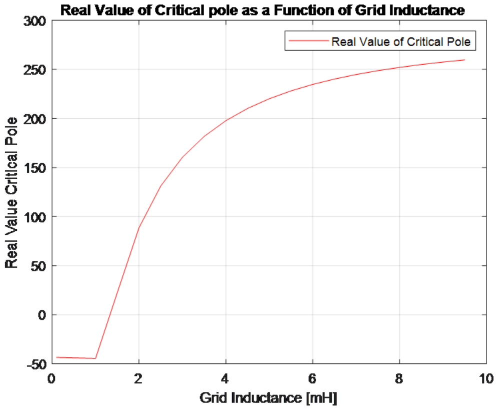

Figure 3.3: Real Value of Critical Pole (RVCP) over a range of grid inductance values.

The plot shows the RVCP as a function of grid inductance value. What this means in practical terms is that after the system base-case is defined, the system is simulated over a range of grid inductance values, for each case the pole with the largest real value is stored in a vector, and finally the critical pole vector is plotted against the grid inductance. The purpose of doing this is to understand some of the underlying system dynamics. The result is clear, and also as expected, the higher the grid inductance value, the higher the numerical value the RVCP has. This arbitrary example goes unstable at a value around 1 mH, as this is where the critical pole enters the RHP. Naturally, the stability limit depends on how the base-case is defined, and the numerical value for this particular example is not of interest for now. What is of interest is the underlying implications of this figure, what this means for the control objective, and the new questions the plot implies. First of all, the plot says nothing about the root of the instability other than that higher grid inductance moves the system closer to the stability limit. Therefore, it is of interest to dive deeper an explore it the critical pole comes from the dd or qq channel. The second aspect is that the axis format in Figure 3.3 is an inadequate way of explaining system behavior at low grid inductance values. Therefore consider Figure 3.4.

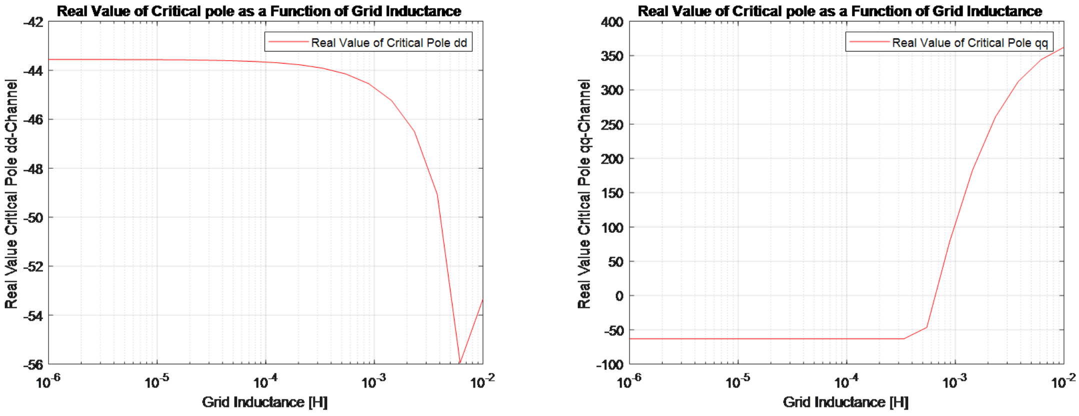

(a) RVCP dd-channel of $\mathbf{L_{cl}(s)}$.

(b) RVCP qq-channel of $\mathbf{L_{cl}(s)}$.

Figure 3.4: Comparing RVCP in dd and qq channels.

This time, another example system is simulated over a range of grid inductance values that are logarithmically spaced and plotted over a logarithmic x-axis. In Figure 3.4a, the RVCP in dd-channel is plotted, and in 3.4b the RVCP in qq-channel is plotted. Also, here the result is as expected, over the full grid inductance range the critical pole in dd-channel is in the LHP, and therefore is not a source to instability in $\mathbf{L_{cl}(s)}$. The same can not be said about the qq-channel, where the same trend as earlier is observed after a certain grid inductance is reached, so the qq-channel is the source of instability. From this discussion, the appropriate inductance range can be determined for the system, because the critical pole in either of the channels does not appear to change very much before a certain level is reached, and therefore are not of interest for adaptive control since the base-case control parameters handle it. Similar results from the literature, for example, [13] and [65], also suggests that the system instability is primarily caused by the qq-channel, if the current controller is tuned properly.

The next step is to implement countermeasures to the increasing RVCP. As it is now demonstrated that the qq-channel is the source of instability, at least for the example system here, only the qq-channel of $\mathbf{L_{cl}(s)}$ is considered for now. It should be mentioned that this will not be the case of all systems, depending on how the base-case is defined, but Section 3.3 handles multivariable adaptive control, so that will be covered there. That means that the only tool available is the modification of the PLL control parameters $K_{p,pll}$ and $K_{i,pll}$. As mentioned before, the relation between PLL bandwidth and system stability is not straightforward. On one hand, higher PLL bandwidth leads to the faster dynamic response, but it also extends the frequency range where the qq-channel converter impedance behaves as a negative incremental resistor. Therefore, the intuition should be that increased PLL bandwidth should lead to a higher numerical value for the critical pole when the grid inductance is in a very high range. This is confirmed by Figure 3.5 where this time the grid inductance is kept constant at a very high value, and the PLL bandwidth is iterated for an example in the range from 50 Hz to 500 Hz.

The RVCP has a lower value the lower the PLL bandwidth is, but in this example, it does not seem to matter

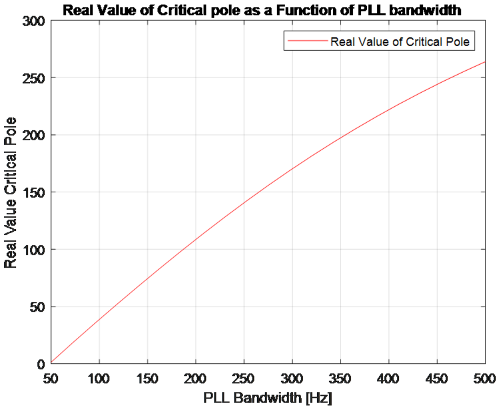

Figure 3.5: RVCP of $\mathbf{L_{cl}}(s)$ over a range of PLL bandwidths.

anyway, since over the full range, the RVCP has a positive value. Also, this time the confirmation asks new questions that are vital to the adaptive control method that should be implemented. Some of them are:

- What is the lower limit to the PLL bandwidth that still ensures the correct operation of the converter?
- Is this lower limit captured in the system dynamics of the MIMO converter model?
- How should this information be used in regards to the grid inductance level?
- How should PLL bandwidth and grid inductance be combined to form an effective control law?

First of all, the limits of the model have to be defined. In Appendix F, the pros and cons of high and low PLL bandwidths are discussed, and also that the PLL bandwidth lower limit should be equal or higher than the grid fundamental frequency. To investigate if this is captured in the RVCP movement of $\mathbf{L_{cl}}(s)$, consider Figure 3.6.

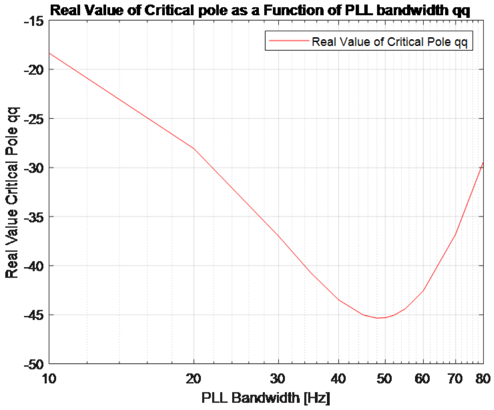

Figure 3.6: RVCP of $\mathbf{L_{cl}}(s)$ over low bandwidth PLLs.

Figure 3.6 shows the same thing as Figure 3.5, the value of RVCP as a function of PLL bandwidth for a specific grid inductance value. The difference this time is that only the qq-channel poles are considered, and the PLL bandwidth is much lower than before, and a relatively high grid inductance value is selected. The plot shows exactly the trend that is expected, starting from 80 Hz bandwidth, the RVCP gets more negative, indicating that the system moves further away from the stability limit. This is expected because the negative resistive behavior frequency range is reduced. But at around 50 Hz of PLL bandwidth, the trend changes, and the RVCP increases again, which indicates that the system is moving towards the stability limit again. The intuitive explanation for this would be that the converter is not able to operate correctly if the PLL bandwidth is lower than the grid fundamental frequency. This could indicate that there exists a global minimum for RVCP and that this minimum is expected to be close to 50 Hz of PLL bandwidth. Therefore, only considering his plot one might think that a lower PLL bandwidth does not need to be defined in the model because it is captured in the model anyway.

However, this is not the case, and the reason becomes clear by considering a similar plot in Figure 3.7a. Again, the RVCP is plotted against PLL bandwidth, only this time it is also done for a range of grid inductance values. If the model were to capture the fact the converter is not able to operate correctly at a PLL bandwidth much lower the grid fundamental frequency, one would expect that the global minimum for RVCP would be approximately the same for all grid inductance values.

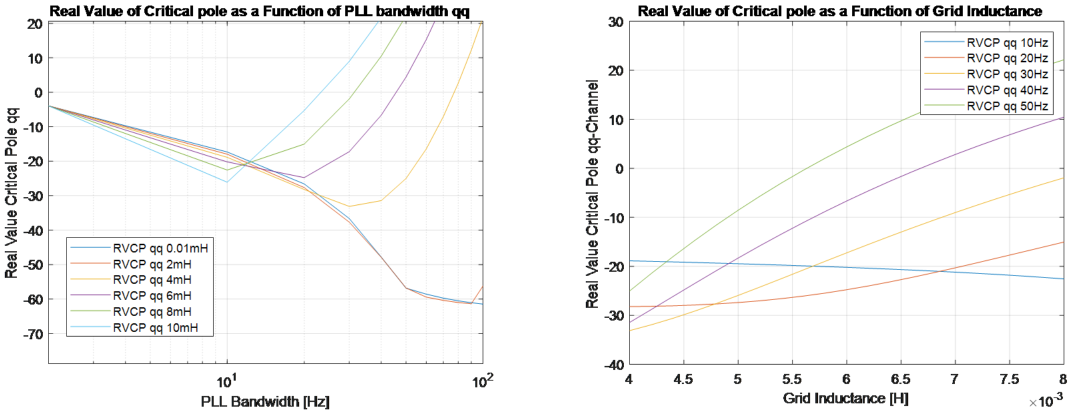

(a) RVCP for low-frequency PLLs for different grid inductance values.

(b) RVCP for low-frequency PLLs for different grid inductance values.

Figure 3.7: Two ways of visualizing RVCP for different PLL bandwidths and different grid inductance values.

As Figure 3.7a shows, it is not the case that the global minimum for the RVCP is at the same PLL bandwidth for all grid inductance levels. To start with the case for lowest grid inductance value, the minimum is not included in the plot, because a very low grid inductance value indicates that the converter can operate at a high PLL bandwidth without any resonance problems. For the rest of the PLL bandwidths, it is clear from the figure that there exists a global minimum, and that this minimum is located at lower PLL bandwidth for higher grid inductance value. This means that the model does not capture all necessary dynamics. This means that by blindly following the RVCP methodology for determining optimal PLL bandwidth can result in unrealistic results. However, it can quite easily be solved by manually defining a lower PLL bandwidth that the system is allowed to operate at, and a natural choice would be 50 Hz, or whatever the grid fundamental frequency is in the relevant area. This is also shortly presented in Appendix F. The fact that the model does not capture the relevant dynamics under 50 Hz is a clear weakness of the model, but this and possible reasons for it are discussed in Chapter 5, for now, it is noted and accepted.

Another equally useful way to visualize the inability the model has to capture all dynamics is shown in Figure 3.7b, where this time the variable is grid inductance and the cases are PLL bandwidth. More specifically, it shows that following the model directly the converter operates best at very high grid inductance levels at PLL bandwidths much lower than the fundamental grid frequency, which is unrealistic. Therefore, 50 Hz is selected as the minimum allowed PLL bandwidth. In practical terms, this means that when the gain schedule is developed, and the simulation indicates that the PLL bandwidth should be reduced to a value lower than 50 Hz to compensate for the higher grid inductance, this should not be done. It could also be useful to specify upper PLL bandwidth limits, for example, defined as ten times the fundamental frequency. More on PLL bandwidth consideration are discussed in Appendix F.

Now that lower and upper model validity limits are out of the way, a natural thing to consider next is the nature of the gain schedule, and how it should be created. This goes into the core of the model and there are several possible approaches. To exemplify the discussion, let say the RVCP moves from -50 to -40 for grid inductance values of 1mH to 2mH, respectively, for an arbitrary system. One intuitive way to tackle this is to reduce the bandwidth with the minimum amount that at least moves the RVCP from -40 back to -50. By doing this, it is ensured that within the interval 1 mH to 2 mH the RVCP does not get closer to the stability limit.

In regards to this, it is also natural to consider when the first adaptive measures should be taken, where the base-case control parameters first are updated, and how large the grid inductance is here. This is naturally dependent on system specifics, but there are some general rules regardless of the system. This is already considered in an earlier figure in this section, in Figure 3.4b, which shows that for a lower grid inductance value than approximately 0.35 mH the RVCP does not move at all. Without going into too much detail, the reason for this is that there is a pole on the real axis that does not move much by changed PLL bandwidth or grid inductance, and therefore in this case at lower grid inductance levels than 0.35 mH in this example, this pole is the critical pole. But for larger grid inductance values than 0.35 mH, there is a complex conjugated pole pair that becomes the critical pole, and its real value is the RVCP. This is very convenient as for the case when the complex conjugated pole pair takes over at the critical pole can serve as the point where the gain schedule starts. In other words, at lower grid inductance levels than 0.35mH in this example, no changes should be done to the base-case control parameters.

When it comes to how big the grid inductance intervals for the gain schedule should be, it comes down to the preferences and demands of the application. But also here, some general rules apply when considering the nature of the RVCP in Figure 3.3 earlier in this section where it is shown that the RVCP as a function of grid inductance value resembles a logarithmic function. This plot also shows one of the weaknesses of the selected methods of only focusing on the RVCP because the pole on the real axis, in this case, has a value of approximately -50. However, at around 1 mH grid inductance value, the grid inductance interval before the system RVCP bigger than zero is very short. That means that the interval of grid inductance value should be small, to ensure that the PLL bandwidth is not reduced by an unnecessary amount, which results in unnecessary poor dynamic performance. The exact value should be in the range 0.1-0.5 mH, but experimentation depending on the specific system has to be used here.

3.2.2 Adaptive PLL method

Now, most of the concepts and formalities are defined, and out of the way, the specific adaptive PLL method can be defined. The list below clarifies and repeats all the necessary steps for the adaptive PLL method, in a more concise way than the text from the previous subsection.

1. Define base-case operating point, build the MIMO grid and converter transfer function matrices, and create $\mathbf{L(s)}$ and $\mathbf{L_{cl}(s)}$. Define the lower PLL bandwidth $\omega_{pll,min}$ in regards to grid fundamental frequency.
2. Find upper grid inductance limit $L_{g,max}$ by simulating the system for a large range of high grid inductance values with $\omega_{pll,min}$ as PLL bandwidth. The upper value is when the RVCP changes from a negative to a positive value. A margin can also be included if that is necessary.
3. Find start point of adaptive control by finding the grid inductance level where the RVCP starts moving quickly towards a positive value (see Figure 3.4b).
4. Define grid inductance interval size based on system sensitivity and application.
5. For all grid inductance intervals, find the change in RVCP, which defines reduction need, for the PLL bandwidth specified from the last interval. If it is the first interval, the base-case PLL should be used.
6. Simulate the system for the upper limit of the current grid inductance interval for a range of PLL bandwidths lower than the current PLL bandwidth. For the first PLL bandwidth that reduces the RVCP more than or equal than the reduction needs, break the loop, update the current PLL bandwidth, and enter the next grid inductance interval.
7. When the PLL cannot reduce the bandwidth enough to meet reduction need without having a lower bandwidth than $\omega_{pll,min}$, the gain schedule is completed. The PLL should operate at $\omega_{pll,min}$ until $L_{g,max}$ is reached. If higher values than this are detected, the inverter should be disconnected from the grid. In the case of simulation, this is naturally not a concern.

Explanations like this naturally get messy in a list form, so a simplified algorithm is shown in the flowchart in Figure 3.8. The result of following this flowchart would be a complete list of PLL control parameters for all grid inductance values of interest.

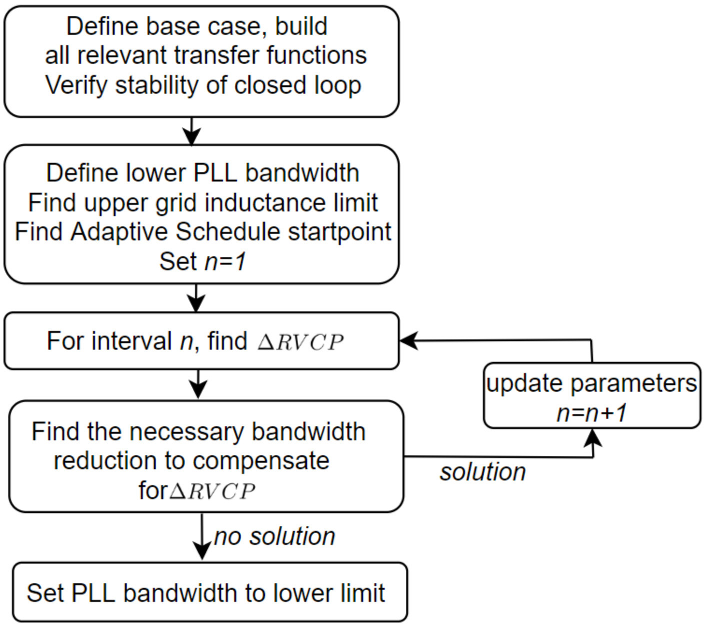

Figure 3.8: Flowchart adaptive PLL.

3.3 Multivariable Adaptive Control

As mentioned earlier, the approach of only adapting the PLL might be incomplete, as the system under study has a PLL and current controller that might interact with each other. Also, there is no guarantee that the current controller is selected with "optimal" parameters in the base-case, both in this thesis and in the general case. Therefore, this section aims at first exploring system dynamics for the converter-grid system under changing PLL bandwidth, current controller bandwidth, and grid inductance level. The reader should consider reading Section 4.1, where the adaptive PLL from the last section was implemented. The reason for this is that some lessons from the implementation of the adaptive PLL will be used directly in this section.

As the previous section, this section is also split into a conceptual part where underlying system dynamics and possible concepts are explored, before the concrete multivariable adaptive control method is presented in Subsection 3.3.2.

3.3.1 Conceptual Design of Multivariable Adaptive Control

Pole Movement and System Dynamics

This section aims at keeping the simplicity of the previously proposed RVCP method, while at the same time remove the weaknesses. One of the differences now is that it is not only PLL bandwidth and grid inductance that has to be balanced against each other, this time the CC bandwidth also has to be taken into account. Therefore, these three system parameters have to be considered altogether, but first, to gain an insight into the dynamics of the system, it is useful to consider how the system behaves when only one of the three varies, and the two others are constant. By considering both the CC and the PLL controller, this means that both the dd and qq-channels are of interest, not only the qq as discussed in the previous section. The PLL will still mainly affect the qq-channel, but the CC affects both. Therefore, to start the exploration of more general system dynamics, consider the plot in Figure 3.9.

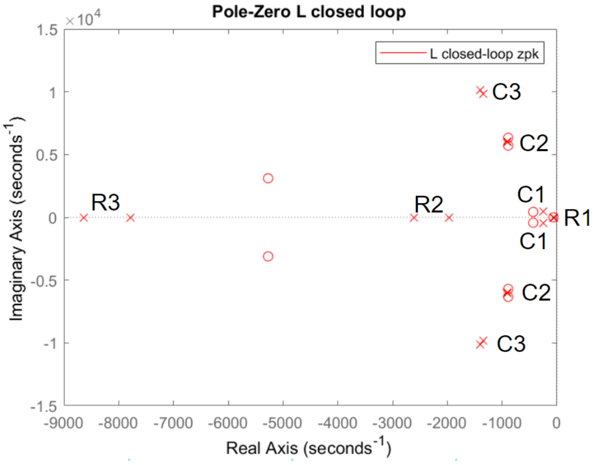

Figure 3.9: General groups of poles and zeros for a minimal realized stable converter-grid system.

Figure 3.9 shows the pole-zero map of $\mathbf{L_{cl}}$ for an arbitrary stable converter-grid system, the difference this time is that poles and zeros close to each other in location is labeled. By just considering this figure, there is no guarantee that these groups stay this way for all systems, but that is considered later. The motivation for doing this is to observe how the different groups move when the controllers and grid inductance are varied, to gain insight into the underlying dynamics of the system, informally and intuitively. One thing that should be kept in mind is that there is no guarantee that for example, a pole on the real axis stays on the real axis when the system is iterated many times. The next thing to do is to see how the groups move when the grid inductance is varied, and control is kept constant for this arbitrary system. The grid inductance is the only varying variable that cannot be directly controlled, therefore this should be covered first.

Therefore, consider the two plots in Figure 3.10. The first plots just show all the poles and zeros, when the system is simulated for a large range of grid inductance values and plotted in the same diagram. But it does not show any general direction or capture the dynamics, and in general, no fundamental understanding can be gained from this plot alone. However, what can be observed is that increasing grid inductance affects some groups more than others. Therefore, the second plot in Figure 3.10b focus on the groups of importance, namely the ones closest to the RHP, which moves significantly by the changing grid inductance. These poles are naturally the dominant poles for system stability. The arrows are in the direction from low to high grid inductance, and the group names are the same as in Figure 3.9.

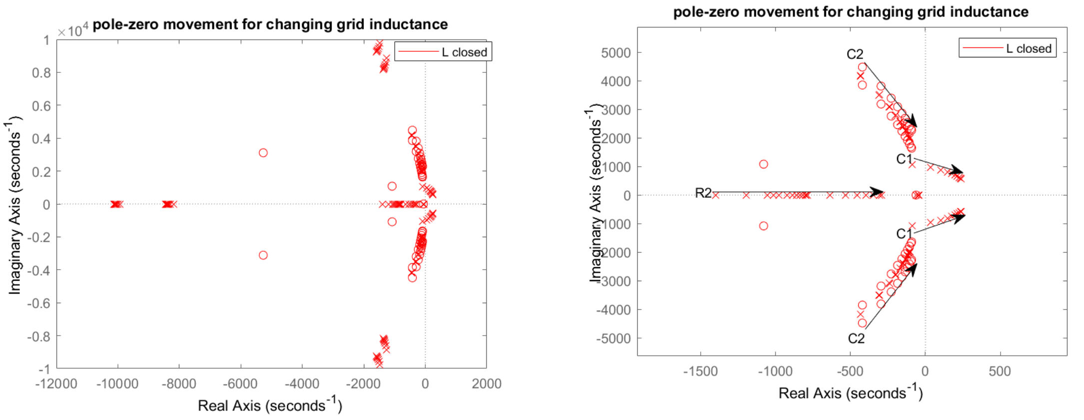

(a) Pole and zero movement for changing grid inductance.

(b) Group movement of poles and zeros for changing grid inductance.

Figure 3.10: General pole and zero movements for changing grid inductance for a minimal realized converter-grid system.

Even though this figure is hard to interpret, some general traits can be observed in Figure 3.10b. First, the main result is that increasing grid inductance moves several of the groups closer to the RHP, which is expected, as all previous results and discussions indicate that a higher grid inductance leads to worse dynamical performance and that the system moves closer to instability. Secondly, the three main groups that move the most are C1, C2, and R2. R1, which in the base-case was the group of poles and zeros closest to the RHP barely moves at all. This is an indication that the RVCP method is a poor measure of system dynamics, at least for low and medium grid inductance levels, as discussed in Section 4.1.

How the poles, and group of poles moves, is not important in itself, the importance is what it can be used for. The intuitive idea would naturally be what can be done to move the critical groups in the other direction, with a combination of the CC and the PLL controller. Therefore, the next step is to analyze these two controllers separately. As the PLL bandwidth tuning has been discussed before, covered in detail in Appendix F.1 this will not be repeated, but this is the first time it is also natural to discuss the CC tuning. Also in this process, the CC behavior can be represented with an equivalent bandwidth variable, w_{cc}, and the details are covered in Appendix F.2. Therefore, without further details, consider the two plots in Figure 3.11, for both the PLL and CC variation. Also this time only the groups with significant movement are focused on.

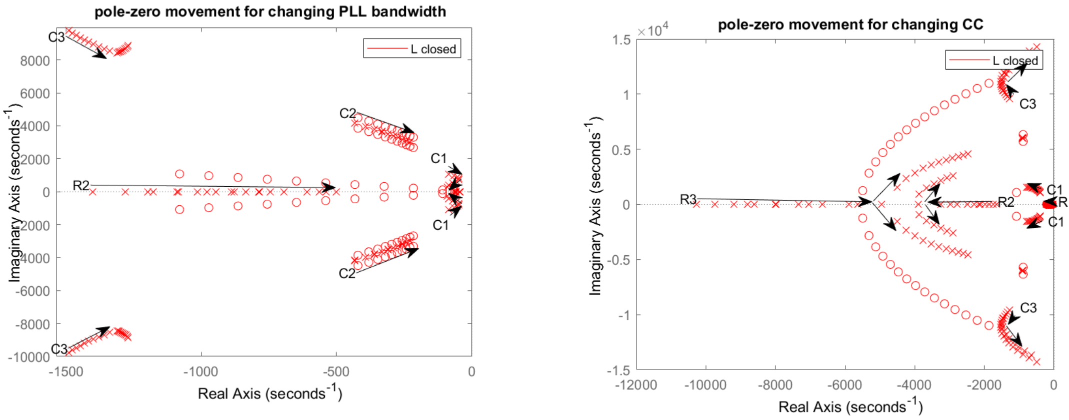

(a) Group movement of poles and zeros for changing PLL bandwidth.

(b) Group movement of poles and zeros for changing CC bandwidth.

Figure 3.11: General pole and zero movements for changing controllers for a minimal realized converter-grid system.

In Figure 3.11a, the PLL bandwidth is changed from a high value to a low value, while the other parameters are constant. This direction is chosen because Section 3.2 showed that increasing grid impedance needs lower PLL bandwidth. The general trend is that the groups that move a lot, all move closer to the RHP with decreasing bandwidth. This is expected, as low PLL bandwidth indicates a slow system response. But this result does not tell the full story, as lower PLL bandwidth also will reduce the resonance between the grid and converter, as discussed earlier. In some ways, the plot is a nice graphical representation of the trade-offs high and low PLL bandwidth gives. But it has little to do with the stability because the groups that move much are far from the RHP. The interesting movement is in C1 but this will be covered later.

In Figure 3.11b, the current controller is simulated in the direction from low to high bandwidth. This is done as it is expected that higher current control bandwidth will lead to faster system response, until a certain point where it gets worse again. This is exactly what can be observed in 3.11b. R1 and C1 move away from the RHP, and in the beginning, C3 does the same. But after a certain point, C3 starts going towards the RHP again, and if the system is simulated for even higher bandwidths, this is the first group that enters the RHP and makes the system unstable. As for R2 and R3 in can be observed that after a certain point, they go from a pole on the real axis to complex conjugated poles, but their movement is in the opposite direction. C2 is not affected by the current controller at all.

The primary motivation for analyzing how the groups move individually for grid inductance, PLL bandwidth and CC bandwidth, which is done in 3.10b, 3.11a and 3.11b, respectively, is to uncover if the CC of PLL can counter the negative effect form grid inductance, and this has do be discussed for each group before the bigger picture can be studied. The list below summarizes the results:

- **R1**. To start with the group that is closest to the RHP for the base-case, R1, the result is conclusive for all three plots. R1 is almost not affected at all by the decreasing PLL and increasing grid inductance, and slightly affected in the positive direction by the CC. This once again shows that the approach of only using RVCP for adaptive control may not be optimal.
- **C1**. For C1 it is shown that increasing grid inductance and increasing CC bandwidth have the opposite effect of increased grid inductance, which is very nice, and should be taken into account when forming the adaptive method.
- **C2**. For C2 the result is not very good, as increased grid inductance moves it closer to the RHP and neither PLL or CC can do anything to avoid it.
- **R2**. Similar to C2, but increased CC bandwidth can move R2 away from the RHP, up to a certain point.

The key here is to use all of the useful information and discard the rest.

Considerations and Concepts

Now that the most important pole dynamics are mapped out, it is time to apply it and form initial concepts for the adaptive control method. A natural extension of the RVCP method would be to consider more than the most critical pole, for example, the four most critical or the ten most critical. If this is to be done, there has to be some sort of weighing mechanism that makes sure that the pole movement close to the RHP is more important than the pole movement far into the LHP. For example, it is not important if a pole moves from -10000 to -9000 in real value, but movement from -50 to +10 is critical information that has to be taken care of. It is also worth considering if some poles should not be considered at all, such as the C2 poles, which are not affected in the right direction by either the PLL or the CC.

Another important aspect that has to be handled is the relationship between how much to adapt the PLL versus the CC. For example, the PLL mainly affects the dynamics in the qq-channel, while the CC affects the dynamics in both channels. If this is not done with great care, there is a possibility that for a certain grid impedance level it may seem that the gain schedule has selected an optimum, but it could be that this optimum is not the global one, i.e. the right combination of PLL and CC control parameters adjustment.

Lastly, any method that does not involve the RVCP will make the system more abstract, because the RVCP is the actual real value of the most critical pole, while any new variables will not tell if the system is stable or not if not proper measure is taken. To serve as an introduction to the concept above, consider the two illustrations in Figure 3.12.

The first plot, in Figure 3.12a, should be familiar. It shows the RVCP as a function of PLL bandwidth for an arbitrary stable converter-grid system. The difference from the last section is that CC bandwidth is included as a variable, and therefore the RVCP is a function of two variables, which results in a surface plot. In this particular case, it looks like the RVCP has a minimum for a high CC bandwidth and a low PLL bandwidth.

The second plot introduces the concept discussed in the previous paragraphs. It is the same stable converter-grid system as in 3.12a, but a new variable called Weighted and Modified Real Value of Critical Poles (WMRVCP) is introduced. The number 14 is, in this case, the number of poles included in the WMRVCP, and it is the 14 poles closest to the RHP. The weighing of the poles should not be focused on for now. As the use of RVCP only suggested that the optimum was located for parameter values of max CC bandwidth and minimum PLL bandwidth, the conclusion from 3.12b is different, as the minimum, in this case, is found for a lower CC bandwidth. The reason for this is that the WMRVCP takes more information into account, and

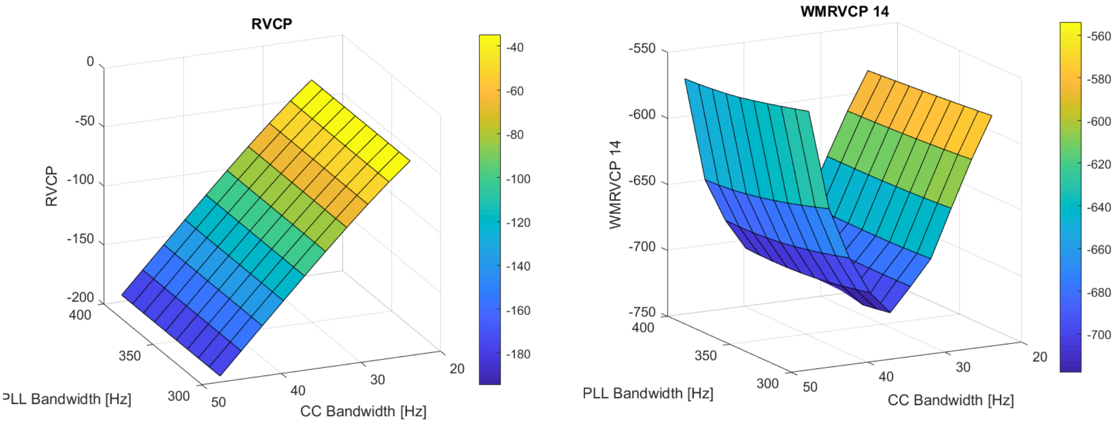

(a) RVCP as a function of PLL and CC bandwidth.

(b) Weighted and Modified RVCP as a function of PLL and CC movement.

Figure 3.12: Pole movement represented as functions of PLL and CC bandwidth.

therefore the suggestion for an optimal combination of control parameters may differ. Naturally, the plots above just serve as motivation to further explore the concept, and nothing general can be said about a general system yet, but it seems that the method of taking more than the most critical pole into account can work.

Selected Concept, Weighted Threshold Variable (WTV)

A selection criterion of interest to explore, is to not care what group the poles are in, but only care about if the real value of the pole is above some specific threshold. This relates to the concept defined earlier of not caring about poles far from the RHP. This solves the mess of finding out which group the pole is a part of because, in essence, this is not relevant. Also, the the summary on how the PLL, CC and grid inductance moves the groups from last page was inconclusive, and no clear methodology emerged from the summary, which indicates that focusing on specific groups may be futile. It also solves the problem of determining how many poles should be included in the aggregate variable, for example 14 as in Figure 3.12b.

However, there are challenges to an approach like this as well, like finding the appropriate threshold value, weighing of the numerical pole value, and the fact that the introduction of a threshold introduces strange surface functions, with little insight in what the optimal operating point would be. Therefore, the next paragraphs will further investigate these challenges to check if this approach is viable.

The first thing to consider is where to put the threshold for where it is considered that pole movement is important. A reasonable place to put the threshold would be at the apex of the C3 group movement, i.e. the lowest real value the C3 group poles takes when the CC bandwidth is varied over a large range of bandwidth values, and the PLL has a high bandwidth. If this threshold is selected, it is ensured that C3 always is inside the threshold and all other poles with a higher real value than this. Furthermore, the choice of this group specifically makes sure that all the groups that move significantly by increased grid inductance are included, and it is easy to define the threshold, as it can be found by just looping over a range of CC bandwidths.

Now that the threshold is defined, the weighing should be selected. There are many ways to do this, but a straightforward one is just to weigh the pole placement in regards to the threshold value. As stated earlier, pole movement close to the RHP is more important than close to the threshold. To concertize, define the threshold as T, and pole number i as p_i. Then the weight W_i of pole number i is equal to the expression in (3.1).

$$W_i = T - \Re(p_i) \tag{3.1}$$

The aggregate variable, which now just is an abstract measure for pole placement, defined as the Weighed Threshold Value (WTV) is equal to the expression in (3.2), if the system has N poles within the threshold.

$$WTV = \sum_{i}^{N} W_i \tag{3.2}$$

It should be considered to have a normalizing factor to divide WTV by so the numerical values are within a reasonable range.

As an example, to motivate why the definition of WTV is useful, suppose a system has two poles within the threshold value, where $T = -1000$, and the real values of the two poles are p_1=-20 and p_2=-800. This results in W_1==-980, and W_2=-200, and WTV=-1180. In this case, p_1 is determines -980/-1180=83% of the total value of the new parameter.

There should be a program running in parallel checking that the RVCP does not enter the RHP, as the WTV does not directly control this. As already stated, the numerical value of WTV does not mean anything in itself, what means something is how this value changes for the system when it is simulated for a large range of CC and PLL values for a given grid inductance. By then looking at surface plots the "optimum" can be determined. Also, the way WTV is defined, the minimum is no longer the optimal point, but the maximum. This comes from the fact that if all the poles are close to the threshold results in very low weights, which results in a value close to zero, while the opposite is true for many poles close to the RHP. As an illustration of this method, consider the two plots in Figure 3.13, which shows the WTV as a function of CC and PLL bandwidth for two different grid impedance values for an example system.

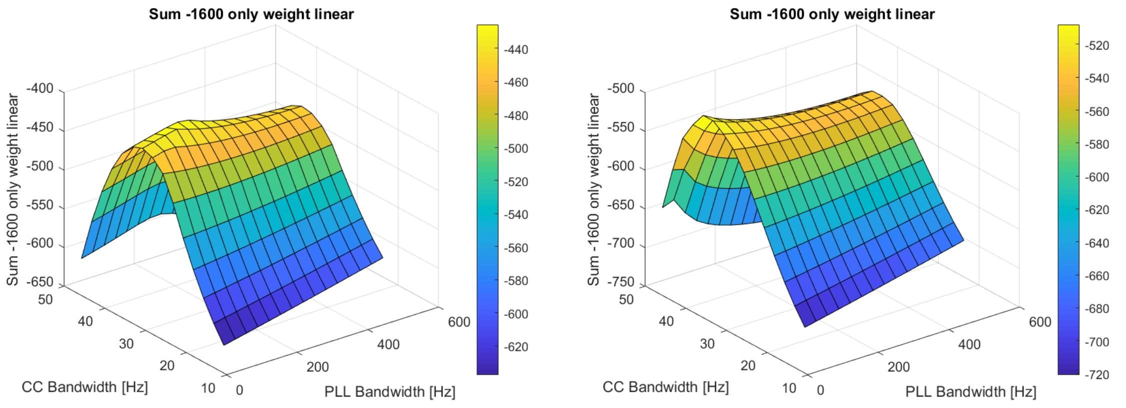

(a) WTV method for a stable system with grid inductance of 0.6 mH.

(b) WTV method for a stable system with grid inductance of 1.8 mH.

Figure 3.13: WTV method for the same system, with two different grid inductance values.

For this particular example, the threshold was selected to be -1600, and the title says that it was weighted linearly, which corresponds to the definition in (3.1). Just to verify that the method does not give odd control parameters, the first plot indicates that the maximum is at around 200 Hz in PLL bandwidth and 35 Hz in CC bandwidth, and for a higher grid inductance value the CC bandwidth is roughly the same, but the optimal PLL bandwidth is smaller. This makes sense, as the PLL should be decreased for higher grid inductance values.

3.3.2 Multivariable Adaptive Control Method

To summarize all the aspects discussed earlier in this section, it is again useful with some sort of list or flowchart for how to implement the WTV method that outputs a multivariable gain schedule.

1. Find the original base-case, select lower grid inductance level L_1 for the gain schedule to start.
2. For the base-case, iterate CC parameters while keeping PLL constant and grid inductance to L_1 to find the threshold based on the placement on the movement of the C3 pole.
3. Refine the base-case by simulating over a large range of CC and PLL bandwidths, select the global optimum given by the WTV. If no global maximum of WTV surface function found, extend the range or lower L_1 or both, and repeat.
4. Global optimum found, set iteration counter n to n=1,
5. Simulate movement of WTV and RVCP in interval n. If RVCP limit not hit, maximize WTV, update control parameters, and n=n+1. If RVCP limit hit, optimize the surface function of RVCP. Update control parameters and set n=n+1. Do this until RVCP gets a positive value, then the gain schedule is finished.

Naturally, this is expressed better in the form of a flowchart, which can be seen in Figure 3.14. By following this flowchart, parameter values for the CC and PLL can be found for every grid inductance interval. This method is implemented for the system under study in this thesis in Section 4.2.

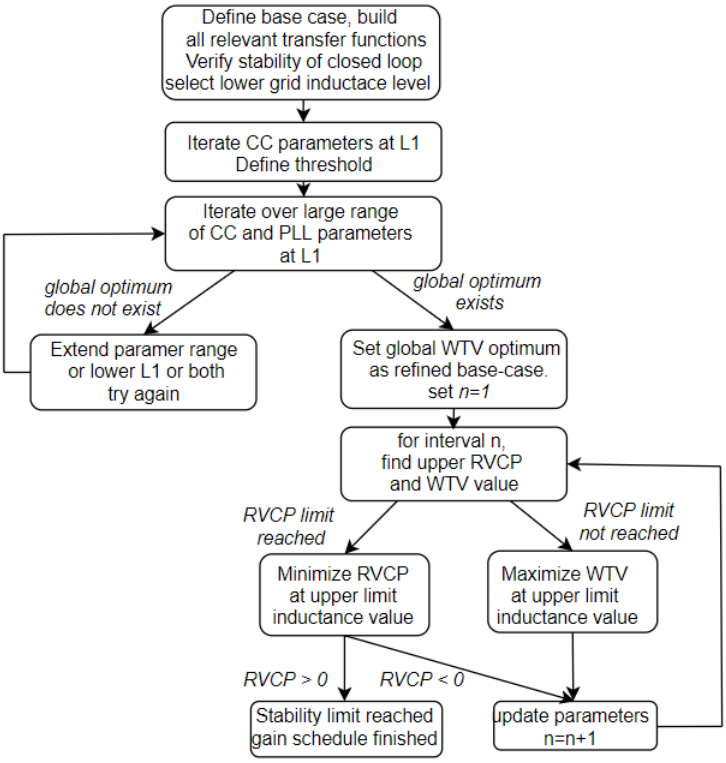

Figure 3.14: Multivariable adaptive control flowchart.

Chapter summary

As this chapter introduced a lot of new concepts and methods, the list below summarizes the most important takeaway from this chapter, in chronological order.

- It was early on selected that $\mathbf{L_{cl}}$ should be used for adaptive control, more specifically controlling the poles of $\mathbf{L_{cl}}$.
- In the first adaptive control method, that only considers the PLL, it was selected that only the qq-channel of $\mathbf{L_{cl}}$ should be considered, and that only the most critical pole should be considered. The RVCP method was based on compensating for higher grid impedance by reducing PLL bandwidth.
- The second adaptive control method adapts both the CC and PLL bandwidth, and both the dd and qq channel of $\mathbf{L_{cl}}$ had to be taken into account. The method is called the WTV method, and is based on taking all the poles within a certain threshold into account and applying a weighing mechanism that depends on where the poles are located in the complex plane, in relation to a certain threshold value.

Chapter 4

Adaptive Control Simulation Results and Analysis

This chapter contains all the simulations in this thesis, and is split into three main parts. Section 4.1 implements the adaptive PLL method based on the Real Value of the Critical Pole (RVCP) from Section 3.2. In addition to just presenting the gain scheduling results, and a short analysis of the results and some details regarding the base-case and Matlab technicalities will be presented.

Section 4.2 implements the multivariable control method from Section 3.3 based on the Weighted Threshold Variable (WTV) and the RVCP. After the results are presented, different controllers are compared to evaluate the performance of the multivariable method.

Section 4.3 implements both of the adaptive control methods in the time-domain, in the form of a detailed Simulink model. Also here the controllers are compared to each other to evaluate the performance.

4.1 Simulation Adaptive PLL Results

This section implements the adaptive PLL gain-schedule described in Section 4.1 for the specific system under study in this thesis. Before the implementation is done, some necessary details about the specific system under study will be presented. If the reader only is interested in the gain schedule results and analysis, it is safe to jump to subsection 4.1.2. After the implementation is done, a comparison to other forms of control is done to serve as a foundation for the discussion of the method in Chapter 5.

4.1.1 System and Simulation Details

The MIMO converter and grid models from Chapter 2 can be now be implemented, and Matlab as the simulation tool in this thesis. The base-case itself is defined in Appendix G and the base-case control parameters in Appendix F, but all relevant parameters and variables are repeated below in Table 4.1 for completeness.

More specifically, the Symbolic Math Toolbox in Matlab was used as especially the MIMO converter model have several very computationally expensive operations, such as inverse of $\mathbf{Z_{oi}}$ to form $\mathbf{Y_{oi}}$, the multiplication of $\mathbf{Z_g}$ and $\mathbf{Y_{oi}}$ to form $\mathbf{L}$, and last but not least the expression for $\mathbf{L_{cl}}$. If this is done with the numerical

Quantity	**Symbol**	**Value**
DC voltage	V_{dc}	700 V
AC RMS phase-phase grid voltage	V_g	400 V
d-channel grid voltage	V_d^s	326.6 V
q-channel grid voltage	V_q^s	0 V
Grid frequency	f_g	50 Hz
Grid inductance	L_g	0.1 mH
Switching frequency	f_{sw}	10 kHz
Filter inductor 1	L_{f1}	400 μH
Filter inductor 2	L_{f2}	350 μH
Filter capacitor	C_f	60 μF
Equivalent grid resistance	R_g	0.5 Ω
Equivalent converter resistance	R_c	0.029 Ω
Filter damping resistance	R_d	0.3 Ω
d-channel current reference	$I_{d,ref}$	71.45 A
q-channel current reference	$I_{q,ref}$	0 A
Duty cycle d-channel	D_d	0.4695
Duty cycle q-channel	D_q	0.0128
Proportional gain, current controller	K_p	0.016
Integral gain, current controller	K_i	0.1007
Proportional gain, PLL controller	$K_{p,pll}$	6.62
Integral gain, PLL Controller	$K_{i,pll}$	7151

Table 4.1: Parameters used in the base-case for this thesis.

values in Table 4.1 directly, Matlab has no chance of computing correct expression for the transfer function, even if other Matlab functionalities are used to try to correct the errors. That means that a total of five symbolic transfer functions are defined in the workspace before numerical substitutions are done. Without going into to much detail, the order of the transfer function were greatly reduced by symbolic computations compared to the numerical one, and also the selected system representation discussed in Section 2.4 made sure the system had a manageable size.

All transfer functions are on factorized form to easily verify the poles and zeros, but in parallel to this the state-space form is used for extracting the actual poles and zeros as this is the recommended working recommendation according to Mathworks [38]. If then the poles calculated from a state-space representation, by computing the eigenvalues of the state-space matrix A, which also is a minimal realization, are equal to the poles of the transfer function representation poles, it is a indication that the system is numerically stable, and that it does not matter what working representation is used because the same information is available from both representations.

As it is already verified that the control parameters for the base-case system makes sense in Appendix F, it will not be covered in depth here, but two plots worth considering is shown in Figure 4.1. In 4.1a both the grid and converter impedance is shown, while 4.1b shows the pole-zero map of $\mathbf{L_{cl,qq}}$. Furthermore, 4.1b confirms that the the selected base-case is stable as there are no RHP poles in $\mathbf{L_{cl,qq}}$ when it is also in known that there are no RHP poles in $\mathbf{L_{cl,dd}}$. Additional information that can be seen in $\mathbf{L_{cl,qq}}$ is that the complex conjugated pole pair closest to the RHP have a lower real value than the pole on the real axis, and as it was defined Section 3.2 that no adaptive measures should take place before this happened, so this is fine as well.

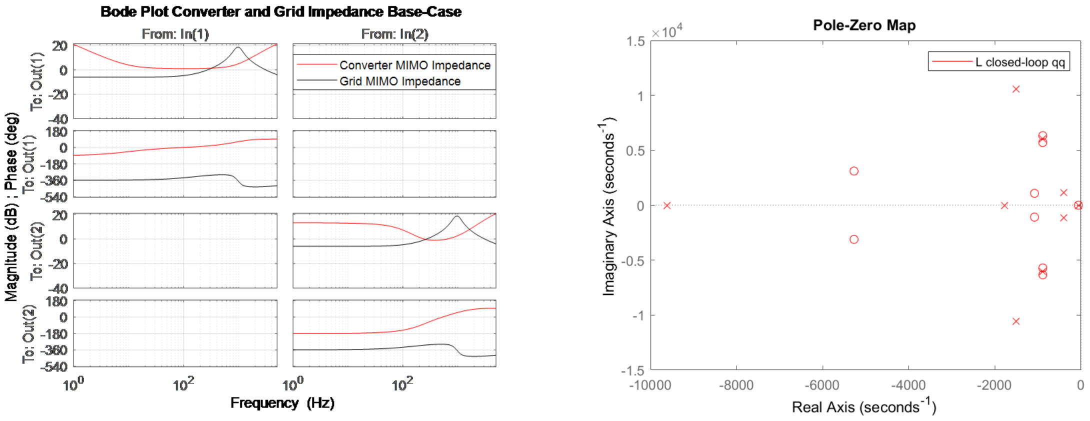

(a) Bode plot of $\mathbf{Z_{oi}}$ and $\mathbf{Z_g}$ for the base-case.

(b) Pole-zero plot of $\mathbf{L_{cl,qq}}$ for the base-case.

Figure 4.1: Base-case plots.

As discussed earlier, there are other ways to confirm that the system is stable, for example by the step response of $\mathbf{L_{cl}}$ or use of GNC on $\mathbf{L}$. For completeness, both these plots are included below in Figure 4.2, but it is the last time this will be done as it is stated earlier that $\mathbf{L_{cl,qq}}$ and its corresponding RVCP that will be used for the adaptive control implementation. The plots confirm once again that the base-case is stable as the step response is relatively smooth, and neither of the eigenvalue loci have any net-rotation around (-1,0) in the complex plane when the extra information that $\mathbf{L}$ has no RHP poles is given.

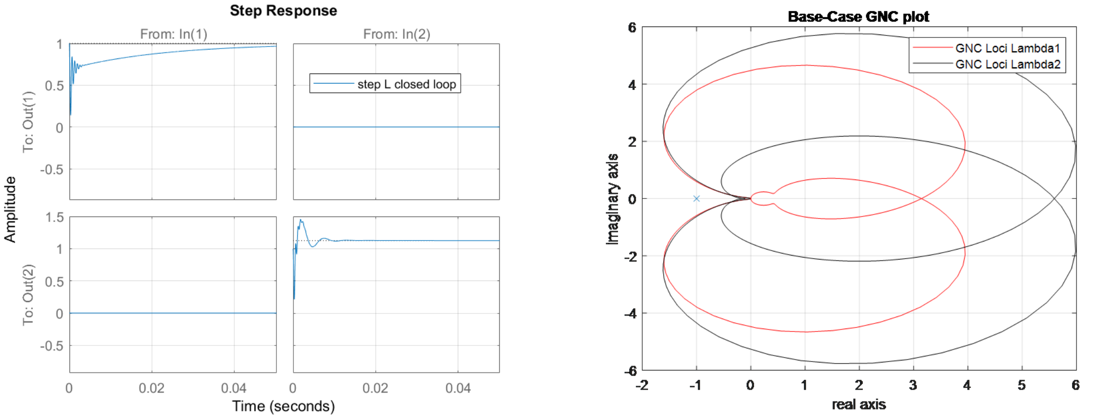

(a) Step-response of plot of $\mathbf{L_{cl}}$ for the base-case.

(b) Eigenvalue loci for λ_1 and λ_2 for $\mathbf{L_{cl}}$ for the base-case.

Figure 4.2: Verification of base-case stability.

Now the actual gain schedule implementation defined by the list in the end of Section 3.2. First, the lower PLL bandwidth limit has to be defined, and as the grid fundamental frequency is 50 Hz, $\omega_{pll,min}$ is defined to be 100π rad/s. The second point on the list is to define the upper grid impedance limit for the system, by simulating the system over a range of grid inductance values when the PLL bandwidth is at the minimum. The RVCP changes sign from negative to positive between the grid inductance levels 5.6 mH and 5.7 mH when the PLL bandwidth is equal to $\omega_{pll,min}$, so the upper limit is therefore defined as 5.6 mH. No margin is chosen in the simulation case, as there is no need for it. Next step is to find the starting point of the gain schedule by simulating the system over a range of grid inductance values, with the base-case bandwidth of 1000π rad/s. The starting point is found to be around 0.6 mH, so this is where the gain schedule will start. The grid inductance interval is selected to be 0.1 mH in the start if the gain schedule, and increased to 0.2 mH later on. The reason for this will become clear when the results are discussed later in this section.

4.1.2 Adaptive PLL Gain Schedule Results and Analysis

Now all details are clarified, and the result from the gain schedule can be seen in Table 4.2. Mind that the numerical values of the RVCP are rounded, as accurate results are of little significance, and also the bandwidth reduction are set not to exactly cancel the need, more like keeping the RVCP more or less in the same numerical range.

Interval	**Bandwidth**	**Lower and Upper RVCP**	**ΔRVCP**	**Bandwidth Reduction**
0.6-0.7mH	500 Hz	-62/-49	13	50 Hz
0.7-0.8mH	450 Hz	-62/-34	28	70 Hz
0.8-0.9mH	380 Hz	-61/-34	27	60 Hz
0.9-1.0mH	320 Hz	-62/-39	23	40 Hz
1.0-1.1mH	280 Hz	-60/-40	20	35 Hz
1.1-1.2mH	245 Hz	-60/-43	17	30 Hz
1.2-1.3mH	215 Hz	-61/-46	15	20 Hz
1.3-1.4mH	195 Hz	-59/-46	13	20 Hz
1.4-1.5mH	175 Hz	-59/-47	12	20 Hz
1.5-1.6mH	155 Hz	-60/-50	10	15 Hz
1.6-1.7mH	140 Hz	-61/-51	10	12 Hz
1.7-1.9mH	128 Hz	-60/-44	16	20 Hz
1.9-2.1mH	108 Hz	-58/-45	13	21 Hz
2.1-2.3mH	87 Hz	-58/-45	13	17 Hz
2.3-2.5mH	70 Hz	-56/-50	6	10 Hz
2.5-2.7mH	60 Hz	-53/-48	5	5 Hz
2.7-2.9mH	55 Hz	-49/-44	4	2 Hz
2.9-3.1mH	53 Hz	-45/-41	4	1 Hz
3.1-3.3mH	52 Hz	-41/-37	4	1 Hz
3.3-3.5mH	51 Hz	-38/-34	4	1 Hz
3.5-3.7mH	50 Hz	-34/-31	3	0 Hz
3.7-2.9mH	50 Hz	-31/-27	4	0 Hz
3.9-4.1mH	50 Hz	-27/-23	4	0 Hz
4.1-4.3mH	50 Hz	-23/-20	3	0 Hz
4.3-4.5mH	50 Hz	-20/-16	4	0 Hz
4.5-4.7mH	50 Hz	-16/-13	3	0 Hz
4.7-4.9mH	50 Hz	-13/-10	3	0 Hz
4.9-5.1mH	50 Hz	-10/-7	3	0 Hz
5.1-5.3mH	50 Hz	-7/-4	3	0 Hz
5.3-5.5mH	50 Hz	-4/-2	2	0 Hz
5.5-5.7mH	50 Hz	-2/1	3	0 Hz

Table 4.2: Adaptive PLL gain schedule.

The numerical values for how the bandwidth and the movement of the RVCP in one interval is not important in themselves, it is the interpretation and analysis of the result which is important, which will be considered next. Mind that the last interval with any update of the PLL bandwidth is 3.3-3.5mH, which is marked with a line. The other place marked with a line in the gain schedule is when the interval length is increased from

0.1 mH to 0.2 mH. The reason for this deviation from the general method was simply that the variable called $\Delta RVCP$ started to move so little compared to the increase in grid inductance, that it was concluded that it was not necessary to have so detailed grid inductance interval anymore. After the final reduction from 51 Hz to 50 Hz there is naturally no more reduction for the PLL as the lower limit is reaches, but the value for the RVCP is still of interest so the simulation is completed until the upper grid inductance limit is hit.

To get a more visual understanding of the results from the development of the gain scheduling, first consider the two plots in Figure 4.3. Figure 4.3a shows how the gain schedule changes the PLL bandwidth as a function of the grid inductance level. In reality, the bandwidth is not a continuous function, it is just a vector, but it of interest to see how it changes over time. The result is clear, the bandwidth must be reduced much more at the beginning of the gain schedule to keep the RVCP relatively constant. One thing worth noticing from the table is that the value for RVCP is kept relatively constant between -62 and -59 until around the grid inductance level of approximately 2.0mH is reached. After this, there is a noticeable decrease in the RVCP even though there is room for more reduction of the bandwidth. The reason for this is that reducing the bandwidth is simply not an as powerful tool as it was lower grid inductance levels. Combined with the fact that the lower bandwidth limit is approaching fast, it was decided that a controlled increase in RVCP was the preferred strategy. This also deviates from the predefined strategy of decreasing the bandwidth until the increase in RVCP was compensated for. If the predefined method was strictly followed the gain schedule would have ended 5 intervals earlier, so it seemed reasonable to do this adjustment to explore the resulting dynamics.

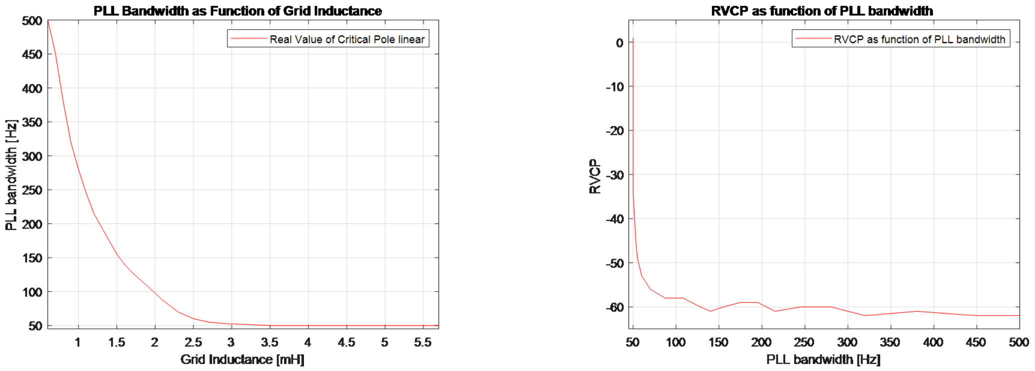

(a) PLL bandwidth as a function of grid inductance.

(b) RVCP as a function of PLL bandwidth.

Figure 4.3: Two visualizations of the gain schedule result.

Figure 4.3b shows the same thing from another perspective, namely the RVCP as a function of the PLL bandwidth. This figure does not give any direct information about the grid inductance, so for this purpose, it is not useful, but it very clearly highlights that the selected PLL gain schedule can control the placement of the RVCP from approximately 500 Hz to 100 Hz, but after this, the RVCP rapidly increases in value, which is a sign that the stability limit is approaching.

It is not very useful to evaluate the adaptive control without any comparisons, therefore the gain schedule PLL should be compared in several ways with more standard methods. This is important to evaluate the performance for itself, but also to see if the method is viable to be further extended for the multi-variable adaptive control method to be implemented later. Therefore consider the plot in Figure 4.4

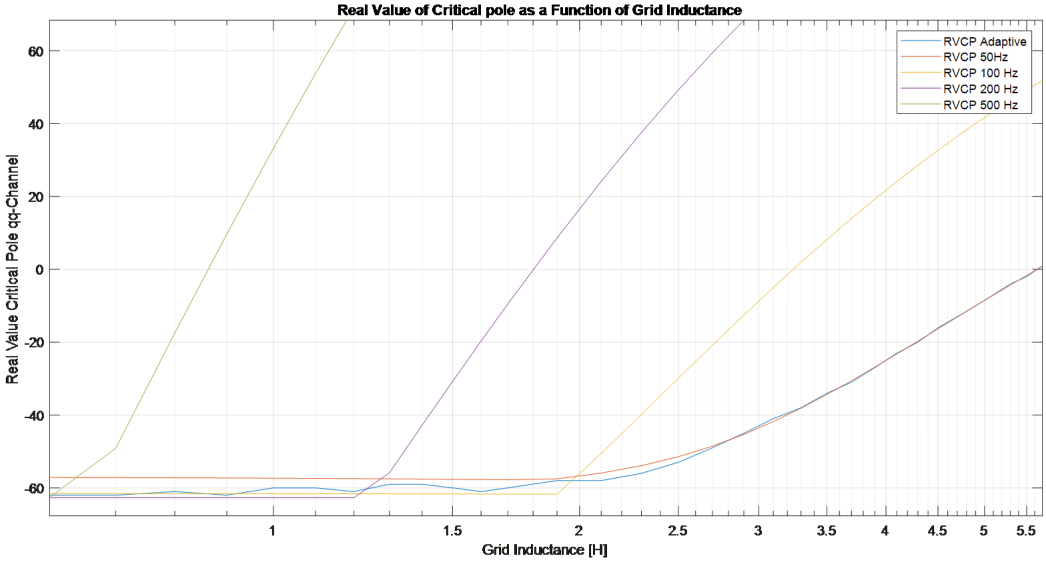

Figure 4.4: RVCP movement for different PLL bandwidths.

As the adaptive PLL is to control the RVCP, A natural way to measure the performance is to compare the RVCP changes for different grid inductance levels, and then compare that to how the RVCP would move with other forms of control. This is what is done in Figure 4.4. The four other PLLs all have constant bandwidth under all grid conditions, and all have the same current control parameters as well. The result is clear for the constant high bandwidth PLLs, the higher the bandwidth, the faster the RVCP changes value from negative to positive. The examples in the figures are 500 Hz, 200 Hz and 100 Hz which go unstable at around 0.87 mH, 1.8 mH, and 3.2 mH respectively. So at least the PLL performs better than having a constant high PLL bandwidth.

However, this is not much of a result, the interesting comparison is how the adaptive PLL compares to a constant low bandwidth PLL, which is a more realistic scenario. It is clear that the two lines follow each other very close, but there are still some remarks to be made. Before approximately 2.7 mH the adaptive PLL always has a lower RVCP value than the constant 50 Hz PLL. This is expected, as the bandwidth is higher, but it is still an important result. After all, it shows that is worthwhile to have adaptive control in the medium grid impedance levels because it improves dynamic performance. However, for grid inductance levels above this value, there is no difference in the value of the RVCP. This is also expected because from table 4.2 the PLL bandwidth reached the lower bandwidth limit in the interval 3.5-3.7mH. The conclusion is therefore that the adaptive PLL has no advantage over a standard low bandwidth PLL in the very high grid inductance range, but that it improves performance in the high, medium and low grid inductance range, if only the RVCP value is taken into account.

However, before a full conclusion can be reached, the method itself must also be discussed as there are potential flaws in just using the RVCP directly without considering how the rest of the system behaves. Naturally, the RVCP is what determines if the system is stable or not, but there are limits to how much useful information that is available in addition to this. Therefore it is of interest to consider how the rest of the system poles and zeros move for different grid inductance levels for the constant low bandwidth PLL and the adaptive one. To guide the discussion consider the four plots in Figure 4.5.

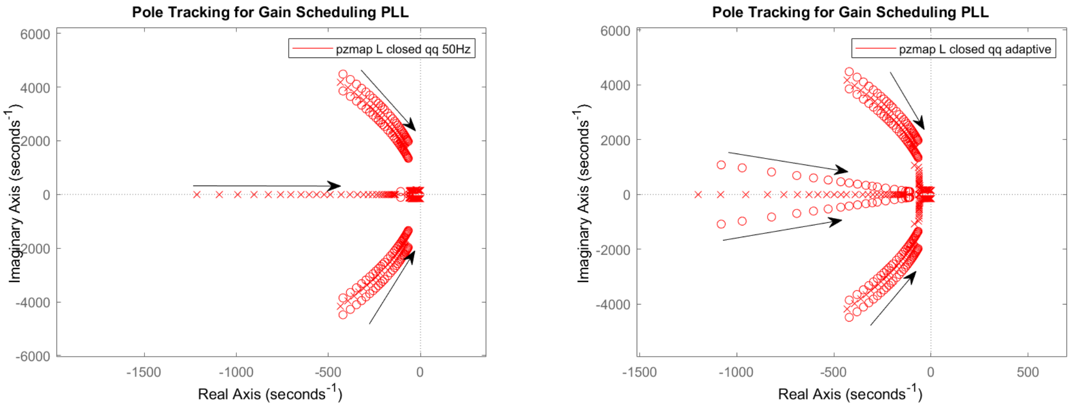

(a) Constant PLL bandwidth.

(b) Adaptive PLL bandwidth.

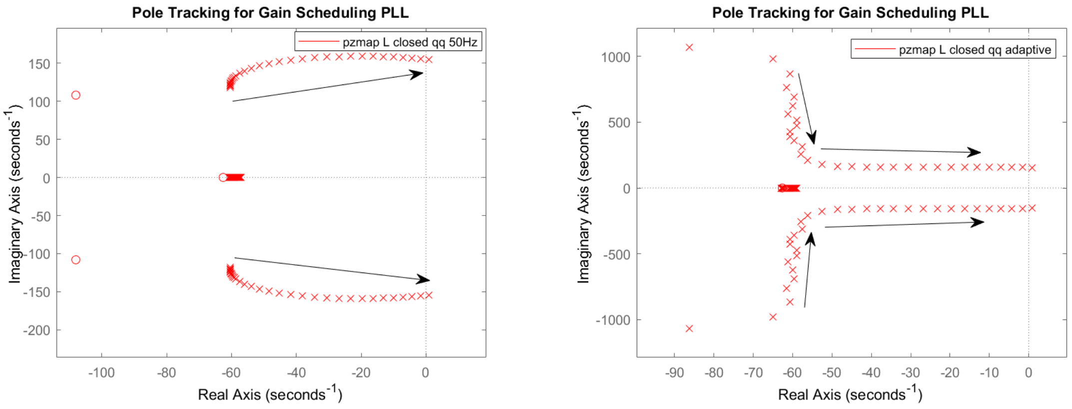

(c) Constant PLL bandwidth zoomed in.

(d) Adaptive PLL bandwidth zoomed in.

Figure 4.5: Comparing poles and zeros movement close to the RHP for constant and adaptive PLL.

The two upper plots shows how several of the poles and zeros closest to the RHP moves, in 4.5a for the constant 50 Hz PLL bandwidth and in 4.5b for the adaptive PLL. As the behavior of the RVCP is already covered earlier in the section, the main motivation for studying such plots is to study how the rest of the system behaves under changing grid inductance levels. The grid inductance level is the same as in Table 4.2, so that means there are 31 pole-zero plots on top of each other to see how the poles and zeros move. The arrows are added to show how the poles and zero movements in the direction of low to high grid inductance.

The first impression of comparing the two plots is how similar they are. The placement seems to not be that much dependent on the PLL bandwidth at all. For example, the complex conjugated pole pair that starts with the highest (in absolute value) imaginary part was measured to not be affected at all by the PLL. i.e the PLL is not able to control this pole placement at all. The same for the pole on the real axis that moves towards the RHP. In addition to the moving zero pair, which is not of much interest, the only clear difference seems to be the poles and zeros closest to the origin. Therefore a zoomed-in version is considered in the two lower plots of Figure 4.5. Mind the different scaling on the real axis. One thing mentioned earlier is the pole on the real axis that does not change much with grid inductance level or PLL bandwidth, and that is clear in both figures. The figures also shows the effect of initiating the gain schedule when the complex conjugated pole pair gets a higher real value than the pole on the real axis.

In the constant 50 Hz case, the complex conjugated pole pair for low and medium grid inductance levels does not move much at all. The reason for this is that the PLL bandwidth is constant low, and therefore no resonance between the grid and the converter. One other big difference is the higher imaginary value of the pole. From the background stability theory covered in Appendix D is known that if a pole on the real axis and a complex conjugated pole pair have the same real value, the complex conjugated pole pair will have a more oscillatory time response. Naturally, the selected method of only using the RVCP as an input parameter for the adaptive PLL does not capture this dynamic, as only the real value is used. This is a clear weakness of the method that will be discussed later, but also it should be noted for further work in the multivariable adaptive control method where both the PLL and the current controller are to be adaptive. The best way to visualize this weakness is the closed-loop step response for the constant 50 Hz PLL and the adaptive PLL for different grid inductance levels, which is done in Figure 4.6.

The grid inductance values are chosen somewhat arbitrarily from a low grid inductance to high grid inductance to compare the two. In the first case, for 0.1mH the gain schedule has not yet started, which means the two first system has a 50 Hz bandwidth PLL and the second has a 500 Hz bandwidth PLL. The result is clear and expected, the high bandwidth PLL gives a much faster response. For the second plot, with grid inductance of 1.2 mH, the result is much more unclear, and the adaptive PLL gives a more oscillatory response with higher overshot and about the same settling time. The last plot is for 2.5 mH and the same result as earlier is clear, the response is pretty much the same.

With the discussion and comparisons above one might ask if the adaptive PLL gives any better performance at all, and if not why not use constant low bandwidth PLL at all times. There is little to no difference in stability limit, and the adaptive PLL gives only better dynamic performance for the low grid impedance levels. RVCP method even seems to give a worse dynamic response by any metric in the medium to high grid impedance area as the 1.2 mH step response figure above shows.

The complete evaluation and discussion will be done later, but there are definitely some valuable results and insights that should be used to modify the adaptive controller for the multi-variable case, and maybe reconsider the use of RVCP as an input to the gain schedule algorithm. However, the adaptive PLL still met the control objective to a large extend, as for low grid impedance levels the dynamic performance is improved, and the stability limit is extended greatly compared to the PLL controller with constant bandwidths with higher bandwidth than 50 Hz, as Figure 4.4 showed.

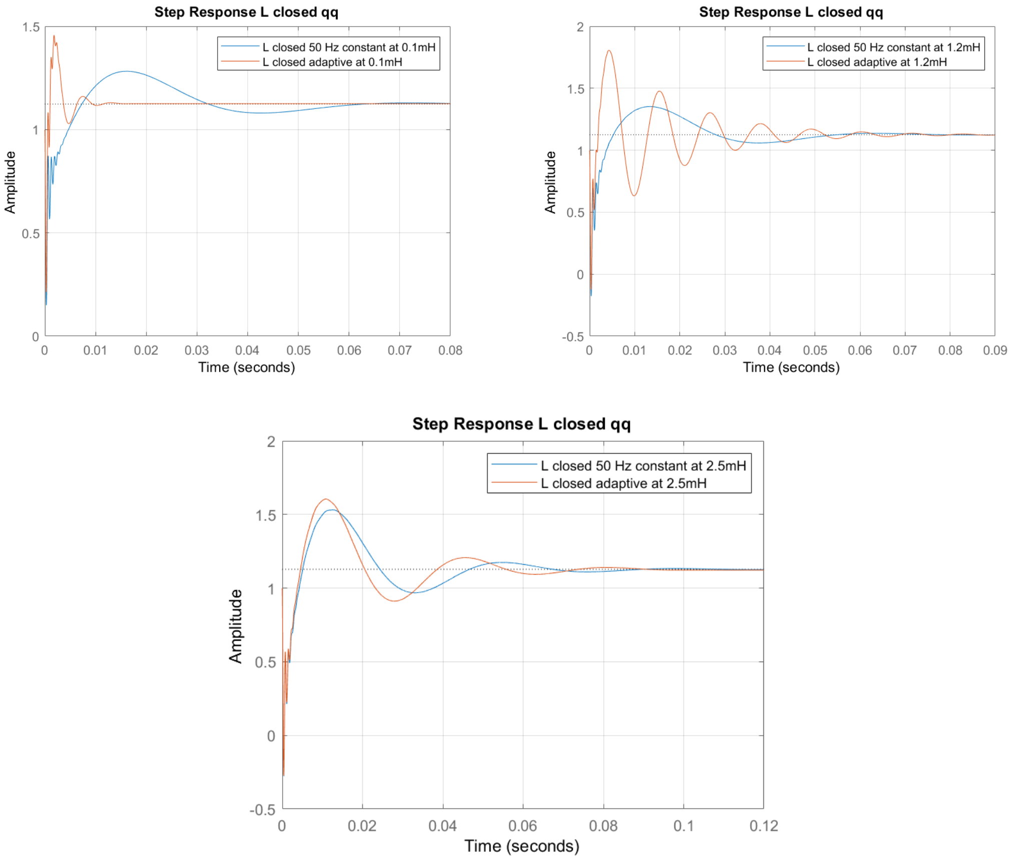

Figure 4.6: Step response for $\mathbf{L_{cl}}$ for grid inductance of 0.1 mH, 1.2 mH and 2.5 mH.

4.2 Simulation Multivariable Adaptive Control Results

This section implements the multivariable adaptive control method from Section 3.3. First the resulting gain schedule is presented, in addition to some simulation details of importance, before a general analysis of the result in Subsection 4.2.2. The previously defined low, medium and high grid impedance cases are analyzed separately in Subsections 4.2.3, 4.2.4 and 4.2.5.

4.2.1 Multivariable Gain Schedule Results

The same system as in Section 4.1 will be used here, so details will not be repeated. By following the flowchart in end of Section 3.3 the gain schedule in Table 4.3 is found.

Interval	CC/PLL Bandwidth	Upper RVCP	Upper WTV
0.0-0.1mH	32/400	-75	-341
0.1-0.2mH	35/383	-93	-369
0.2-0.3mH	35/320	-94	-389
0.3-0.4mH	35/270	-94	-404
0.4-0.5mH	36/225	-100	-415
0.5-0.6mH	36.5/192	-104	-425
0.6-0.7mH	36/160	-101	-437
0.7-0.8mH	36/120	-102	-442
0.8-0.9mH	37/96	-111	-447
0.9-1.0mH	37/75	-112	-452
1.0-1.1mH	37/70	-112	-460
1.1-1.2mH	37/65	-109	-466
1.2-1.3mH	37/60	-103	-472
1.3-1.5mH	37/55	-96	-483
1.5-1.7mH	38/50	-92	-495
1.7-1.9mH	38/50	-93	-512
2.1-2.3mH	38/50	-97	-534
2.3-2.5mH	38/50	-99	-542
2.7-2.9mH	38/50	-102	-555
3.1-3.3mH	38/50	-100	-565
3.5-3.7mH	38/50	-91	-573
3.9-4.1mH	38/50	-77	-579
4.3-4.5mH	38/50	-62	-584
4.5-4.7mH	38/50	-55	-587
4.7-4.9mH	50/50	-117	-762
4.9-5.1mH	50/50	-112	-770
5.1-5.3mH	50/50	-109	-773
5.3-5.5mH	50/50	-98	-777
7.7-7.9mH	50/50	0	-800

Table 4.3: Multivariable adaptive control gain schedule.

Before the analysis of the result can start, some remarks has to be made. Initially, the base-case was the same as the adaptive PLL, namely CC=26 Hz and PLL=500 Hz. In the last section, the gain schedule was defined to start at 0.6 mH, because this was approximately when the most critical pole in the *qq* channel started to move fast towards the RHP. This time a lower value was selected, mostly just to get more out out the gain schedule, and 0.1mH seemed like a reasonable staring point. The interval size was set to 0.1mH.

The next point in the flowchart is to iterate over a large range of CC values while keeping PLL parameters constant and grid inductance to the lower interval value, which in this case is 0.1mH. When this is done, the pole-zero plot in Figure 4.7a gives an indication to where the threshold should be, based on the rules of including the C3 poles. Based on this the threshold was selected to be -1600, i.e. all poles with a higher real value than -1600 is influencing the variable WTV.

Now that the threshold is established, the base-case should be refined to the WTV maximum at 0.1mH, according to the flowchart, and this is illustrated in the surface plot in Figure 4.7b. It can be seen that the global optimum is in the PLL range 400-600 Hz and CC range 30-40 Hz, and if measured accurately CC=32 Hz and PLL=400 Hz is selected. This is the parameters that can be seen in the beginning of the gain schedule in table 4.3.

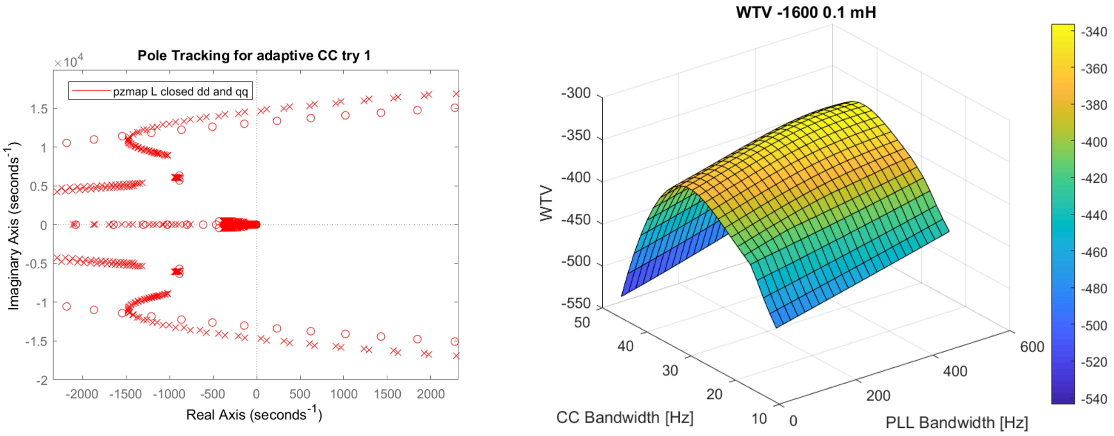

(a) Pole-Zero map for threshold selection.

(b) WTV surface plot at 0.1mH.

Figure 4.7: Threshold determination and refined base-case selection.

The last step before all the grid inductance intervals can be iterated through, is to select the lower RVCP limit where the process should shift focus from maximizing WTV to minimizing the RVCP. Based on the pole placement of the refined base-case, and the behavior observed in the adaptive PLL section, the RVCP limit was selected to be -50, i.e. when RVCP has a lower value than -50, the WTV is optimized with no regards for RVCP.

In table 4.3 there are four lines, indicating certain incidences. The first one indicates that the interval size was increased from 0.1-0.2 mH, mainly because the lower PLL bandwidth limit was approaching fast, and that the WTV numerical value did not change much for each interval. The second line indicates the point where the lower PLL limit is reached, but also the point where the WTV for a very long period gives approximately the same parameters for the CC and PLL that maximizes the WTV function. This particular set of parameter values of CC=38 Hz and PLL=50 Hz is the maximum WTV until the RVCP limit is reached. From the gain schedule, this is not apparent, but if the interval 4.5-4.7mH is simulated the RVCP gets a value higher than -50, which is above the RVCP limit. This means that instead of maximizing the WTV function, now the RVCP is minimized, i.e. all focus is on the critical pole. This can be observed in the gain schedule where the RVCP makes a big jump from -55 to -117, but the WTV goes from -587 to -762, which means that even though the critical pole is moved further away from the RHP, the general tendency of the system gets much worse, if only the WTV is considered.

After this point, a slight modification to the flowchart algorithm was made. The flowchart says that after RVCP is maximized, the next interval should just be simulated and again check if the RVCP limit is reached to determine if RVCP or WTV should be optimized. But if this is done directly, the system will jump form optimizing RVCP in one interval to optimizing the WTV in the next, and just repeat this pattern. Instead of doing this, it was determined that after the RVCP limit was hit for the first time, the RVCP should be optimized for all intervals until the system gets unstable. Therefore it can be seen in the table that after the 4.7-4.9 mH interval, nothing happens with the control parameters. The interval size was kept to 0.2 mH after this, and simulated until the system goes unstable at approximately 7.9 mH. Some intervals are excluded from the table to save space.

4.2.2 Multivariable Adaptive Control, General Analysis

Now that some details about the process have been discussed, the result from the WTV method can be compared to other forms of control. A natural first comparison would be the adaptive PLL from the last section. The first interesting aspect to inspect is how the two methods compare in selecting PLL bandwidths, and this can be seen in Figure 4.8.

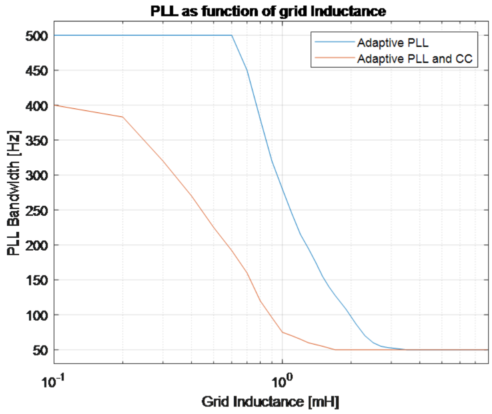

Figure 4.8: PLL bandwidth as a function of grid inductance for the adaptive PLL and the multivariable adaptive control method.

It is clear from the figure the multivariable method gives out a much lower PLL bandwidth for all grid inductance levels until both hit the lower limit. The explanation for this is already implicitly discussed before, the adaptive PLL only care about the RVCP, while the WTV takes multiple poles into account, to give a more refined answer to what the ”optimal” PLL bandwidth is. Naturally, this plot cannot be used to evaluate the performance of the two methods, and another interesting metric would be how the two methods RVCP and

WTV changes over different values. The WTV is not a parameter in the first method, but in practical terms, it can be calculated later, for comparison purposes as done here. Therefore, consider the two plots in Figure 4.9.

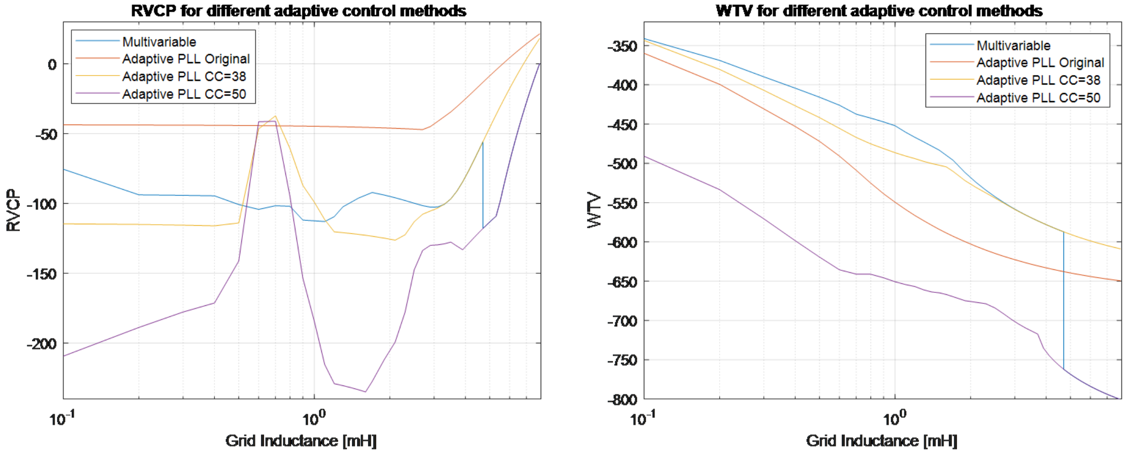

(a) RVCP.

(b) WTV.

Figure 4.9: RVCP and WTV as functions of grid inductance for four different adaptive controllers.

In the first figure, Figure 4.9a, the RVCP is plotted as a function of grid inductance for the multivariable gain schedule and the PLL gain schedule. Also, two other simulations were performed, where the PLL values from the adaptive PLL were used, but more aggressive CC parameters were selected. This was done because it would be unfair to compare the RVCP for two different methods if one of them had poor CC parameters.

The shape of the original adaptive control in red is the easiest to explain because it is just like the last section, the only difference this time is that both channels are included. The RVCP is kept more or less constant until a certain value because that is what the method was designed to do. The multivariable method in blue does not try to control the RVCP in any way before 4.7mH, so there is no point in trying to explain the RVCP curve. If first these two methods are compared, a very nice result it that the multivariable method has a lower RVCP and is stable for a higher grid inductance level than the adaptive PLL. This is not very surprising, as the weaknesses of the RVCP already has been discussed, but it is still a nice result.

One difference not accounted for when only comparing these two figures is the fact that the multivariable methods consistently have higher CC bandwidth, which will influence the RVCP plot. Therefore, the current controller in the original adaptive PLL was increased, to 38 Hz and 50 Hz respectively, as these values indicated good behavior in the multivariable method. These two curves are the yellow and purple curves in Figure 4.9a and 4.9b. This time the result is a bit more unclear. The purple line is for a large portion of the grid inductance range much lower than the multivariable method. Also this time this can easily be explained without even looking at the WTV plot because the adaptive PLL has higher bandwidth both for the CC and PLL for low frequencies, so the RVCP is far intro the LHP. So only using RVCP as a metric it is fair to say that the original adaptive PLL with more aggressive CC parameters performed ”better” than the multivariable method, except for a period approximately in the middle, where there is a sharp increase followed by a decrease in the RVCP.

Naturally, this is only half true because the RVCP is not the variable that is optimized in the multivariable method. Therefore, consider the plot in Figure 4.9b, which has the exact same four systems as in Figure 4.9a, but this time the WTV is plotted instead. This time there is no question about the result, the multivariable method has a higher WTV value over the whole range it is optimized. This is given from the method itself, because the global optimum is selected in each interval, so any other result would indicate a wrong implementation. It is especially clear from this plot that the selection of 50 Hz as CC bandwidth over the whole range is a bad choice since the purple line, in general, has a much lower WTV than all the three other methods. One interesting observation is that it looks like the adaptive PLL with CC=38 is very close to the multivariable method, without this ever being the objective. The simple explanation for this is that the multivariable method has CC parameters in the range 30-38 until 4.7mH, which is close to 38, and that the pole movement effected by this is weighted heavily by the WTV, resulting in similar WTV values.

Just for reference, two more plots are included where the multivariable method is compared to the static controller that does not change. The reason for doing this is if static controllers can achieve the same performance, it would be nice to avoid all the trouble of implementing an adaptive control system. Also, from the last section, it seemed that some static controller performed as good as or better than the adaptive controller, which hopefully is accounted for in the WTV method compared to the RVCP method. As shown in the last section, PLL controller with static bandwidth of over 50 Hz is not interesting for high grid inductance values, as they go unstable, so it is only interesting to compare the multivariable method with static controllers with low PLL bandwidths and high CC bandwidths.

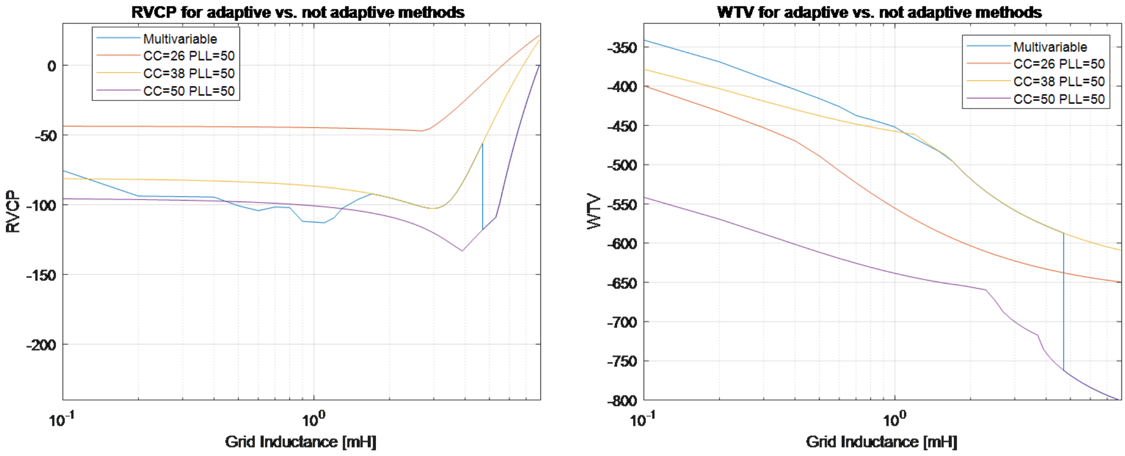

(a) RVCP.

(b) WTV.

Figure 4.10: RVCP and WTV as functions of grid inductance for comparing the multivariable adaptive control and static control.

In all three static cases, familiar CC values are chosen, namely, 26 Hz, which is the original base-case, 38 Hz, which is the WTV optimum for a very large range of grid inductance values, and 50 Hz, which is the CC value that minimized the RVCP for very high grid inductance values.

To start with the WTV values, the conclusion from the last paragraph should still hold which is that there should be no combination of control parameters which results in a higher WTV value than the multivariable method. It looks like there is one point where the yellow line has a higher WTV than the blue line, which indicates that the actual global optimum was not selected. The reason for this is most likely just a little inaccurate selection of control parameters in that specific interval, and it is no big deal since the difference is almost neglectable. Apart from this, the other static controllers have a much lower WTV value over the WTV maximizing range, especially the high CC bandwidth static controller.

From the RVCP plot, the two static controllers with the lowest CC gains go unstable first, which is as expected. The highest CC bandwidth controller also has a consistently low RVCP value compared with the others, as expected, but this comes at cost, as seen in the WTV plot. Other than that it is not much to say. In general, when comparing the multivariable method to other adaptive and static controllers, there are certain combinations from the adaptive PLL and also static parameter selection that achieves ok dynamic performance, but the multivariable WTV method is in general superior, both for the RVCP and the WTV.

As discussed earlier, both the RVCP and WTV are not necessarily a good measure of dynamic performance, so to further compare different control methods it could be useful to evaluate the step response at different grid inductance values. In Section 4.1, the step response was evaluated at three different grid inductance levels, 0.1mH, 1.2mH and 2.5 mH. One of the differences this time is that both channels have to be evaluated, as the current controller influence the step response in both channels. Also, it is worth considering what the multivariable method should be compared to. From the previous paragraphs, there are several interesting alternatives to explore, both from other possible adaptive methods and the static methods. Therefore, all seven cases already discussed are further explored.

4.2.3 Multivariable Adaptive Control, Low Grid Inductance

First, the response at 0.1mH is explored for all the 7 cases. If all cases are in one diagram, it gets very messy, Therefore, they are split in two, in Figure 4.11a and 4.11b.

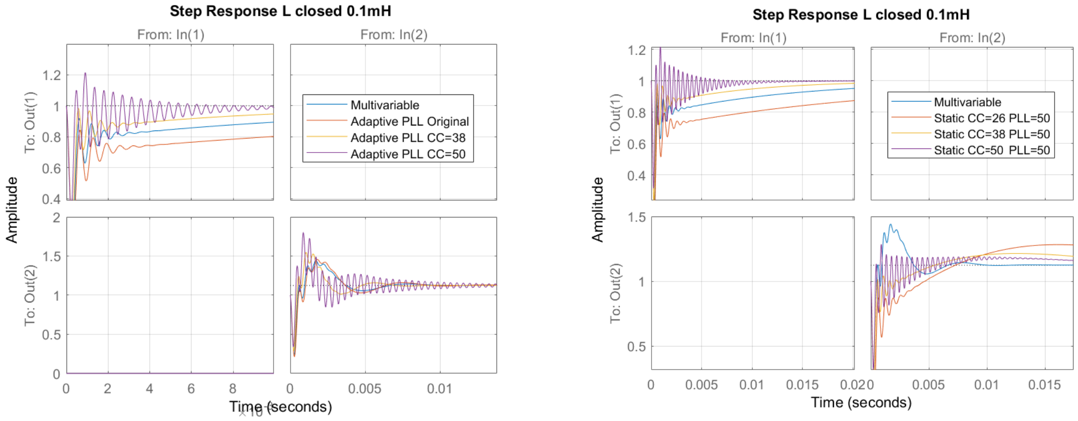

(a) Step response four controllers at 0.1mH.

(b) Step response four controllers at 0.1mH.

Figure 4.11: Step response for seven different controllers at 0.1mH.

In Figure 4.11a, the four different gain schedules from before are compared, and even though the plot is a bit unclear, certain conclusions can be drawn. To start with the dd-channel, as this is easiest to explain because it is formed mainly by the current controller, it is clear that the higher the CC bandwidth the faster the response is, until a certain point where it gets very oscillatory. The original adaptive PLL has CC=26 Hz, the multivariable has CC=32 Hz, and so on. It is fair to say that only looking at this plot, a CC bandwidth of 50 Hz looks to be too high.

In the qq-channel, the trend is similar, but now the PLL bandwidth must also be taken into account. The multivariable method selects PLL to 400 Hz at this value, while the three others all have 500 Hz. However, it looks like the current controller is dominating the response at this low frequency, as the trend is the same in the dd-channel. Also, the response for the multivariable method and the original PLL is very similar. In general, it is difficult to say anything general about this plot, other than that 50 Hz CC bandwidth is probably is to high.

In In Figure 4.11b, the multivariable method is compared to the three static cases defined earlier. This time the effect of the PLL bandwidth appears more clearly in the qq-channel, as the multivariable method has much higher bandwidth and also much faster response. For the highest CC bandwidth is the same as earlier, it looks like it is to high. Based on this plot alone the static controller in yellow looks to perform quite good, which also matches with the intuition from the RVCP ad WTV plots earlier.

4.2.4 Multivariable Adaptive Control, Medium Grid Inductance

Now the grid inductance is increased to 1.2 mH, and this time it is fair to say from Figure 4.12a that the multivariable method step response is much better than the three other adaptive methods. The main reason for why the multivariable method has a much smoother step response in the qq-channel, is already discussed earlier.The WTV method selected lower PLL bandwidths than the RVCP method alone, in this case the first have PLL=60 Hz and the latter have PLL=215 Hz. In the dd-channel it still looks like 50 Hz of current controller bandwidth is to high.

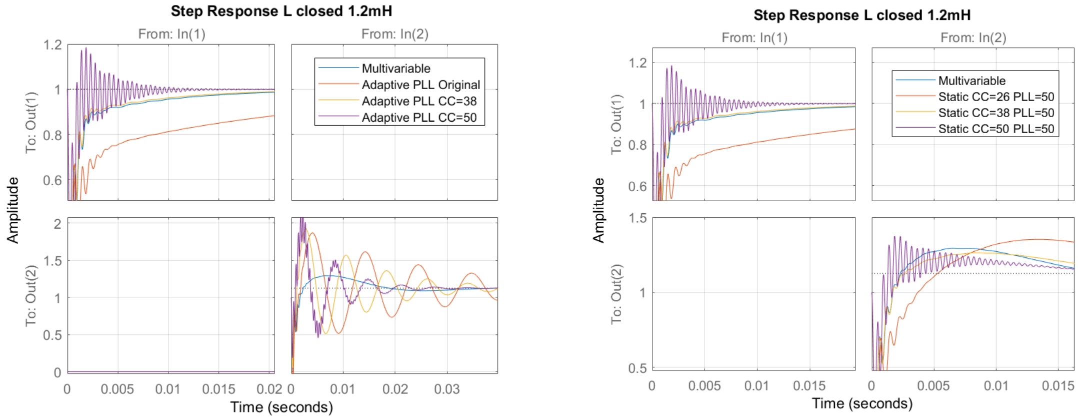

(a) Step response four controllers at 1.2 mH.

(b) Step response four controllers at 1.2 mH.

Figure 4.12: Step response for seven different controllers at 1.2 mH.

When comparing with the static controllers, it is a bit more unclear again from the qq-channel alone. It certainly looks like both the 50 Hz and the 26 Hz versions are sub-optimal, but again the static controller in yellow performs quite good, and certainly better than the other adaptive controllers, except the multivariable method.

4.2.5 Multivariable Adaptive Control, High Grid Inductance

At 2.5 mH, the strong oscillatory response from the other adaptive controllers seems to be gone. In the dd channel in Figure 4.13a, the multivariable response seems to be missing, but it is only covered by the yellow line because for this case they have the same CC parameters. Other than that, not much interesting is happening, the multivariable method looks to have the smoothest response in the qq-channel.

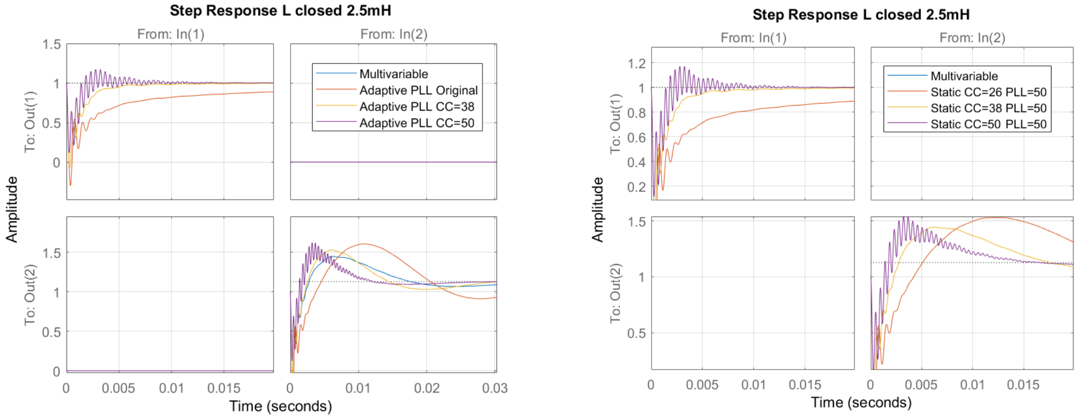

(a) Step response four controllers at 2.5 mH.

(b) Step response four controllers at 2.5 mH.

Figure 4.13: Step response for seven different controllers at 2.5 mH.

Also when compared to the static controllers, the multivariable line is hidden behind the yellow line, this time in both channels, because in this case they have exactly the same PLL and CC parameters, and therefore also the exact same response.

Like the last section, it could also be useful to look at the pole trajectories for different methods, but this is dropped this time, because it is rather messy, and no new significant information will be obtained. The results from the RVCP, WTV and step responses should be more than enough information to evaluate the multivariable method.

In general, it is fair to say that the multivariable method performs very well compared to the other adaptive and static methods. The method provides stability for as long as all other methods, while at the same time have low RVCP values and better dynamic responses than the other methods. If the control objective only is to keep the system stable for as high grid inductance as possible, the user might as well select the adaptive PLL with CC=50 Hz or the static method with PLL=50 Hz and CC=50 Hz, but as shown these two methods have very poor step responses for lower grid inductance values. As for the static controller with CC=38 and PLL=50, this one might be the second-best alternative as it has a very good WTV value compared to all other methods, and in general, has a good dynamic performance. But if no measures are taken this version goes unstable at a lower grid inductance level than the adaptive. Therefore, in regards to the control objective, the multivariable WTV methods archives superior performance compared to all other methods explored, which is a great result.

4.3 Time-Domain Implementation of Adaptive Control Methods

As the two previous sections use fairly abstract models for determining the control parameters, it will be useful to see how this works when implemented in a real system. Experimental validation is left for future work, due to laboratory unavailability in the period March-June 2020, due to the COVID-19 Pandemic. As laboratory implementation was not an option, another possibility is a detailed Simulink switched converter model, which is considered in this section, where elements from the adaptive control methods developed in Section 4.1 and 4.2 is tested out.

It turned out that a direct translation to the switched converter model in Simulink was easier said than done, and some details about the model itself, and necessary adjustments can be found in Appendix I. This section will just present the results after the necessary adjustments was made. The same three grid inductance cases of low, medium and high grid from the previous two sections will also be used here.

As presented in Appendix I, not all seven controllers from the last section will be analyzed in the time-domain as well, since there is no need for it, since several of the controllers overlap in performance. In addition to the two adaptive controllers, two static controllers will be used for comparison in this section, because if they are chosen appropriately, all the interesting dynamics are captured.

The first static controller is defined as the ”balanced case”. It has static control parameters where neither the CC or the PLL bandwidth will be very high or very low. The point of doing this is to have a controller that hopefully will perform well under most grid inductance levels i.e. a balanced controller, but at the cost of going unstable at a lower grid inductance level that the adaptive cases. It is chosen to have a PLL bandwidth of 200 Hz, and a CC bandwidth of 38 Hz, with the same definition of bandwidth used earlier in this thesis, but adapted to a per-unit control system.

The second static case is defined as the ”Aggressive Case”, with high CC bandwidth and low PLL bandwidth. More specifically, the CC bandwidth was selected to 50 Hz and PLL bandwidth 50 Hz. This combination was shown in the last section to be stable for a very high range of grid inductance values, but in general, have a bad performance. Therefore, it would be interesting to see how both of these two static cases perform in the time-domain, and in general, for all four cases see if the same trends as earlier can be observed.

From the Simulink model, there are many interesting variables and parameters that can be analyzed, but to keep it simple, this section mainly focuses on the d-current and the corresponding time-domain phase currents, and the output of the PLL. It should be kept in mind that the step responses, RVCP, WTV, and pole placement of $\mathbf{L_{cl}}$ are not directly translatable to the plots studied and analyzed in this section. However, the stability conclusion should most definitely be the same, as they are two different models of the same system.

It is also important to keep in mind that it is futile to try and analyze the PLL output and d-current response separate from each other. As discussed so many times earlier in this thesis, if the wrong grid angle is used in the $abc - dq$ and $dq - abc$ transformations, there is no reason to believe that the current controllers can operate correctly. Only in steady-state the d-current response can be analyzed separately, but at least for this section, the steady-state is not of interest.

The influence can also go the other way, because for example when there is a step response in the grid current, this will affect the grid voltage, which again will influence the PLL, as will be seen in all the PLL output plots in this section. There will also be some initial synchronization effects, but this will not be focused too much on.

4.3.1 Time-domain Implementation, Low Grid Inductance

The first case is the base-case grid inductance, 0.1mH. As the important traits of the system are the PLL output and the current controllers' ability to follow the reference in d-current, this is considered in Figure 4.14.

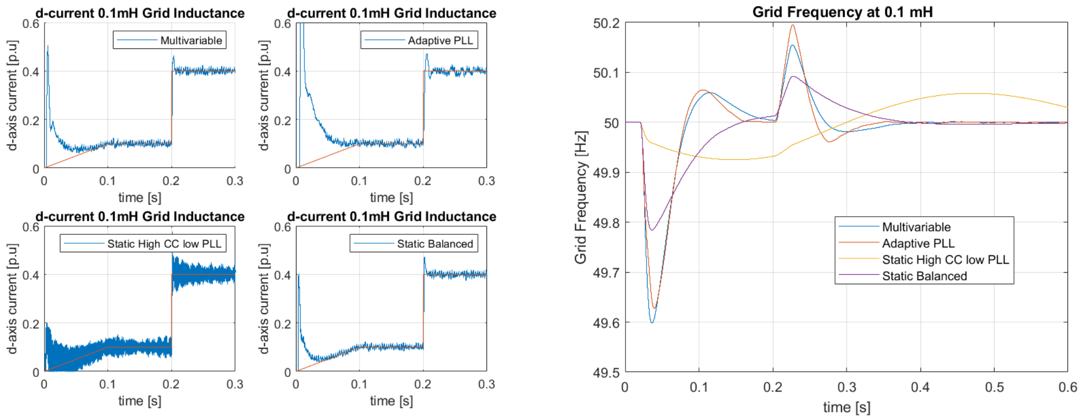

(a) d-current response for the four control cases at 0.1 mH.

(b) PLL output for the four control cases at 0.1mH.

Figure 4.14: Performance plots for the four controllers at 0.1mH.

Before the two plots are analyzed, the underlying information for what the models do should be revisited, to form an opinion on what should be expected. The four plots have CC bandwidths of 32 Hz, 26 Hz, 50Hz, and 38 Hz, in the same order as in Figure 4.14b and all these should be familiar from the last section. The PLL bandwidths are 400 Hz,500 Hz, 50 Hz, and 200 Hz and in the same order. As all these cases were analyzed in the last section, it is expected that the multivariable and the balanced static case has good dynamic performance, while it is expected that the adaptive PLL case has slightly too high PLL bandwidth and slightly too low CC bandwidth, compared to the two previous cases. The aggressive static case is expected to have very poor dynamic performance, due to high CC bandwidth and low PLL bandwidth.

In Figure 4.14a the d-current reference and the actual d-current is plotted against each other. While all the cases are stable, as expected, the current controller in the aggressive static case is poorly tuned. Also, the PLL response is in this case very slow compared to the other three cases. Another interesting aspect that can be observed for the adaptive PLL, is the effect a wrong PLL output has on the current controller. This is especially clearly seen in the initial synchronization of the simulation for the adaptive PLL, where the grid current is far from the reference for a long period compared to the other three cases.

The analysis from these two plots should be sufficient, but now that a complete model is used, also the time-domain currents and voltages can be studied easily. Therefore, consider the phase-currents on the grid side for the multivariable case and the aggressive static controller case in Figure 4.15.

What is meant by ”grid side” in this case is that the measurement is done after the second filter inductor, seen from the converter, i.e. when the switching ripple and most of the high frequency harmonics are filtered out. Naturally these two plots have the exact same information as the d-current plots above, just now that they are after the filter, and in the time-domain. Therefore, the result should be the same, and that is also the case.

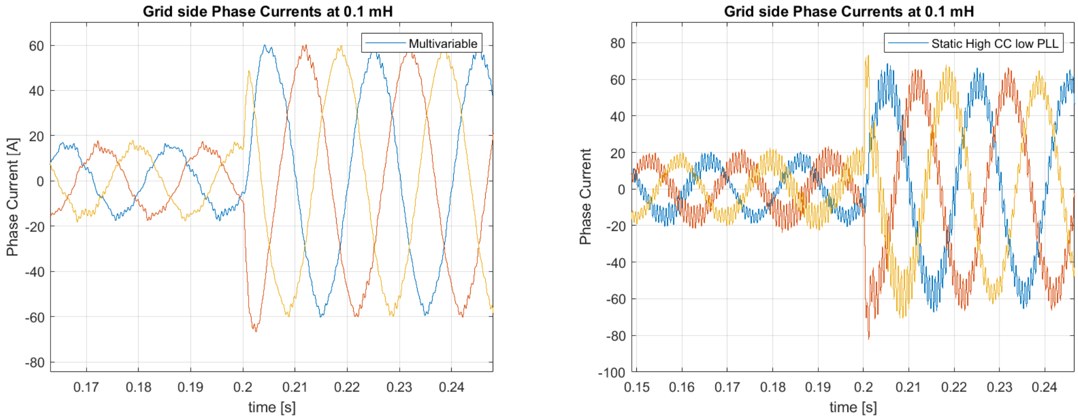

(a) Phase currents multivariable case 0.1mH. **(b)** Phase currents aggressive static case case 0.1mH.

Figure 4.15: Comparison of phase currents multivariable case and static aggressive case at 0.1mH.

While both of the cases are distorted compared to a pure sine wave, the phase currents in Figure 4.15a clearly have a better shape than in Figure 4.15b, where it is clear that the current controller have to high bandwidth. In general the result was as expected for the 0.1mH case, so the next case is 1.2 mH.

4.3.2 Time-domain Implementation, Medium Grid Inductance

The second case is grid inductance equal to 1.2mH, and again the d-current response and PLL output is studied, in Figure 4.16.

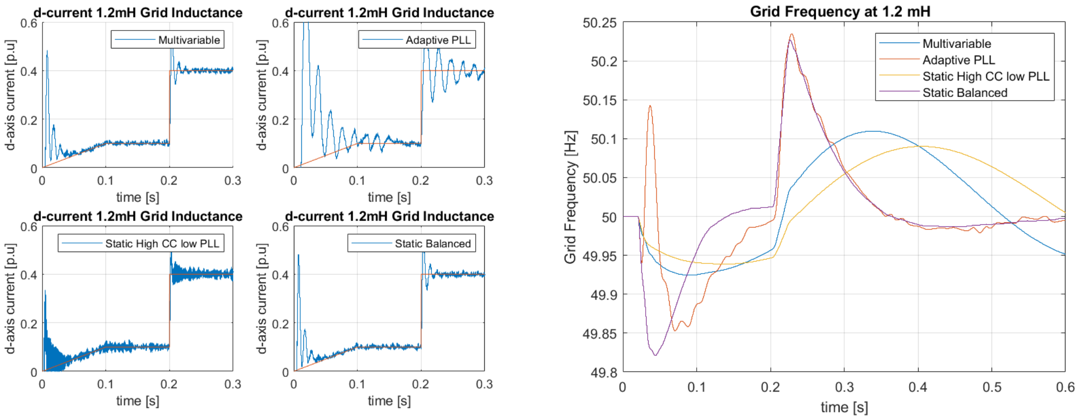

(a) d-current response for the four control cases at 1.2 mH. **(b)** PLL output for the four control cases at 1.2mH.

Figure 4.16: Performance plots for the four controllers at 1.2mH.

This time the CC bandwidths are 37 Hz, 26 Hz, 50 Hz and 38 Hz and the PLL bandwidths are 60 Hz, 215 Hz, 50 Hz and 200 Hz in the same order as in the figure. Naturally, the static cases does not change, and the two adaptive cases are updated from the gain schedules in Tables 4.2 and 4.3. The conclusion from last section at 1.2 mH was that the multivariable case was very good, the adaptive PLL case was very oscillatory in the qq-channel due to the high PLL bandwidth and low CC bandwidth compared the other cases. For the aggressive static controller, poor but stable dynamic performance is still expected and for the balanced static case the response should still be good, as the moderate PLL bandwidth still should not be a problem yet.

To start with the PLL output, the response for the adaptive PLL case and the balanced static case are very similar, as the two bandwidths are very close in this case. Also, the multivariable and the static aggressive case have similar PLL responses, as the multivariable case is already close to the lower limit.

The first impression one might get from the d-current plots is how oscillatory the adaptive PLL case is. This is not very surprising when considering that the control parameters suggested by the underlying method only cares about the most critical pole. Also this time the multivariable case and the balanced static case have a very similar response, even though the bandwidths are very different. There are few differences in the aggressive static case, but the response might seem a bit better than the last case, and this is not too surprising as the RVCP plot in Figure 4.10a showed that the RVCP got further away from the RHP without doing anything with the controller. All in all the result at 1.2 mH matches very well with the results from the last section, with the highlight being how bad the adaptive controller is at medium grid inductance values. Just to highlight this before the 2.5mH case is analyzed, consider the plot in Figure 4.17 where this time the d-currents for the four cases are plotted in the same diagram.

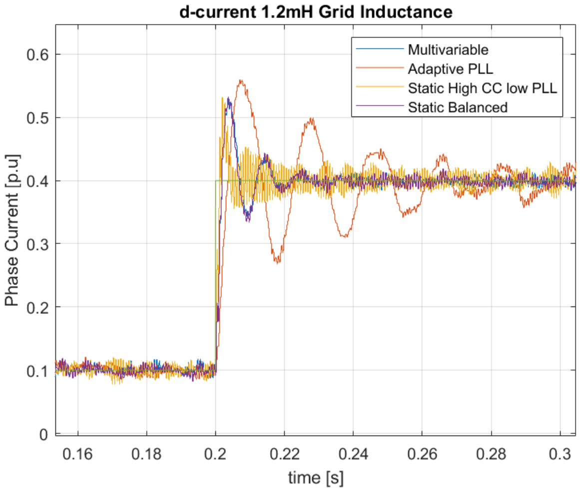

Figure 4.17: d-currents for the four cases at 1.2 mH.

It is clear from the figure that the control parameters in the adaptive PLL case has the worst performance, and that the multivariable case and static balanced case have the best performance.

4.3.3 Time-domain Implementation, High Grid Inductance

Now to the final case from the last section, 2.5 mH. The d-currents and PLL outputs are once again plotted, in Figure 4.18. The CC bandwidths are 38 Hz, 26 Hz, 50 Hz and 38 Hz and PLL bandwidths are 50 Hz, 60 Hz, 50 Hz, and 200 Hz. It is now expected that the static balanced case has too high PLL bandwidth, which will lead to oscillations. The rest is a bit unclear from the step responses in Figure 4.13, as it could look like the gap between the static aggressive case and the multivariable case has been bridged. Also at this point, the adaptive controller would start to have significantly poorer performance due to the lower CC bandwidth that the rest of the controllers.

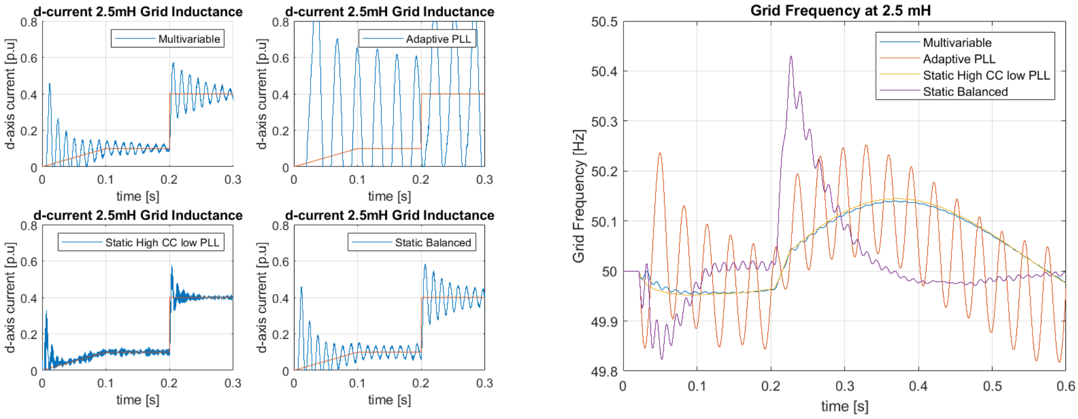

(a) d-current response for the four control cases at 2.5 mH.

(b) PLL output for the four control cases at 2.5 mH.

Figure 4.18: Performance plots for the four controllers at 2.5mH.

The adaptive PLL case is the first thing noticed in both the plots, as the PLL output does not have a steady-state value, and the current controller is unable to follow the reference. Depending on what definition of ”unstable” is used, one might argue that since there is an oscillation around a certain point, the system is not unstable, but for all practical purposes, the current injected into the grid by the adaptive PLL case in no way resembles sine waves. It should be noted that the axis in Figure 4.18a is on purpose equal in all for cases, to easier compare them.

It is a bit surprising, considering the previous analysis, that the adaptive PLL is the first to go unstable when also the static balanced case was thought to be unstable at this high grid inductance level. The static balanced case has almost the same performance as the multivariable case, and this is also the first time where it looks to be clear that the static aggressive case has the best dynamic performance. This may indicate that the WTV method used for the multivariable case suggests using a too low CC bandwidth. To illustrate how much better the performance is in the aggressive static case, compare the grid-side phase currents in Figure 4.19.

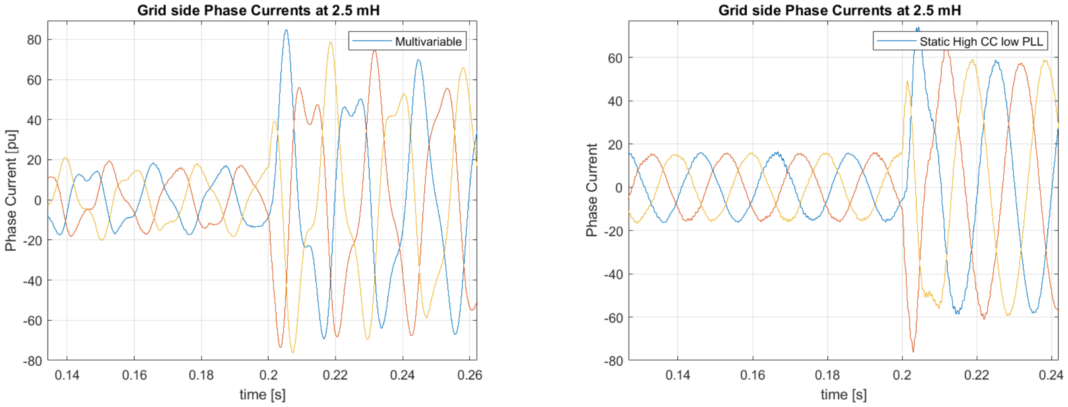

(a) Phase currents multivariable case 2.5mH.

(b) Phase currents multivariable case 2.5mH.

Figure 4.19: Comparison of phase currents multivariable case and static aggressive case at 2.5mH.

Once again, it is focused on the response right around when the d-current reference makes a step and it should be noted that the multivariable case has a nice steady-state operating point. But only considering the two plots above, it is clear that the response for the aggressive static case is much better than the multivariable case. As the two systems have the same PLL bandwidths now, the only difference is the CC bandwidth, so therefore this figure highlights the importance of not only adapting the PLL for changing grid conditions but also the current controller. It also highlights the fact that even though the WTV is maximized in the dq-domain, this may not indicate ”optimal” behavior in the time-domain, which again means there is room for improvement in the the method, or the translation to the time-domain could be improved, or both.

4.3.4 Time-domain Implementation, Very High Grid Inductance

One last case is also considered here because some points from the last three cases was not highlighted clearly enough. Therefore, an even higher grid inductance of 5.0 mH is considered in this section. The CC bandwidths are 50 Hz, 26 Hz, 50 Hz, and 38 Hz and the PLL bandwidths are 50 Hz, 50 Hz, 50 Hz, and 200 Hz. The multivariable method has already reached the limit for when the RVCP is optimized instead of the RVCP, so the aggressive static case is equal to the multivariable case. As the adaptive PLL already failed at 2.5 mH, it should fail now as well, and also the moderately high PLL bandwidths in the balanced case should lead to stability problems now.

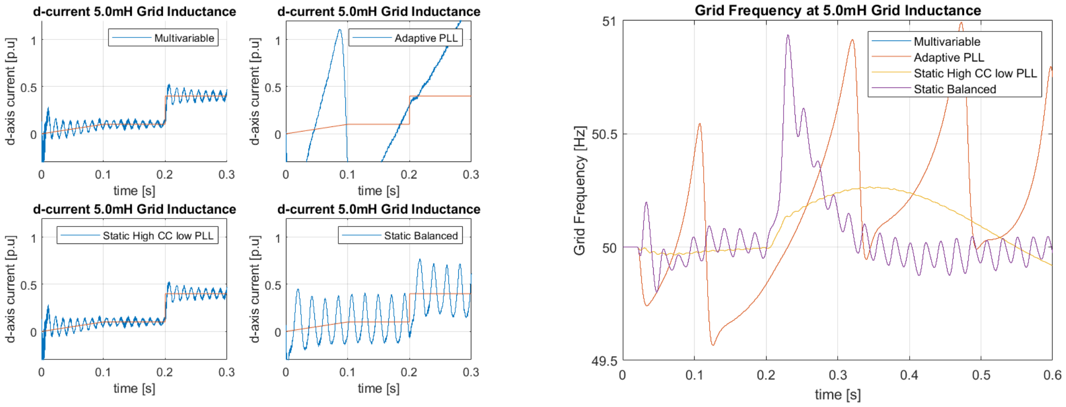

(a) d-current response for the four control cases at 5.0 mH.

(b) PLL output for the four control cases at 5.0 mH.

Figure 4.20: Performance plots for the four controllers at 5.0 mH.

From the figure, it can be seen that the adaptive case is even worse than before, as expected, but now also the static balanced case is not functioning properly. As expected, the response for the static aggressive case and the multivariable case are equal now, as they have the same control parameters.

The main discussion for all the results from this section will be done in Chapter 5, but just to sum up this section, it is generally fair to say that the same trends from the analysis of $\mathbf{L_{cl}}$ also holds for a time-domain Simulink model, when it comes to the relation between CC bandwidth, PLL bandwidth, and grid inductance. Naturally, there is some difference here and there that was unexpected, like that the adaptive PLL failed at a lower grid inductance level than expected, and that the static balanced case lasted for longer than expected. It also looked like the WTV method outputs a to low CC bandwidth, from the analysis for the 2.5 mH case. But the underlying trend on how the controllers should move in relation to grid inductance is consistent in both sections, and that is the most important takeaway from this section.

Chapter summary

As this chapter explored many different simulation cases, it may be difficult to extract the key takeaways from this chapter. Therefore the list below summarizes the most important aspects form this chapter.

- Section 4.1 implemented the adaptive PLL which resulted in a complete gain schedule over the full grid inductance range. Even though stability was ensured until 5.7 mH, which increased the stability limit, there was clear room for improvement.
- Section 4.2 implemented the multivariable adaptive control method, which resulted in a complete gain schedule that increased the stability range compared with the adaptive PLL. First, a general comparison to other forms of control was done, which indicated that the multivariable method was a very good compromise compared to other controllers, which after that was confirmed by the low, medium and high simulation cases.
- Section 4.3 used the results from the two developed adaptive control methods in a switched Simulink model. In general, the same results could be observed, and once again it showed that over the full grid inductance range, the multivariable method performed much better than all other controllers that was tested. However, the simulation results indicated that the adaptive PLL was even worse than in the dq-domain, and also the multivariable method showed some weaknesses, which means that the methods can be improved, and that more efforts should be made on understanding the connection between then dq-domain and the time-domain translation, in addition to refining the WTV method..

Chapter 5

Discussion, Concluding Remarks and Further Work

All the relevant contributions and results of this thesis have now been presented, and this chapter is dedicated to first discuss the results, and then reach a conclusion for this thesis. Lastly, a section on further work will be presented, as there are some open questions in this thesis left unanswered.

5.1 Discussion

Since the main part of this thesis roughly can be divided into modeling from Chapter 2 and adaptive control in Chapter 3 and Chapter 4, these two subjects will be discussed separately in this section.

5.1.1 Converter and Grid Modeling

The first natural aspect to discuss from Chapter 2 would be the converter and grid models. Since the grid models are much simpler than the converter models, this will be covered first. Since the SISO model was not used for anything, other than deriving the stability criterion, as this is much simpler to do in the SISO case, this will not be discussed further.

The grid model is fairly straight forward, as it just consists of some filter elements, a series impedance, and a voltage source. The only aspect that may need a discussion is the choice of only varying the grid inductance, and keeping the grid resistance constant. The main justification for this is already presented in Appendix B.4. To summarize, the three most important reasons is that:

- This seems to be the standard in the literature that even considers varying grid impedance in the first place.
- No application is specifically considered in this thesis, so there is no reference for how the resistance should be varied, and also no reference for how it should be varied in relation to the grid inductance.
- The grid inductance is the dominant factor regarding stability, and changing the grid resistance as well will make the results more unclear and less concise.

Of course, there are downsides of neglecting the influence of changing grid resistance as well, mostly because there is no reason to believe that the grid resistance stays constant under different grid conditions, but with the arguments above, it seemed reasonable to make the choice that was taken.

Since the converter model is more complicated, more comments need to be made here. The main reason for using such a complicated model as in Figure 2.15b, with the corresponding expression for the small-signal converter impedance expression $\mathbf{Z_{oi}}$, was the wish of studying the impact the PLL has on stability, and then there is simply no way around it. Of course, there are other ways to include the effect of the PLL, but the selected model worked very well, and could almost be used directly, only some minor modifications were needed. A nice aspect about this model is that the PLL impact is so clear from the bode plots, with the negative resistive behavior, and also the fact that this can be directly controlled by the PLL bandwidth is a very nice aspect of the model. Naturally, the biggest downside of the model is that it is difficult to work with such a large expression, which will be discussed later.

When both of the models were developed, they could be used directly to form the minor-loop gain transfer function matrix $\mathbf{L}$, which again can be used for stability analysis with the use of the GNC. However, only stability analysis was not the goal of this thesis, the main objective was to develop adaptive control methods, and as discussed in Section 2.3, it was chosen to work directly with $\mathbf{L_{cl}}$ instead of $\mathbf{L}$. The main reasoning and consequences of this choice were discussed there, and will not be repeated, but it should be noted that it is this choice that shapes the rest of the thesis. Out of the two most negative consequences of using $\mathbf{L_{cl}}$, which is the model fitting problem and numerical issues, only the numerical issue part was relevant for this thesis in the end anyway, because the laboratory implementation was not an option.

The numerical problems still stand, and as stated many times in this thesis, considerable work was done to try and minimize this problem, both by model reduction, simplification, and decoupling, but also more practical efforts in Matlab with various techniques and methods to make sure that the result for the poles and zeros in $\mathbf{L_{cl}}$ made sense, and were consistent over time. This is critical, as most of the rest of the thesis depends on how the poles of $\mathbf{L_{cl}}$ are placed in the complex plane.

When it comes to the theoretical efforts of model reduction and decoupling, this is motivated and discussed in Appendix D.4, and the results seemed reasonable. Naturally, simplifying a system always comes at the expense of maybe losing important dynamics, but when the alternatives in this thesis are considered, there are no other options. If the full version of the grid and converter models are used, it would be nearly impossible to develop adaptive control methods within the scope of this thesis. And since the main objective of this thesis is adaptive control based on chancing grid impedance, necessary measures to achieve this objective had to be taken.

Even though the model fitting problem did not become a problem in this thesis, it should still be considered a serious concern for future work. To summarize, if $\mathbf{L_{cl}}$ is used directly, the grid inductance needs to be fitted to an analytical transfer function, and if the model fitting does not create a transfer function of the same order as used in all the theoretical models and adaptive control methods, the pole-zero plots may look completely different. This will have effects for both of the adaptive control methods developed in this thesis, as they rely only on $\mathbf{L_{cl}}$, and this could not be a concern if $\mathbf{L}$ and the GNC was used instead. That being said, the pros of using $\mathbf{L_{cl}}$ for adaptive control outweighed the cons, because it is so much easier to work with than $\mathbf{L}$ for developing adaptive control, as the poles and zeros can be analyzed directly and there is no need to rely on graphical techniques such at the eigenvalue loci.

5.1.2 Adaptive Control Methods and Implementations

General Adaptive Control Discussion

Chapter 3 contains the main theoretical contribution of this thesis, as most of the material up to this point is based on previous work in the literature. The first natural discussion point is the control objective defined in this thesis as ”*stable operation of the converter for as high grid impedance value as possible, while at the same time ensuring good control performance under different grid conditions*”. If only stable operation for as high grid impedance as possible is the objective, this thesis showed that simple static methods could achieve this. But if grid codes are taken into account, the aggressive static controller from Section 4.3 would probably not meet the power quality requirements, based on the highly distorted current injected to the grid. It is the second part of the control objective that sets it apart from static control, and only adaptive control can solve this problem, as changing grid impedance will affect the operation of the converter. The choice of using $\mathbf{L_{cl}}$ has already been discussed, but some of the implications for control needs to be addressed.

The initial plan was to obtain some analytical expression that related all the variables of interest and use this for a continuous adaptive control method. This is discussed in Section 3.1, and the reasons for why this was not achieved. Of course, it would have been nice with an analytical method mapped out, as basically, this would solve the entire problem, but this was not achievable. However, this does not necessarily affect the control objective if numerical methods can achieve similar results. Furthermore, it was chosen early on that gain scheduling was the preferred adaptive control method, as this maybe is the simplest. Also, gain scheduling fits very well with the fact that no analytical relations were obtained, and system dynamics had to be uncovered by simulating the system over a large range of control parameters and grid impedance values. Furthermore, this is a thesis on power systems and power electronics, not control theory, so it was preferred to keep it as simple as possible. Additionally, it was selected to split the problem in two, where the first approach was to only adapt the PLL, and later have a multivariable method if time and other factors allowed, because there was no guarantee at the time that anything that worked would be developed anyway. Therefore, the next thing to discuss is the specific methods and their implementations and results, and it will start with the adaptive PLL.

Adaptive PLL Method Discussion

Since the methods used are very experimental, it would be unnatural to just present the finished method and then explain it. Therefore, a lot of time in the adaptive PLL section was used on explaining the underlying system dynamics, to serve as a motivation for why the specific choices were taken. Examples of this were the choice of only focusing on the qq-channel, uncovering the fact the model did not capture the lower PLL bandwidth and determine a natural starting point of the method. The choice of only using the qq-channels are already appropriately addressed, and will not be repeated, but the two other issues need a proper explanation and discussion.

The fact that the model did not capture the lower PLL bandwidth was the first real sign that there is something off with the modeling. It is a bit unclear what the reason is, as it could be related to any or all of the point below:

- The model itself, mainly inspired by [13].
- A result of the model reduction and decoupling.
- Misunderstanding about the PLL operation.
- Other problems related to the implementation/numerical issues.

It is a serious concern, and it should be addressed in future work, but in this thesis, a pragmatic approach was taken to solve this problem, as the user defines the lower limit manually, depending on the grid fundamental frequency in that area.

The second issue with this method was that the use of only focusing on the pole closest to the RHP, noting was done before the system was already very close to the stability limit. The reason for this is that for the selected base-case, the pole closest to the RHP was on the real axis, and did not move much for changing grid impedance or PLL parameters, only CC bandwidth. If then the CC bandwidth is selected too low, this pole will be located close to the RHP, meaning that the adaptive PLL method does not take any action before there is a lot of poles close to the RHP. The implications of this were clear in the simulations, where it was determined that simple static methods often performed better than the adaptive PLL, and what is then the point of having an adaptive method in the first place.

But if the method itself is focused on again, a lot of these issues can be resolved by having a better defined base-case. Also, the method is very intuitive and simple, if one pole moves closer to the RHP, simply adjust the PLL bandwidth so that the opposite effect happens. Furthermore, this method helped to gain insight into the underlying dynamics of the pole movement, and the flaws of the methods helped to derive the more general multivariable method because potential pitfalls were already discovered. And the result was not bad, it made sure the system was stable for as high grid impedance as possible, by adjusting the PLL bandwidth, which fulfilled parts of the control objective.

Multivariable Adaptive Control Method Discussion

For the multivariable method, the goal was to include CC parameter adaption, and this complicates the analysis. No longer only one channel could be considered, and how all the poles move in regards to CC bandwidth, PLL bandwidth, and grid inductance had to be uncovered. Therefore, also Section 3.3 starts out in the same fashion as Section 3.2, where lots of time in the beginning is spent on describing the underlying dynamics. The reason for this was once again to motivate the methods used later, as after all the WTV method is experimental in nature.

The main takeaway from the adaptive PLL, which only focused on the real value of the critical pole (RVCP), was that in some way, more information had to be considered. In the beginning, different methods were tried where, for example, a certain number of poles was selected, or weights of each pole were assigned manually, depending on how much they moved in all intervals. All the methods except the chosen one result in a numerical mess that did not result in ”optimal” parameter selection for the system under study in this thesis when it was played out. In the end, a very simple idea was chosen, where no care about how many poles were selected, only their placement in the complex plane, in relation to a predefined threshold value. As Chapter 4 showed, it worked well. After all, it is a very intuitive method, and by having the RVCP method running in parallel to make sure that the system does not go unstable until the absolute stability limit, that problem is also handled, and in many ways the method it fulfills the control objective.

When that being said, there are some weaknesses to the method. The repeating weakness is the risk of numerical errors already discussed, as this method relies heavily on where the poles are located and how they move with changing parameter values. This has previously been discussed, and measures were taken to manage it. Secondly, the method might seem a bit unmotivated as there probably exist techniques for similar problems that probably handles the issues in more efficient ways. However, this has already been discussed, and the main reason why an experimental approach was taken was that it was not very important how the gain schedule was derived, what was important was if the results of the method made sense, which they did.

Furthermore, it was defined in the scope that a formal theoretical foundation for the adaptive control method is outside the scope.

To go back to the technicalities of the methods, there are some questionable aspects in the method itself, such as the weighing of the poles. One might argue that the pole close to the RHP has to little weight compared to those who are close to the threshold. Also, there is no mechanism to handle complex conjugated pole pairs, which results in a complex pole pair counting twice as much as poles on the real axis, and the fact that the imaginary value of a pole is not taken into account at all.

Furthermore, there are some problems by representing the two controllers only by their bandwidth. For the PLL, this process seems to be quite smooth, and the same method as in [13] was used, and it was verified that the results make sense. But for the current controller, the reader might have noticed the strange way of determining the CC parameters and also the numerical value of the bandwidth itself. All this is covered in Appendix F, with the justification that how to find fitting control parameters are not interesting in the main part of the thesis, but for future work, it should be explored deeper how to effectively represent the current controller by one variable, and how this determines K_p and K_i. The main reason it was not focused on in this thesis, was that it would be very difficult to keep track of everything, and if analysis on how K_p and K_i for the PLL and CC would be handled directly, the result would probably be more unclear. It would also be a lot more computationally heavy as instead of simulating over two variables for a certain grid inductance to find a good combination of PLL and CC bandwidth, the simulation would need to iterate over four variables. For finding the global optimum of the WTV, this is not possible if a normal personal computer is used because it takes several days for one interval, but this depends on the accuracy of the intervals, of course. Also, having a function with four instead of two variables would make it impossible to analyze visually as a surface function. The global optimum can still be found by finding the maximum or minimum in a multidimensional array, but it takes away a lot of the intuition of the method. All of these issues plays into the fact that the time-domain simulation indicated that the multivariable method might select a bit too low CC bandwidth, and the main reason for this was that the poles close to the RHP are not weighted heavily enough.

The reader probably notices that also for the multivariable case, the predefined strategy defined by the flowchart in Figure 3.8 was slightly modified as the flowchart had a small logical error for very high grid impedance values. The error was basically that when the RVCP limit was reached, the focus should shift from maximizing the WTV function to minimizing RVCP, and then check if the limit was reached again. The problem with this was that in the next iteration, the limit for the RVCP is not reached, and the WTV is maximized, and then the limit is reached and so on. This should be handled more smoothly in future work than simply deviate from the predefined strategy. But all in all, it looked like the multivariable method solved most of the problems in the adaptive PLL method.

Time-domain Implementation Discussion

The final discussion point is the translation of the adaptive methods into the time-domain implementation in Simulink, in Section 4.3. The goal of this section was to see if it was possible to observe the same results as in Section 4.2 when the two adaptive methods were compared, and in addition, adding two static controllers. This part had some challenges, and the reasons for this need to be discussed.

First of all, if the numerical values developed in either of the two adaptive methods were used in the Simulink model, no stable operating point was found. This means that there is something wrong in one of the models, as it does not properly translate. Most likely, the reasons are quite simple, even though both models model the same system, there are differences in how they operate and the underlying dynamics. There is not necessarily an ”error” in any of the models, so it was not that surprising. Therefore, it was decided that the Simulink control system would be in per-unit, as own previous work had been done in per-unit, and then translate the output of the gain schedules into per-unit control variables. This process worked very well, with some minor adjustments, which are addressed in Appendix I.

In the end, it did not really matter that the translation was perfect either. The important part was if the observed trends from the adaptive methods could be translated to the time domain, in regards to how the CC and PLL bandwidths should move under changing grid conditions. And all in all, the trends were translatable which was very nice to see, except for some cases which are already addressed in Section 4.3.

However, future work needs to find the underlying reasons for the differences, so not only the same trends and conclusions can be drawn, but also numerical values are matching. This will facilitate more of a ”plug-and-play” characteristic, wherein an ideal scenario the multivariable method in this section is modified, and the result works directly in the time-domain, whether it be simulations or Hardware-in-the-loop implementations at the lab, and then finally in a system in the real world. Naturally, not only the adaptive methods have to be refined for this, but also the converter and grid models would have to include more details. Section 4.3 also showed how bad the first adaptive method was, which highlighted the fact that is is important to also care about the CC bandwidth, and not only the PLL, which is the impression one might get from the literature.

All in all, there was no combination of control parameters that had the same performance as the multivariable method over the full grid inductance range, which was very nice to see, but at the high grid inductance case in section 4.3.3, it looked like the multivariable control parameters were not optimal compared to the static high case. Some results like this is to be expected, as the translation to the time-domain is not perfect, and the WTV method itself is not perfect either.

5.2 Concluding Remarks

Since the previous two subsections addressed many different aspects of the work in this thesis, it may be difficult to identify the main findings and takeaways that need to be considered for further work. The list below summarizes this.

- The MIMO converter model used in this thesis clearly shows the impact of PLL bandwidth on system stability and related this to grid impedance.
- The use of the small-signal impedance-based transfer function matrices $\mathbf{L}$ and $\mathbf{L_{cl}}$ proved to be very useful methods to determine the stability of the converter-grid system, and implement adaptive control in this thesis. It seemed like decoupling the d and q axis was reasonable for the scope of this thesis.
- The first adaptive control method was effective in increasing the stability limit, but it was shown that only considering the most critical pole, and only considering the qq-channel of $\mathbf{L_{cl}}$ gave sub-optimal dynamic performance under certain grid conditions. In the time-domain implementation, the method proved to be worse than other simple static methods.
- The second adaptive control method was effective in increasing the stability limit, at the same time ensuring good dynamical performance under all grid conditions. To get this result, both the dd-channel and qq-channel of $\mathbf{L_{cl}}$ had to be considered, and both the current control parameters and PLL parameters had to be considered. No combination of control parameters that had better dynamic performance than the multivariable method over the full grid inductance range was found. In the time-domain implementation, the same trends could be observed, but in some cases it looked like other combinations of control parameters was better, which indicated that the method could be further improved, and more efforts should be made in bridging the dq-domain and time-domain models.

5.3 Further Work

Based on the discussion in Section 5.1, and the concluding remarks in the previous section, the list below serves as possible topics that should be included in further work.

- In future work, more details in the converter model should be incorporated. It should further be explored what the limitations of the model is, to uncover the weaknesses such that lower PLL limit is captured, and then make changes that address the problems.
- More efforts should be made to make sure that the transfer function matrices are numerically stable and that selection of control parameters for the base-case of a certain system makes sense in a time-domain model or laboratory setup so that the results are directly translatable.
- It should also be considered to include outer control loops such as power or voltage control, as this is common in real systems. The balance between accurate system representation and models that actually can be used for adaptive control has to be carefully balanced, as this thesis discovered that if $\mathbf{L_{cl}}$ is to be used for adaptive control, there must be no numerical errors.
- The decoupling of d and q axis seemed to be reasonable in this thesis, but this should be further explored when system decoupling is valid, and apply more formal reasoning behind this.
- More emphasis should be put on grid modeling, and how the equivalent grid resistance and inductance changes under different grid conditions, and in relation to each other. For this, a specific application should be considered. Efforts should be made to make sure that the grid estimation fits the grid impedance to an appropriate model, which makes sense for the version of $\mathbf{L_{cl}}$ that is used for adaptive control.
- The multivariable methods should be considered from the start, because this thesis highlights the importance of CC and PLL bandwidth both have for stability.
- Future adaptive control methods should also consider taking more formal attempts at proper model reduction, to get a manageable size of $\mathbf{L_{cl}}$ where an analytical relation between CC bandwidth, PLL bandwidth, and grid impedance can be obtained.
- More work should be done on how to represent the controllers by one variable, namely the bandwidth, and more care should be used on how K_p and K_i evolve with the bandwidth.
- Even though the use of $\mathbf{L_{cl}}$ might seem promising, there are certain problems discussed that will disappear if $\mathbf{L}$ and the GNC is used instead. It should be further studied how the GNC can be directly used for adaptive control, and not only for determining stability for a certain set of controllers and grid inductance cases.
- Implement the multivariable adaptive control flowchart in Figure 3.14 as an explicit optimization problem that calculates the whole gain schedule at once.

Bibliography

[1] X. Wang, Y. Li, F. Blaabjerg, P. Loh. ”Virtual-Impedance-Based Control for Voltage-Source and Current-Source Converters”, *IEEE Transactions on Power Electronics*. Vol. 30, no. 12, December 2015.

[2] B.K. Bose. ”Global Energy Scenario and Impact of Power Electronics in the 21st Century”, *IEEE Transactions on Industrial Electronics*, Vol. 60, no.7, pp.2638-2651, July 2013.

[3] H. Alenius, ”Modeling and Electrical Emulation of Grid Impedance for Stability Studies of Grid-Connected Converters”, Master of Science Thesis, Tampere University of Technology, October 2017.

[4] Y. Mohamed. ”Mitigation of Converter-Grid Resonance, Grid-Induced Distortion and Parametric Instabilities in Converter-Based Distributed Generation”, *IEEE Transactions on Power Electronics*, vol 26, no.3, March 2011.

[5] C. Buchhagen, C. Rauscher, A. Menze, J. Jung. ”First Experiences with harmonic interactions in converter dominated grids”. *International ETG congress 2015, Die Energiwende - blueprints for the new energy age.* Nov. 2015, pp1-7.

[6] G. Irwin, A. Jindal, A. Isaacs. ”Sub-synchronous control interactions between type 3 wind turbines and series compensated AC transmission systems” , *2013 4th IEEE International Symposium on Power Electronics for Distributed Generation Systems (PEDG)*, July 2011, pp.1-6 ISBN: 978-1-4577-1000-1.

[7] C. Li. ”Unstable Operation of Photovoltaic Inverter from Field Experiences”, *IEEE Transaction on Power Delivery* Vol. 8977, No. c, pp.1-1, 2017.

[8] T. Messo, R. Luhtala, T. Roinila, D. Yang, X. Wang and F. Blaabjerg, ”Real-time impedance-based stability assessment of grid converter interactions,” *2017 IEEE 18th Workshop on Control and Modeling for Power Electronics (COMPEL)*, Stanford, CA, 2017, pp. 1-8.

[9] J. Sun, ”Small-signal methods for ac distributed power systems - a review” *IEEE Transactions on Power Electronics*, vol. 24, no.11, pp.2545-2554, Nov. 2009.

[10] A. Rygg. “Impedance-based methods for small-signal analysis of power electronics dominated systems”. PhD thesis. Norwegian University of Science and Technology, 2018.

[11] S. Halsne. “Stability Assessment by Grid Impedance Method and Adaptive Control”. Master thesis. Norwegian University of Science and Technology, 2018.

[12] M. Cespedes, J. Sun, ”Adaptive Control of Grid-Connected Inverters Based on Online Grid Impedance Measurements”, *IEEE Transactions on Sustainable Energy*, Vol. 5, No. 2, April 2014.

[13] B. Wen, D. Boroyevitch, R. Burgis, P. Mattavello, Z. Shen. ”Analysis of d-q small signal impedance of grid-tied inverters”. In *IEEE transactions on power electronics*, Vol. 31, NO.1, January 2016.

[14] T. Midtsund, J. A. Suul, T. Undeland ”*Evaluation of Current Controller Performance and Stability for Voltage Source Converters Connected to a Weak Grid*”, *2010 2nd IEEE International Symposium on Power Electronics for Distributed Generation Systems*.

[15] X. Ruan, X.Wang, D.Pan, D. Yang, W. Li, C. Bao. *Control Techniques for LCL-Type Grid-Connected Inverters,CPSS Power Electronics Series*, 2018.

[16] F. Rønningen. ”Impedance-based Stability and Adaptive Control of Grid-Connected Inverter”. Specialization Project. Norwegian University of Sienc eand Technology. 2019.

[17] F. Blaabjerg, Z. Chen, S.B Kjaer. ”Power electronics as efficient interface in dispersed power generation systems”. *IEEE Transaction on Power Electronics*, Vol. 19, No. 5, pp. 1184–1194, Sep. 2004.

[18] J. Sun, ”Impedance-based stability criterion for grid-connected inverters,” *IEEE Transactions on Power Electronics*, vol. 26, no.11, pp.3075-3078, Nov. 2011.

[19] R.D. Middlebrook. ”Input filter considerations in design and application of switching regulators”, *IEEE Industry Applications Society Annual Meeting, 1976*

[20] M. Belkhayat. ”Stability criteria for AC power systems with regulated loads” PhD thesis, Purdue University, 1997.

[21] L. Harnefors, M. Bongiorno, and S. Lundberg, “Input-admittance calculation and shaping for controlled voltage-source converters,” *IEEE Transactions on Industrial Electronics*, vol. 54, no. 6, pp. 3323–3334, Dec. 2007

[22] M. Cespedes and S. Jian, “Impedance shaping of three-phase grid-parallel voltage-source converters,” *Proc. 27th Annu. Appl. Power Electronics Conference Expo*, Mar. 2012, pp. 754–760

[23] B.Wen, D. Boroyevich, R. Burgos, P. Mattavelli, and Z. Shen, “Influence of phase-locked loop on dq frame impedance of three-phase voltage source converters and the impact on system stability,” presented at the *CPES Power Electronics Conf.*, Blacksburg, VA, USA, Apr. 6–8, 2013

[24] T. Suntio, T. Messo, J. Pukko. ”Power Electronics Converters, Dynamics an Control in Conventional and Renewable Energy Applications”. Wiley-VCH, ISBN: 978-3-527-69851-6

[25] B. Wen, D. Boroyevic, R. Burgos, P. Matavelli, Z. Shen ”Inverse Nyquist Stability Criterion for Grid-Tied Inverters”, *IEEE Transactions on Power Electronics*, vol. 32, no. 2, Febraury 2017.

[26] B. Wen, ”Stability Analysis of Three-phase AC Power Systems Based on Measured D-Q Frame Impedances”. PhD thesis, Virginia Polytechnic Institute, November 2014.

[27] Y. Sun. ”The Impact of Voltage-Source-Converters Control on the Power System: the stability analysis of a power electronics dominant grid”, PhD thesis Eindhoven University of Technology, December 2018.

[28] A. Knop and F. W. Fuchs. ”High frequency grid impedance analysis by current injection”. *2009 35th Annual Conference of IEEE Industrial Electronics*, pp. 536–541, 2009.

[29] S. Cobreces, E. J. Bueno, D. Pizarro, F. J. Rodriguez, and F. Huerta. “Grid impedance monitoring system for distributed power generation electronic interfaces”, *IEEE Transactions on Instrumentation and Measurement*, vol. 58, no. 9, pp. 3112–3121, 2009.

[30] M. Ciobotaru, V. Agelidis, and R. Teodorescu. “Line impedance estimation using model based identification technique”, *Power Electronics and Applications (EPE 2011), Proceedings of the 2011-14th European Conference on. IEEE*, 2011, pp. 1–9.

[31] S. Halsne. *Specialization Project: Online Grid Impedance Estimation and Stability Assessment*. NTNU, Department of Electric Power Engineering 2018

[32] M. Céspedes and J. Sun. *“Online grid impedance identification for adaptive control of grid-connected inverters Energy Conversion Congress and Exposition (ECCE), 2012 IEEE*, pp. 914–921.

[33] T. Roinila, M. Vilkko, and J. Sun. ”Broadband methods for online grid impedance measurement” *Energy Conversion Congress and Exposition (ECCE)*, 2013 IEEE, pp. 3003–3010.

[34] J. A Suul, S D’arco, P. Rodriguez, M. Molinas ”Impedance-compensated grid synhronization for extending the stability range of weak grids with voltage source converters”,*IET Generation, Transmission Distribution, Special Issue: Selected Papers from the 11th IET International COnference on AC and DC Power Transmission (ACDC 2015)*

[35] G. A. Dumont, M. Huzmezan, *” Concept, Methods and Techniques in Adaptive Control”*, Proceedeing of the American Control COnference, Anchorage May 2002.

[36] P. A. Ioannou, J. Sun, ”Robust Adaptive Control”, Dover Pubications Inc, 2012

[37] K. J. Åstrom, B. Wittenmark, ”Adaptive Control”, Dover Publications Inc, 2008

[38] `https://se.mathworks.com/help/control/examples/using-the-right-model-representation.html`
07.04.2020

[39] `https://se.mathworks.com/help/slcontrol/ug/linearizing-nonlinear-models.html`
29.05.2020

[40] Johann W. Kolar. *Lecture Notes*, Power Electronic Systems I, Zurich Fall term 2018, ETH Zürich

[41] Johann W. Kolar. *Lecture Notes*, Power Electronic Systems II, Zurich Spring term 2019, ETH Zürich

[42] B. Wu, M. Narimani, ”High-Power converters and AC drives”, second edition, page 96 , 2017

[43] Q. Zhong, T. Hornik. *Control of Power Inverters in Renewable and Smart Grid Integration, 2013 John Wiley and Sons, Ltd* chapter 1.6 and 22

[44] A.E.W.H Kahlane, L. Hassaine, M. Kherchi. ”LCL filter design for photo photovoltaic grid connected systems”, Centre de Development des Energies Renouvelables, CDER, 2014

[45] R. Teodorescu, M. Liserre, P. Rodriguez. ”Grid Converters for Photovoltaic and Wind Power Systems”, 2011 John Wiley and Sons, Ltd Chapter 4, 8, 11

[46] Massachusetts Institute of Technology, ”Analysis and Design of Feedback Control Systems”, Lecture notes, course number 2.14

[47] M. Dahleh, M. A. Dahleh, G. Verghese, ”Lecture notes on Dynamic Systems and control”, Massachusetts Institute of Technology, course number 6.241J.

[48] S. Skogestad and I. Postlethwaite, ”Multivariable feedback control: design and analysis”, John Wiley Sons, 2005

[49] M. Korytowski. ”Effects of the phase locked loop on the stability of a voltage source converter in a weak grid environment” PhD thesis. University of Pittsburgh, 2014

[50] M. Dozein, P. Mancarella, T. Saha, R. Yan. ”System Strength and Weak Grids: Fundamentals, Challenges and Mitigation Strategies”, *2018 Australasian Universities Power Engineering Conference (AUPEC)*, Auckland, New Zealand, 2018, pp. 1-7. doi: 10.1109/AUPEC.2018.8757997

[51] T. Roinila, M. Vilkko and J. Sun, ”Broadband methods for online grid impedance measurement,” *2013 IEEE Energy Conversion Congress and Exposition*, Denver, CO, 2013, pp. 3003-3010.

[52] F. Rønningen, ”Effect of Increased Switching Frequency for LCL-Filter Design and PI Parameter Selection for Current Controlled Grid-Connected Voltage Source Converter”, Student Paper in the course *ELK-23 Power Electronics for Future Power Systems*. NTNU 2019.

[53] J.G. Balchen, T. Andresen, B.A. Foss, ”Reguleringsteknikk”, 6th edition, Institutt for teknsisk kybernetikk, NTNU, 2016

[54] M. Amin *Lecture Notes ELK21, Autumn semester 2019, NTNU Trondheim*

[55] R. Nilsen, ”Compendium TET4120 Electric Drives”, NTNU 2018.

[56] C.K. Kim, V.k Sood, G.S. Jang, S.J Lim, S.J Lee HVDC Transmission: Power Conversion Applications in Power Systems, John Wiley and Sons 2009.

[57] B. Wen, R. Burgos, D. Boroyevich, P. Mattavelli, Z. Shen, ”AC Stability Analysis and dq frame Impedance Specifications in Power-Electronics-Based Distributed Power Systems”, IEEE Journal of Emerging and Selected Topics in Power Electronics, Vol.5, No. 4, December 2017

[58] IEEE Standard, *IEEE Guide for Planning DC Links Terminating at AC Locations Having Low Short-Circuit Capacities*. IEEE Press, 1997.

[59] V. Kaura, V. Blasko ”Operation of a phase-locked Loop system under Distorted Utility Conditions”, *IEEE Transactions on Industry Applications*, Vol. 33, NO. 1, January 1997

[60] Y. Tang, L. Huang, and G. Zhao, “Resonant feed forward control for LCL-type grid-tied inverters in weak grid condition” *2016 IEEE Energy Conversion Congress and Exposition (ECCE)*, 2016, pp. 1–6.

[61] Q. Zhao, H. Zhang, W. Song, X. Li, and Q. Yang, “Regulator reconstruction strategy of grid-connected inverter in weak grid”. *2016 IEEE 8th International Power Electronics and Motion Control Conference (IPEMC-ECCE Asia)*, 2016, pp. 451–457.

[62] X. Chen, J. Chen, C. Gong, and H. Wang, “Impedance-based analysis of grid-connected inverter in high impedance grids”, *2013 IEEE 8th Conference on Industrial Electronics and Applications (ICIEA)*, 2013, pp. 1284–1289

[63] J. J. Sun, W. Hu, H. Zhou, Y. M. Jiang, and X. M. Zha, “A resonant characteristics analysis and suppression strategy for multiple parallel grid-connected inverters with LCL filter” *Journal of power electronics* vol. 16, pp. 1483–1493, 2016.

[64] S.K. Chung, A phase tracking System for Three Phase Utility Interface Inverters, *IEEE transactions on Power Electronics*, Vol. 15, No. 3 May 2000.

[65] S. Zhou, X. Zou, D. Zhu, L. Tong, Y. Zhao, Y. Kang, X. Yuan, ”An Improved Design of Current Controller for LCL-Type Grid-Connected Converter to Reduce Negative Effect of PLL in Weak Grid”, *IEEE journal of emerging and selected topics in power electronics*, Vol. 6, No.2, June 2018

[66] I. Vieto and J. Sun, ”On system modeling and analysis using d1-frame impedance models”, *2017 IEEE 18th Workshop on Control and Modeling for Power Electronics (COMPEL)* , pages 1-8, July 2017

Appendix

Appendix A

Mathematical Transformations, $\alpha\beta$ and dq-Frame

Both the converter and grid modeling in this thesis is done in the dq-frame, and in the main part of the thesis, there is no proper explanation where this comes from. The abc-dq-transformation is just applied directly, with no questions asked. Therefore, this appendix will introduce this coordinate transformation, which is essential in this thesis. However, also the $\alpha\beta$-transformation is included here, as also the $\alpha\beta$-frame gives useful information about a general three-phase system, even though it is not used in this thesis. The $abc-\alpha\beta$-transformation can also serve as a smaller step in the complete $abc - dq$-transformation, and it also helps motivating why the dq-frame is useful. Therefore, this appendix first has a section on the $\alpha\beta$-frame, followed by a section on the dq-frame. The whole chapter is based on own previous work in [16].

A.1 Clarke Transformation and Space Vector Modulation, $\alpha\beta$ frame

Space Vector Modulation (SVM) is a widely used modulation technique and gives an intuitive picture of how the six transistors in the VSC can be operated to generate the wanted signal [40]. This technique establishes a relationship between the switching states and a 2-dimensional space vector.

The switching state of each leg can be represented by 1 or 0 as described in Appendix B.1. As there are three bridge legs, each with two possible switching states, this gives $2^3 = 8$ possible combination. If the three-phase balanced operation of the inverter is assumed, the relationship in (A.1) is obtained.

$$v_{A0}(t) + v_{B0}(t) + v_{C0}(t) = 0 \tag{A.1}$$

The voltages $v_{A0}(t)$, $v_{B0}(t)$, $v_{C0}(t)$ are the phase voltages at time t. The relationship shown in (A.1) is important because it is possible to describe the three-phase system with only two quantities, as (A.1) leaves one degree of freedom. Furthermore the Clarke transformation is introduced in (A.2).

$$\begin{bmatrix} v_\alpha(t) \\ v_\beta(t) \end{bmatrix} = \frac{2}{3} \begin{bmatrix} 1 & -\frac{1}{2} & -\frac{1}{2} \\ 0 & \frac{\sqrt{3}}{2} & -\frac{\sqrt{3}}{2} \end{bmatrix} \begin{bmatrix} v_{A0}(t) \\ v_{B0}(t) \\ v_{C0}(t) \end{bmatrix} \tag{A.2}$$

This is also referred to as the abc-$\alpha\beta$ transformation, as two new voltage quantities $v_\alpha(t)$ and $v_\beta(t)$ are obtained. The constant $\frac{2}{3}$ is not entirely random chosen as this value will give the same amplitude value of the voltages before and after the transformation [40]. The space vector itself has $v_\alpha(t)$ and $v_\beta(t)$ as real and imaginary parts, expressed as:

$$\vec{V_{\alpha\beta}}(t) = v_\alpha(t) + jv_\beta(t) \tag{A.3}$$

The eight possible combinations of switching states form six active and two inactive space vectors shown in Table A.1. By defining the phase voltages that appears for the different switching states, and inserting them into (A.2) six active space vectors in the complex plane are obtained.

Space Vector	Switching state	On-state switches	Vector Definition
$\vec{V_0}$	111	S_1, S_3, S_5	$\vec{V_0} = 0$
$\vec{V_0}$	000	S_2, S_4, S_6	$\vec{V_0} = 0$
$\vec{V_1}$	100	S_1, S_2, S_6	$\vec{V_1} = \frac{2}{3}V_d e^{j0}$
$\vec{V_2}$	110	S_1, S_2, S_3	$\vec{V_2} = \frac{2}{3}V_d e^{j\frac{\pi}{3}}$
$\vec{V_3}$	010	S_2, S_3, S_4	$\vec{V_3} = \frac{2}{3}V_d e^{j\frac{2\pi}{3}}$
$\vec{V_4}$	011	S_3, S_4, S_5	$\vec{V_4} = \frac{2}{3}V_d e^{j\frac{3\pi}{3}}$
$\vec{V_5}$	001	S_4, S_5, S_6	$\vec{V_5} = \frac{2}{3}V_d e^{j\frac{4\pi}{3}}$
$\vec{V_6}$	101	S_1, S_5, S_6	$\vec{V_6} = \frac{2}{3}V_d e^{j\frac{5\pi}{3}}$

Table A.1: Space vector definitions

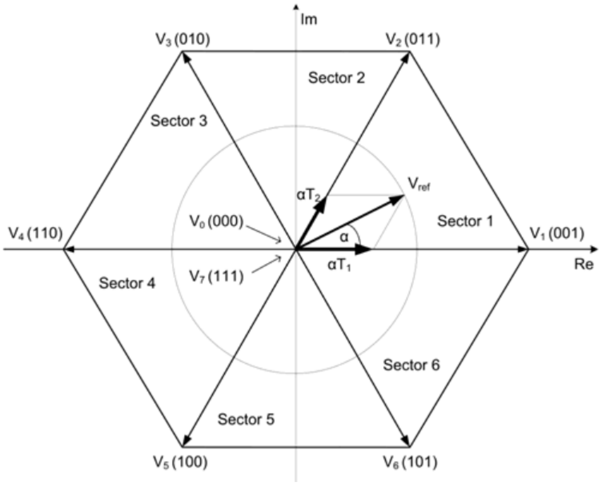

Figure A.1: Space Vector Modulation diagram [41]

Here appears the whole point of the SVM technique. Figure A.1 has as reference vector, V_{ref}, representing the three modulation waves. This is only a snapshot in time, and the reference vector rotates in the complex plane at angular velocity $2\pi f_m$. In this example, the reference vector is in sector 1, between $\vec{V_1}$ and $\vec{V_2}$. The reference vector can be composed by adding $\vec{V_1}$, $\vec{V_2}$, and $\vec{V_0}$ multiplied by the dwell time stayed in each switching state. As there are two ways of representing $\vec{V_0}$ this leaves one degree of freedom. The dwell time can be calculated by simple vector algebra, and calculations will be omitted here.

By following two simple rules, a switching sequence that will follow the reference vector can be determined. The first rule is to only use the two most nearby space vectors plus the zero vector. The second rule is to only switch one bridge leg at the time. Following these two rules, lower switching losses and lower current transients will occur [42]. So for the example reference vector in Figure A.1 a possible switching sequence can be as described in A.4

$$000 - 100 - 110 - 111 - 110 - 110 - 000 \tag{A.4}$$

It can be seen that only one leg is switched at the time and that the only $\vec{V_1}$, $\vec{V_2}$ and $\vec{V_0}$ are used, i.e. the adjacent space vectors.

A.2 Park Transformation, dq frame

As the $\alpha\beta$ transformation was introduced in the last section, to change the reference frame from abc to $\alpha\beta$, another transformation that gives a rotating reference frame will be presented in this section. This is called the direct-quadrature reference frame, or dq-frame for short [43]. The motivation for this is that v_α and v_β still are functions of time. If the reference frame synchronously rotates at the same speed as the space vector, the reference vector is no longer a function of time i.e. two time-invariant DC quantities describe the three-phase system in steady-state. The $\alpha\beta$ to dq transformation is presented in (A.5).

$$\begin{bmatrix} v_d \\ v_q \end{bmatrix} = \begin{bmatrix} cos(\theta) & sin(\theta) \\ -sin(\theta) & cos(\theta) \end{bmatrix} \begin{bmatrix} v_\alpha(t) \\ v_\beta(t) \end{bmatrix} \tag{A.5}$$

This is effectively the same as multiplying $\vec{V_{\alpha\beta}}(t)$ by $e^{j\theta}$. θ is the angle of the space vector and is also time dependent. The new vector is now:

$$\vec{V_{dq}} = v_d + jv_q \tag{A.6}$$

The dq transformation could be performed directly on an abc system, not going via the $\alpha\beta$ transformation as done in (A.5). By substituting the expression in (A.2) into (A.5), the expression for the transformation from abc coordinate system to dq directly, as seen in (B.10), is obtained.

$$\begin{bmatrix} v_d \\ v_q \end{bmatrix} = \frac{2}{3} \begin{bmatrix} cos(\theta) & cos(\theta - \frac{2\pi}{3}) & cos(\theta + \frac{2\pi}{3}) \\ -sin(\theta) & -sin(\theta - \frac{2\pi}{3}) & -sin(\theta + \frac{2\pi}{3}) \end{bmatrix} \begin{bmatrix} v_a(t) \\ v_b(t) \\ v_c(t) \end{bmatrix} \tag{A.7}$$

when the multiplication constant for the $abc - dq$-transformation is $\frac{2}{3}$, as in (B.10), it is the *power invariant* transform. If the constant is $\sqrt{\frac{2}{3}}$ it is the *voltage invariant* transformation. In the end, it does not really matter which one of them is used, as long as it is consistent, and clearly stated which one of them that is used. In this thesis the power invariant version is used.

Appendix B

Grid-Connected 2L-VSC

As this thesis mostly is concerned with modeling, control, and stability of the converter connected to the grid, little emphasis is put on the converter itself. The main reason for this is that most of it are considered background knowledge, and when the relevant point comes up, it is just referred to as this appendix, to make sure that the main part of the thesis is as compact as possible and that a red line is followed. However, it is useful to consider the background information as well. Therefore the first section in this appendix covers the converter topology, the basics of Sinusoidal Pulse Width Modulation (SPWM). The second section covers everything related to grid connection, i.e. the grid synchronization mechanism, the LCL-filter, and the basics of resonance damping methods.

This thesis also jumps directly over the conventional converter modeling and control and dives straight into the impedance-based stability analysis. Therefore, the third section of this appendix covers conventional current control in the dq-frame, the methods used here are very useful for getting initial control parameters, also in the MIMO converter modeling from the main part of this thesis.

The last section in this appendix covers the topics of weak grid characterization, typical grid impedance values, and motivates why a weak grid in this thesis first and foremost are characterized by increased grid inductance. Most of this appendix is based on own previous work in [16].

B.1 Converter Topology and Sinusoidal PWM

The converter under study in this thesis is shown in Figure B.1. This is known as the three-phase 2L-VSC. The DC-side is represented by a voltage source V_d, with positive and negative terminals P and N. The DC-side also contains a capacitor C_d to provide a stable DC voltage source and remove high-frequency variations. The DC-side voltage is assumed to be stable and constant for this whole project, if not specified otherwise. The positive and negative terminals of the DC-source are connected by three bridge legs. Each bridge leg has two transistors in series, with a terminal in between, giving a total of six transistors. The three terminals A, B and C are called the inverter terminals, and are the interface to the three-phase system, and represent the three phases. The three phases can be connected to the grid, preferably with a grid filter, or to a load, as shown in Figure B.1. The six transistors, numbered from 1 to 6, have a diode connected in antiparallel. The diodes are called freewheeling or flyback diodes, with the purpose to provide an alternative path for the current to flow when the transistors are turned off. This is especially important if the loads are inductive, for example,

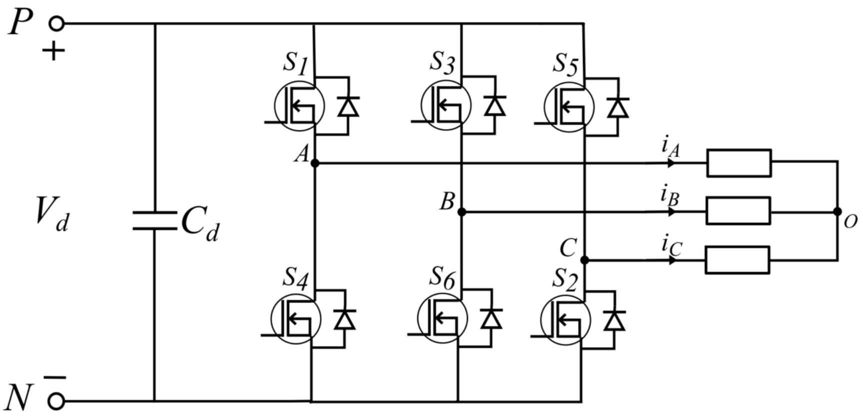

Figure B.1: Schematic of 2L-VSC.

an induction motor. The transistors depicted in Figure B.1 are Insulated-Gate Bipolar Transistors (IGBT), but details on transistors are not given any attention in this thesis, and the behavior is considered ideal if not specified otherwise.

To explain the principle of operation, only one phase needs to be considered, as the three phases are identical. Consider phase A, where the transistors S_1 and S_4 are connected in series. First of all, note that if S_1 and S_4 both are in the ON state at the same time, the DC-side will be short-circuited. Therefore it is assumed that the gate drivers and control system are not able to switch the upper and lower switch ON at the same time. This is a fair assumption as this is true for most gate drivers for VSC applications [40]. Therefore, for simplicity, the state when the upper switch is ON can be called 1 and the state where the lower switch is ON can be called 0. In-state 1 the inverter terminal is directly connected to the positive terminal P and have the full DC-side voltage V_d as the output on the AC side. In-state 0, the opposite happens, and the inverter terminal is connected to the negative terminal, N, with output voltage zero. This is the reason for the name two-level, the AC side can only output two levels of voltage, in this case, either V_d or 0.

If the voltages at the inverter terminals are denoted v_{AN}, v_{BN} and v_{CN} the following equations describe the voltages appearing over each phase in the star-connected load:

$$v_A = v_{AN} - v_{0N} \tag{B.1}$$

$$v_B = v_{BN} - v_{0N} \tag{B.2}$$

$$v_C = v_{CN} - v_{0N} \tag{B.3}$$

The voltage v_{0N} is the voltage from the star-point of the load referred to the negative rail of the DC source, which in balanced three-phase operation is zero. The voltage difference between the loads' neutral point and the inverter terminal voltages results in phase currents i_A, i_B, and i_C.

The principle of operation for the 2L-VSC can best be illustrated in Figure B.2.

v_{mA}, v_{mB}, v_{mC} are sinusoidal modulating waves and v_{cr} is the carrier wave. They have corresponding frequencies f_m and f_{cr}. The modulating waves have the shape and frequency of the wanted sine wave at the inverter terminals. If the carrier wave and modulation waves have the same frequency, it is known as fundamental frequency modulation, but usually, f_{cr} is operated at a much higher frequency than f_m [40].

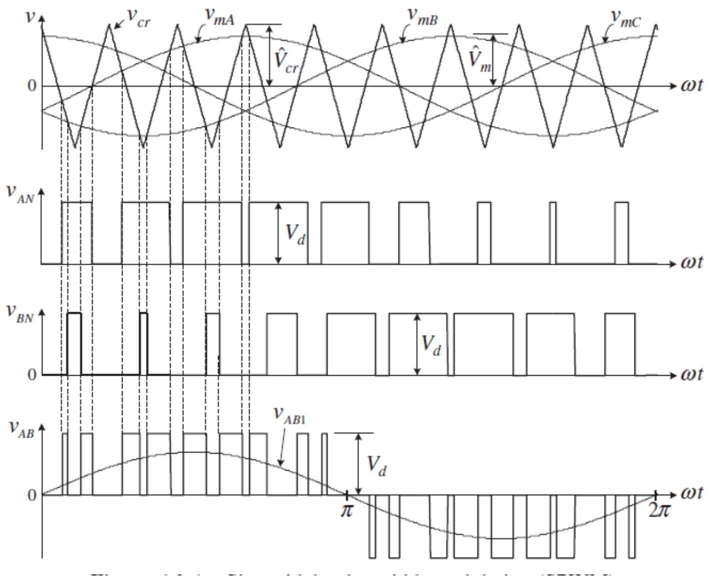

Figure B.2: Sinusoidal Pulse Width Modulation [42].

The Sinusoidal Pulse Width Modulation (SPWM) switching rule is:

$$v_m < v_{cr}, \textit{upper transistor OFF i.e. switching state 0} \tag{B.4}$$

$$v_m > v_{cr}, \textit{upper transistor ON i.e. switching state 1} \tag{B.5}$$

This can be observed in Figure B.2, where square-shaped voltages appear at the inverter terminals. In regions where the higher amplitude is needed, pulses of larger a width are generated, and opposite in low amplitude areas. If the pulses are averaged over a small time interval, the shape resembles that of a sine curve. By having a high frequency of the carrier wave, f_{cr}, compared to the modulation wave frequency, f_m, this approximation becomes better and better.

Figure B.2 also shows one of the line voltages, v_{AB}, which can be described by:

$$v_{AB} = v_{AN} - v_{BN} \tag{B.6}$$

It should be noted that in recent years the trend is that SVM described in Appendix A.1 and another mode advanced modulation techniques are being increasingly popular over the SPWM, but regardless the SPWM is an intuitive introduction to inverter control. No more details on modulation techniques will be covered in this appendix, or this thesis, as this is of little concern with regards to the scope of this thesis.

B.2 Grid Synchronization, PLL, LCL-filter and Resonance Damping

When the 2L-VSC from Section B.1 is to be operated in grid-connected mode, several challenges arise. How is the converter connected and synchronized to the grid in the first place, and how does the converter stay synchronized? These are important questions that will be answered in this section. In both scenarios, real-time information about the grid is needed, because parameters such as voltage magnitude, phase, and frequency never are in steady-state in a real grid.

There are two main categories of methods for synchronization, open-loop methods, and closed-loop methods [43]. No open-loop methods will be discussed in this thesis, as these methods often have poor performance related to frequency deviations, voltage distortions, and voltage imbalances in the grid [43]. The closed-loop methods have mechanisms that make sure the information obtained from the grid is accurate [43].

The convectional Phase-Locked Loop (PLL) will not be covered, as the Synchronous Reference Frame PLL (SRF-PLL) will be used for this project. PLLs are adopted as part of the control in most grid-connected converts today [43]. Furthermore, it is common for grid-connected converters to have a grid filter, and in this section, a brief comparison of different solutions will be covered before the LCL-filter will be selected for this project. The LCL-filter can lead to resonance problems, therefore resonance damping methods should be considered, and this is discussed at the end of the section.

The Synchronous Rotating Frame PLL (SRF-PLL) is now considered, which is commonly used in three-phase systems [43]. Figure B.3 shows the operational block diagram of the SRF-PLL.

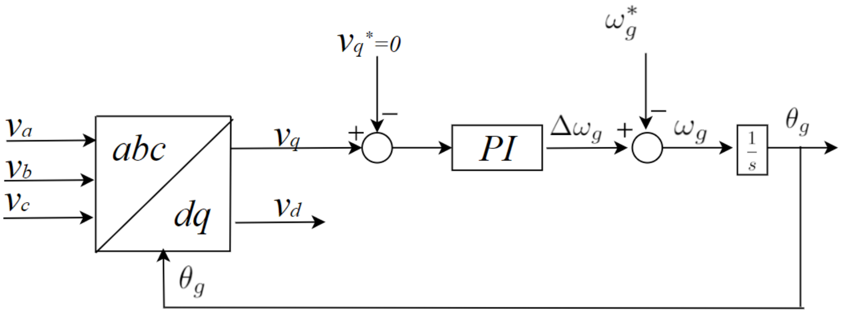

Figure B.3: Block diagram of an SRF-PLL.

The input to the SRF-PLL is the three-phase voltages, and the first operation is the abc to dq transformation described in Appendix A.2. The output is then two DC signals, v_d and v_q. v_q is compared to the reference v_q^*, which is set to zero. If v_q is zero, the controller reference and the grid rotates at the same speed and the same angle, that is the reason for $v_q^* = 0$. The error is fed through a PI-controller, to get the deviation in grid angular frequency, $\Delta\omega_g$, which is compared to the grid angular frequency reference, ω_g^*. The result, ω_g, is integrated to obtain θ_g, which is fed back to close the loop. In steady-state, this will result in $v_q = 0$, so that the frequency and phase of the input and output are locked.

There are other more sophisticated methods for obtaining phase and frequency information, such as the Second-Order Generalized Integrator Phase-Locked Loop (SOGI-PLL), Sinusoidal Tracking Algorithms, and Sinusoidal Locked Loops [43], but they will not be covered as PLLs are not the focus of this project. [43] is a source for more detailed information about this topic.

In the grid-connected VSC, a filter is needed to attenuate the harmonics generated by the PWM operation of the converter [15]. The filter is placed between the converter and the grid, and a first attempt can be a simple inductor, the L-filter.

For two main reasons, the L-filter will not be looked any further into. First, if the L-filter alone is to attenuate the harmonics in the current enough to meet standards and grid codes, the value of the inductance would need to very high, especially for high power applications due to lower switching frequency. To realize one bulky inductor is expensive. Secondly, the high value of the inductance can lead to a slow dynamic response [45]. Even for lower power applications, like DG-PV systems, where the switching frequency can be increased, and therefore the inductance can be decreased, a pure L-filter would require a significant inductance and therefore be expensive and bulky. Moreover, last but not least, the L-filter does not filter out high-frequency switching harmonics.

A second approach would be the LC-filter, consisting of an inductor in series and a capacitor in parallel with the VSC. This is a second-order filter and has better damping capabilities than the L-filter [44]. However, connecting such a filter to the grid, the resonance frequency of the filter becomes dependent on the grid impedance, and therefore this filter will not be considered either. Also, it does not solve the problem with one bulky inductor value.

Instead, consider the topology presented in Figure B.4. The VSC is connected to the grid with an LCL-filter consisting of two inductors, L_1 and L_2, and one capacitor, C. The grid is represented as a voltage source v_g.

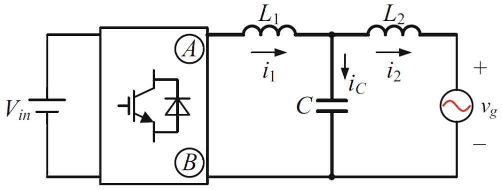

Figure B.4: LCL-filter [15].

The LCL-filter has the capacitor branch between the two inductors, which can bypass high-frequency harmonics. This means the value of the inductor can be reduced, but still attenuate the current harmonics enough to meet standards. The filter provides an attenuation of 60 dB/decade for frequencies above resonance frequency, which can be calculated to be as shown in (B.7).

$$f_{res,LCL} = \frac{1}{2\pi}\sqrt{\frac{L_1 + L_2}{L_1 L_2 C}} \tag{B.7}$$

However, also this filter topology can lead to resonance problems like the LC-filter. Therefore designing the LCL-filter is a crucial aspect of the grid connection of the VSC. However, filter design is not the main task of this project. But based on [45], [15], and [44] a summary on how to design the LCL-filter is as follows:

1. *Ripple analysis and converter side inductor choice*. By specifying the maximum allowed current ripple, chose the L_1 inductor.

2. *Harmonic attenuation and choice of the resonance frequency*. After choosing L_1, the choice of attenuation level will indicate which resonance frequency the filter must have, and consequently, the product L_2C can be derived from the transfer function of the filter [45].

3. *LCL-filter optimization*. Optimize the relation between L_2 and C to obtain the value from the last step. Factors such as installed reactive power of the filter and robustness of the resonance frequency to grid impedance variations can be used as the optimization criterion.

At the resonance frequency, and close to it, the LCL-filter could easily lead to system instability, and therefore damping methods should be considered. In this section some passive and active damping methods will briefly be described and compared, however, it will be kept brief as one method will be used in this thesis.

Passive methods are called passive because they consist of inserting passive components into the filter network. That would be a combination of resistors, capacitors, and inductors to attenuate the resonance of the filter. The most basic passive methods are based on inserting a resistor into the filter network. For the LCL-filter there are six possible ways of doing this, as a series or parallel resistor can be placed for the three filter components, L_1, L_2 and C. This will lead to six different frequency responses, discussed in [15]. Based on their discussion, using a resistor in series with the capacitor gives lower losses than the other alternatives, and has been widely used.

However, adding a resistive element will always increase losses and several improved solutions have been proposed to reduce the power losses further. The improved passive damping methods consist of adding additional passive elements to the filter topology. The basic idea is to make the current running through the resistor smaller, to get lower resistive losses. It can be shown that a lower power loss and high harmonic attenuation can be achieved, but the downside is increased volume and cost. Further details and differences of the solutions can be found in for example [15].

B.3 Conventional dq-frame Current Control for the Grid-Connected VSC

Several times in this thesis the term current control is referred to without any proper explanation as this is considered background material. However, a short description will follow in this appendix, to serve as a foundation to some of the unexplained transfer function from the converter modeling sections, for both the SISO and MIMO case in 2.2 and 2.3. Also, an explanation for the choice of PCC for the specific converter-grid connection used in this thesis will follow. This Appendix is based on own previous work in [52] and [16] .

The system to be examined in this thesis is a current-controlled 2-level three-phase grid-connected VSC, The topology has been illustrated several times in this thesis, but is repeated in B.5 for clarity. The DC side supply voltage, V_{dc}, is assumed stable, and no DC side voltage control is considered. The converter is connected to the grid with an LCL-filter, which consists of the inverter side filter inductor L_{f1}, the grid side filter inductor L_{f2}, and the filter capacitor C_f. The phase currents flowing in the first filter inductor can be defined as i_{L1a}, i_{L1b} and i_{L1c} and the injected grid current flowing through the second filter inductor L_{f2} can be defined as i_{L2a}, i_{L2b} and i_{L2c}.

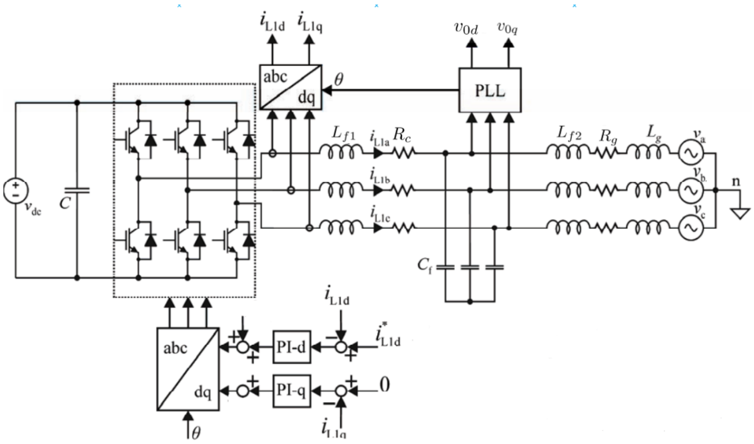

Figure B.5: System and control topology

The control method selected in this thesis is current control, however, with an LCL-filter this is not clearly defined, as there are several possible approaches. The first choice is whether to control the injected grid currents i_{L2a}, i_{L2b} and i_{L2c} or the inverter currents i_{L1a}, i_{L1b} and i_{L1c}.There are examples of both in the literature, [15] is an example of the first, and [8] is an example of the latter. In this thesis, the latter is chosen. An advantage of this is that the Point of Common Coupling (PCC) can be defined as close to the inverter as possible, namely right after the first filter inductors. The PCC is also where the Phase Locked Loop (PLL) measures the voltage and estimates the grid frequency and angle, which is needed to perform the dq-transformation. The PLL is considered in other parts of this thesis, and will not be repeated here.

The control design choices are visualized in Figure B.5 where current and voltage sensors are applied. The PLL calculates the estimated grid angle θ which is used as an input for the abc to dq transformation of the inverter phase currents. The output is the calculated currents in the dq reference plane, i_{L1d} and i_{L1q}. The most basic version of PI-current control is shown if Figure B.5, where no additional feedback loops are applied. The current references are compared to the actual currents, the error is fed into a PI controller, and the reverse dq transformation is applied to generate the PWM gating signals for the six switches. The theory for modeling the converter in the dq plane will briefly presented, however as this is standard theory it will not be covered in depth. A source for the topic is for example [15]. The first simplification to be done is to neglect the filter capacitance, and model the filter as the sum of L_{f1} and L_{f2}, which can be denoted as L_{eq}. This is done to get a plant model that can be used in a first approach. By applying KVL on the circuit in Figure B.5 the expression in equation B.8 below is obtained.

$$L_{eq}\frac{di_{Leq}}{dt} + R_c i_{L_{eq}} = v_c - v_g \tag{B.8}$$

here v_c is the inverter terminal voltage, and v_g is the grid voltage. This can be applied to all three phases, which is shown in equation B.9 below.

$$L_{eq}\begin{bmatrix}\frac{di_{L1a}}{dt}\\ \frac{di_{L1b}}{dt}\\ \frac{di_{L1c}}{dt}\end{bmatrix} + R_c\begin{bmatrix}i_{Leqa}\\ i_{Leqb}\\ i_{Leqc}\end{bmatrix} = \begin{bmatrix}v_{ca}\\ v_{cb}\\ v_{cc}\end{bmatrix} + \begin{bmatrix}v_{ga}\\ v_{gb}\\ v_{gc}\end{bmatrix} \tag{B.9}$$

This representation of the system has its weaknesses, mainly because the quantities are sinusoidal in the time-domain. By applying the dq transformation to the system, the three-phase system can be represented by two DC quantities. To go from the abc reference frame to the dq reference frame, the system in equation B.9 is multiplied by the transformation matrix T shown below on both sides.

$$T = \frac{2}{3}\begin{bmatrix}cos(\theta) & cos(\theta - \frac{2\pi}{3}) & cos(\theta + \frac{2\pi}{3})\\ -sin(\theta) & -sin(\theta - \frac{2\pi}{3}) & -sin(\theta + \frac{2\pi}{3})\end{bmatrix} \tag{B.10}$$

The grid phase angle θ is obtained from the PLL. No information is lost in the dq-transformation as a fundamental assumption for the system is balanced three phase operation, meaning that the sum of the three phase voltages is zero, leaving one degree of freedom. This will transform the system to the dq reference frame and the system is now defined as in equation B.11 and B.12.

$$L_{eq}\frac{di_d}{dt} + R_c i_d - \omega L_{eq} = v_{cd} - v_{gd} \tag{B.11}$$

$$L_{eq}\frac{di_q}{dt} + R_c i_q + \omega L_{eq} = v_{cq} - v_{gq} \tag{B.12}$$

A new quantity appears in the new equations, which is ω . As described earlier, an SRF-PLL is used to estimate the grid frequency, ω, and grid angle, θ, These quantities are needed to perform the dq transformation in the first place, and will also be necessary for the control system introduced later. However, the terms ωL_{eq} introduced in equations B.11 and B.12 above gives a coupling between the phases. This can be handled by introducing decoupling terms in the control structure, and the dependency can be removed.

This marks a natural transition from system description without control, to introducing control. As a first starting point for control, the currents will be controlled by PI-controllers. The PI-controller will bring the steady-state error to zero, which is derived and explained more in detail in [53]. Therefore two PI-controllers are introduced, one for d-current and one for q-current. The cross-coupling is also introduced in the control system, and a relation can be defined from the inverter terminal voltage references as:

$$v_{cd}^{*} = v_{gd} + L_{eq}\frac{di_d}{dt} + R_1 i_d - \omega L_{eq} \tag{B.13}$$

$$v_{cq}^{*} = v_{gq} + L_{eq}\frac{di_q}{dt} + Ri_q + \omega L_{eq} \tag{B.14}$$

The full control scheme can be summarized in Figure B.6 below. The next question to answer is how to tune the PI parameters K_p and K_i, which will be discussed in the next section.

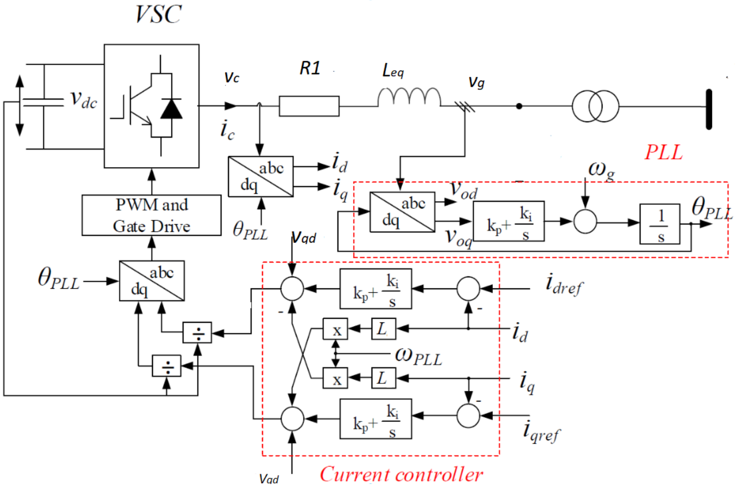

Figure B.6: Full control system when the LCL-filter is simplified to a L-filter [54]

To derive a method for determining initial control parameters for the PI-current controllers, the open-loop transfer function from i_{dref} to i_d in Figure B.6 must be considered. i_{dref} is called i_d^* from now for simplicity. A generalized block diagram consisting of three parts is considered below in Figure B.7. For brevity the method is not derived here, as it is a fairly standard method, that is explained in for example [55].

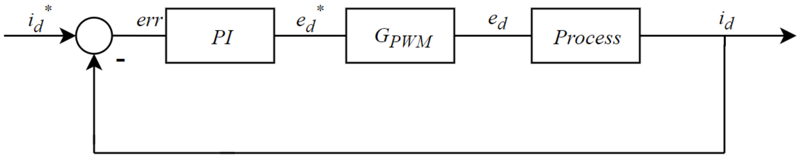

Figure B.7: Generalized simplified block diagram of transfer function from i_d^* to i_d

B.4 Weak Grid Characterization and Typical Grid Impedance Values

Several times in this thesis the term ”weak grid” is used without a proper definition or explanation. It is also assumed that the grid is mainly inductive, without any explanation. Therefore this appendix will cover the topic of weak grid characterization, and why a weak grid often is related to PEC dominated grids and higher grid impedance. The sources for this Appendix is [15], [49] and[50].

Also, since the theoretical grid model used for both the modeling part and the adaptive control has grid inductance and resistance as input parameters, typical values for this has to be established so actually realistic values for the weak and strong grid can be used in the adaptive control systems. Therefore this is considered in the last paragraph of this section.

The motivation for describing the characterization of a weak grid for the context of this thesis is that the grid is behaving differently in a PEC dominated grid compared to the traditional grid. One aspect is the difference in inertia because many renewable energy sources do not have any rotating mass. This will, in turn, affect the Short Circuit Ratio (SCR) of the system, which again is related to the impedance of the system, which is central in this thesis. This relation will be described below.

When a fault happens is a system with a high amount of Synchronous Generators (SG), the SG is still able to maintain the terminal voltage by control of the rotor excitation current. From basic theory, it is known that the short circuit current of SG is proportional to the terminal voltage of the SG. Therefore the reduction of the SCR level increases the risk of voltage instability and voltage collapse. This is not the case for most renewable energy sources, as they often are coupled to the grid electronically with converters, as in this thesis. Therefore, PEC dominated grids provide no substantial contribution to the SCR [50], and low SCR increases, therefore the voltage sensitivity following a fault. Therefore it can be stated that a part of the system that has low SCR can be considered a weak area of the grid. This is also the definition of a weak grid in IEEE standard 1204-1997 [58], where it is stated that a weak grid is characterized as ”an AC system with low SCR and/or inadequate mechanical inertia”. The short circuit ratio is defined as:

$$SCR_{PCC} = \frac{S_{PCC}}{P_s} \tag{B.15}$$

where S_{PCC} is the short circuit ratio at the PCC, i.e. where the converter is connected to the grid, and P_s is the power output of the source. This ratio is a common way to describe grids' strength or stiffness.

In [15], [56] and [49] the SCR is further related to grid impedance values, where it is shown that low SCR, which is present in power electronics dominated grids, is related to high values of grid impedance. In the same manner, high SCR is related to low grid impedance value and strong grid conditions. This directly connects the fact that in a PEC dominated grid higher grid impedance values will occur. PEC dominated grids does not only often have high grid impedance, but the range of impedance values is also much bigger and varies faster than in a traditional SG dominated grid [50].

This is one of the main investigation points in this thesis, to verify that a high grid impedance value affects the operation of the converter, and use grid impedance estimation as in input to the control system to account for the negative effect this gives, for example by the regulation of PLL bandwidth by adaptive control methods.

Another dimension to characterize weak and strong grids is how the grid reacts to disturbances. In a strong grid, the disturbance caused by load changes or harmonics has a small effect on the grid, compared to a weak grid where there will be large voltage variations under the same disturbances. This will not be looked into, as it is not within the weak grid description this thesis is focused around, namely the impedance level.

Last but not least, an important topic for this thesis is the level of grid inductance and grid resistance and how this affects the operation. As defined in the scope, and several other places in this thesis, the grid is modeled as a voltage source with series resistance and inductance. Therefore it is of great interest to find typical values, but also look into what effect the inductance and resistance have on stability issues.

The first problem by finding typical values is that it greatly depends on the application. For example, if the converter is situated at the end of a long radial line the X/R ratio is low, but if the converter is operated in a strongly meshed grid, for example in a big city, the X/R ratio is high. As this thesis has no specified application defined in the scope, this cannot be used to determine typical base-case values. However, this does not matter when considering the second argument, what impact do the two parameters have on the stability assessment. It is well established in the literature, for example in [8] and [12], that it is the *resonance* between the converter and the grid that is causing stability problems, not the grid impedance itself. Naturally, it is the inductive behavior of the grid that is causing the resonance, not the resistive behavior. Therefore, this thesis considers the grid to be mainly inductive, and the grid resistance is kept constant to a value of 0.5 Ω, similar to measured grid resistance values from similar laboratory setups reported in the literature.

When it comes to the numerical value of the grid inductance, results from the literature reports that the converter operation is unstable for values in the range of 1-10 mH for similar laboratory setups. For example in [13], [11] and [12] the converter-grid systems all becomes unstable in this range. Also, own previous work in [16] showed that the stability limits were highly nonlinear and that if a good base-case of control parameters the system dynamics were very similar for low grid inductance values and very low grid inductance values. With this in mind the inductance increments in Chapter 3 are selected as they are.

This choice of only changing the grid inductance to emulate changing grid conditions, compared to tuning both grid resistance and inductance, gives focus to the handling the resonance problem, and at the same time simplifies the analysis, as only one parameter has to be updated and the problem with X/R ratio is handled directly. This simplification of mainly focusing on the inductive part of the grid, and also connecting the terms weak grid and high inductance, is also common in the literature, for example in [60], [61], [62], [63], [18] [27].

Appendix C

Fundamentals of Small-Signal Analysis and Impedance-Based Stability in dq-domain

In this Appendix, a more general introduction to the topic of impedance-based stability analysis will be presented. The small-signal modeling part is based on [10] and [41] and the impedance-based stability analysis theory is based on [18].

First, the general method of small-signal analysis will be presented, and then, as the main topic of this thesis is impedance-based stability analysis of the 2L-VSC with grid connection, it is natural to consider the underlying basic theory of impedance-based stability analysis.

The last section of this appendix presents some common building blocks transfer functions used in this thesis, and how the dq-domain impedance representation looks like. This serves as a fundamental background for how more complex systems look like and behave in 2.3.1 and is therefore important to understand the system behavior.

C.1 Small-Signal Analysis and Stability

Small-signal analysis is a common technique especially used in control theory and electrical engineering, with the purpose of investigating how the system responds to a small disturbance around a specific operating point [10]. In comparison to simple circuits consisting of only passive and linear elements, resistors, inductors, and capacitors, which often is easily be solved directly with the use of linear differential equations, power electronics circuit often use non-linear circuit elements such as transistors, diodes and integrated circuits, which cannot be solved by linear differential equations directly. Attempts to solve such circuits directly can either lead to very complicated models that often give very little understanding of the underlying dynamics of the system, or just an unsolvable mathematical mess. Therefore, one solution is to only look at small changes close to some given operating point, and linearize all equations around this point. This is exemplified by the illustration in Figure C.1.

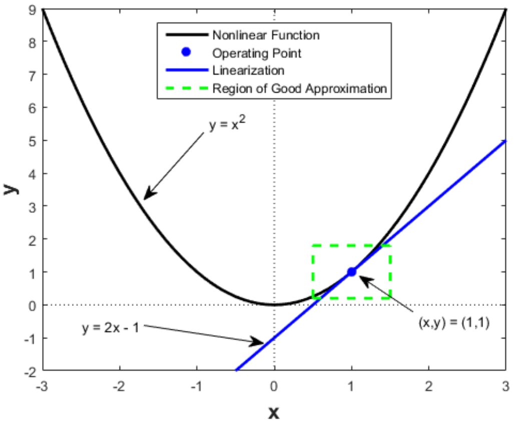

Figure C.1: Illustration of the small-signal concept on a general system [39]

To specify this concept for this thesis, it is useful to define what small-signal impedance means, as this is a fundamental concept. To guide the discussion, a simple system is considered in Figure C.2a, and in C.2b the same system has been subject small-signal sinusoidal perturbation, i.e. a voltage source $v_{inj} sin(\omega_{inj} t)$ added in series with the DC voltage source. Obviously, the amplitude v_{inj} must be much smaller than V_{dc} for the small-signal approximation to hold. The total source voltage $v(t)$ is now equal to $v(t) = V_{dc}+v_{inj} sin(\omega_{inj} t)$ In the first case, the subsystem is black-boxed, and nothing is known about the system, except the steady-state dc current $i = I_{dc}$, but in the second case, the current will change to $i(t) = I_{dc} + i_{inj} sin(\omega_{inj} t + \phi)$. From this, the small-signal impedance of the system can be defined directly from ohms law by considering the small-signal elements of $v(t)$ and $i(t)$ in (C.1).

$$Z(j\omega_{inj}) = \frac{v_{inj}}{i_{inj}} e^{j\phi} \tag{C.1}$$

The impedance is defined directly in the frequency domain as a function of the injection (or perturbation) frequency. Now the illustration in C.2b becomes clear, where the small-signal impedance Z is directly defined.

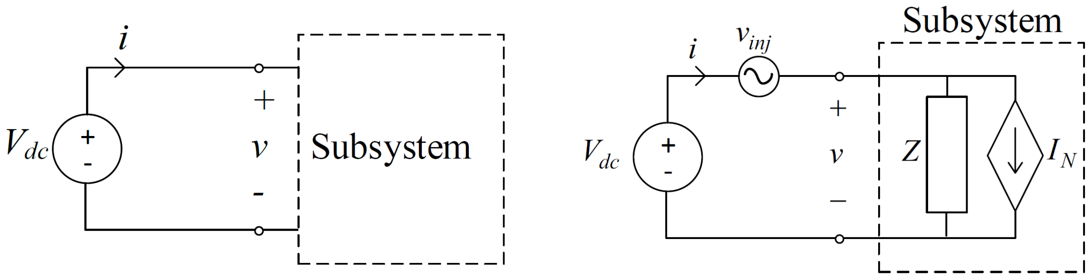

(a) General source and subsystem equivalent [10].

(b) General source and subsystem equivalent [10].

Figure C.2: Two general sources and subsystems.

Certain challenges arise when modeling small-signal impedance for three-phase ac systems compared to DC systems, but this is covered in Section 2.1 in this thesis, so that will not be repeated here. Instead, the next paragraphs will cover how to apply the impedance-based modeling for stability analysis.

The impedance-based stability criterion was first presented in [19], where a system was partitioned into a source and load subsystem, like shown in Figure C.3.

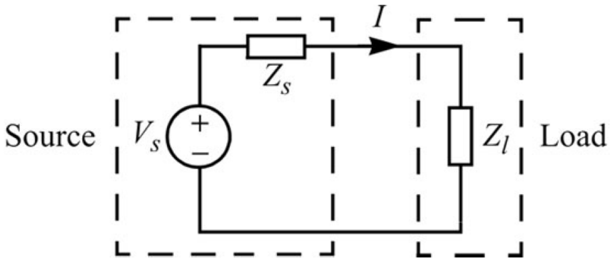

Figure C.3: Small-signal representation of voltage source with load [18].

As most power electronics circuits are non-linear, the linear representation in Figure C.3 is only valid for small-signal analysis, close to some operation point. By applying Ohms law, the expression in (C.2) can be obtained for the current I.

$$I(s) = \frac{V_s(s)}{Z_l(s) + Z_s(s)} = \frac{V_s(s)}{Z_l(s)} \frac{1}{1 + \frac{Z_s(s)}{Z_l(s)}} \tag{C.2}$$

It is further assumed that the voltage source is stable when unloaded. This is a fair assumption , and holds in most cases [18]. This implies that the terms $V_s(s)$ and $\frac{1}{Z_l(s)}$ are stable on their own, and stability only depends on the expression in (C.3). From now on s is dropped as an argument, to simplify notation, as all functions are functions of s.

$$H = \frac{1}{1 + \frac{Z_s}{Z_l}} \tag{C.3}$$

From Appendix D it is evident that H resembles a standard closed-loop transfer function with negative feedback. Since the pole placement of H is the determining factor for stability, it can be concluded that H is stable if and only if the impedance ratio $\frac{Z_s}{Z_l}$ satisfies the Nyquist Stability Criterion for SISO systems. In other words, the system is stable if the denominator in H have no net rotation around the point (-1,0) in the complex plane.

At the moment, this criterion only holds for voltage source systems, but in [18] it is extended to current source systems.

C.2 Examples of Bode Plots in dq-domain

As mentioned in the introduction to this appendix, there is a need for understanding the dq-domain bode plots of basic building blocks, before bigger systems can be analyzed. Building blocks means, for example, resistive or inductive behavior in this context. Therefore, this section includes bode plots in the dq-domain of resistors, inductors, capacitors, inverter power stage, and current controller. Some of them might seem trivial, but it is still useful for trying to understand bigger, more complicated systems.

For clarity the transfer function matrices in the dq-domain for these transfer functions matrices from Section 2.3.1 are listed below.

$$\mathbf{Z_{dq,Resistor}} = \begin{bmatrix} R & 0 \\ 0 & R \end{bmatrix} \tag{C.4}$$

$$\mathbf{Z_{dq,Inductor}} = \begin{bmatrix} sL & -\omega L \\ \omega L & sL \end{bmatrix} \tag{C.5}$$

$$\mathbf{Z_{dq,Capacitor}} = \begin{bmatrix} sC & -\omega C \\ \omega C & sC \end{bmatrix}^{-1} \tag{C.6}$$

$$\mathbf{Z_{dq,powerstage}} = \begin{bmatrix} R_c + sL_c & -\omega L \\ \omega L & R_c + sL_c \end{bmatrix} \tag{C.7}$$

$$\mathbf{G_{dq,pi}} = \begin{bmatrix} K_p + \frac{K_i}{s} & 0 \\ 0 & K_p + \frac{K_i}{s} \end{bmatrix} \tag{C.8}$$

The Bode plots for these five expressions can be plotted directly in for example Matlab, and some of them will be presented in this section. For pure resistive behavior, the bode plot is not included, as this is just a constant gain with zero phase. A negative resistor, which is of special interest in this thesis will have magnitude equal to a normal resistor, but the phase will be constant -180 °. In Figure C.4 the dq-domain of an inductor and a capacitor is shown.

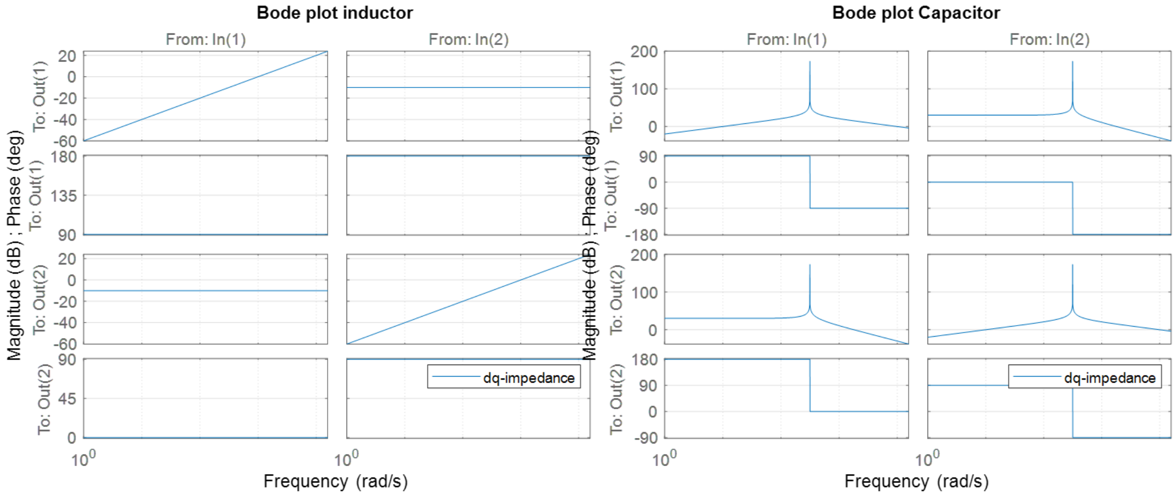

(a) Inductor dq-domain impedance bode plot.

(b) Capacitor dq-domain impedance bode.

Figure C.4: Inductor and capacitor dq-domain impedance bode plots.

For the inductor plot, the dd and qq magnitude plots increase with the frequency, as expected and the dq and qd have the same magnitude, but different phase due to the in the dq-channel. Due to the inversion in the expression for capacitor dq impedance, the bode plot is different from the simple resistor and inductor plots, but the plot nevertheless shown the basic behavior for a capacitor, short-circuit for high frequencies, open-circuit for low frequencies.

Now that the three basic building blocks are out of the way, the last two things to be considered here is the power stage and the current controller open-loop behavior. The power stage is shown in C.5a, which clearly shows a combination of resistive and inductive behavior in the dd and qqchannels, where the resistive parts dominates at low frequencies and inductive part at high, and in the dq and qd channels the behavior is just equal to the inductor, also as expected. Finally, the open-loop and closed-loop current controller is considered in C.5b, where the open-loop integrator function at low frequencies, and attenuation at high frequencies clearly are shown.

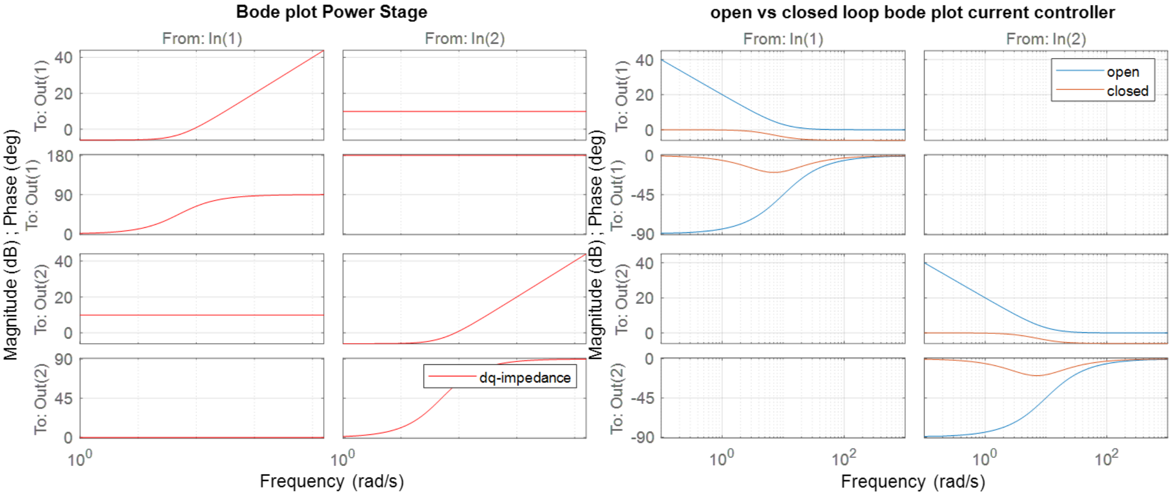

(a) Power stage dq-domain impedance bode plot.

(b) PI Current controller dq-domain impedance bode plots.

Figure C.5: Power stage and current controller dq-domain impedance bode plot.

Especially the dd-channel of both the power stage and the controller should be noted for the MIMO modelling part in Section 2.3.1 because the converter magnitude is shaped to a high degree based on these two building blocks.

Appendix D

Nyquist Stability Criterion and Additional MIMO Control Theory Fundamentals

In this thesis, the converter and grid are both modeled as MIMO systems, without much consideration for the fundamental underlying theory. Also, in Section 2.2 and 2.3, two different versions of the Nyquist Stability Criterion (NSC) are used directly without any proper explanation of the underlying concept. Therefore the first and second sections of this appendix cover the background theory of SISO NSC and MIMO NSC, respectively.

The third section of this appendix covers basic theory on MIMO systems, and how they differ from SISO systems, mostly in regards to poles and zeros, since this is of special interest for stability analysis in this thesis. This is further built upon in the fourth and final section of this appendix which first motivates why it is useful to have a decoupled MIMO system, where finally a justification for why this is done in this thesis is presented.

D.1 SISO Nyquist Stability Criterion

The Nyquist stability criterion is a graphical technique used to determine the stability of a dynamical system [53]. The criterion can be used if the system can be described by a closed-loop negative feedback transfer function representation. The general system under consideration is shown in Figure D.1, where the system open-loop transfer function is $h(s)$, written as h here for simplicity. The system has closed-loop negative feedback from the output y to the input x. The closed-loop transfer function, denoted H, of the system then becomes as in (D.1).

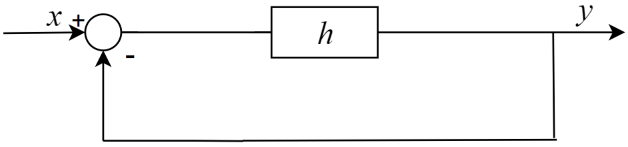

Figure D.1: General form of a closed-loop negative feedback system.

$$H = \frac{h}{1+h} \tag{D.1}$$

Here h is assumed to be a linear and rational function so that both numerator and denominator consist of polynomials. If this is true, then the same holds for H. The roots of these polynomials are commonly called zeros and poles, respectively, and are generally complex. Therefore the poles and zeros can be plotted in the complex plane, shown in Figure D.2, where the poles are marked with an x. From control theory [53], it is known that the poles of the transfer functions for a dynamical system determine stability, more precisely the real part of the pole. Both complex pole pairs and real poles in the Right Half Plane (RHP) corresponds to an increasing component in the time-domain response. Figure D.2 shows exactly this, as the response increases with time.

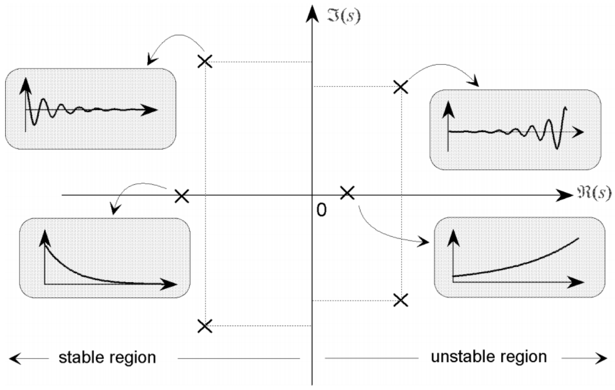

Figure D.2: Time-domain response for four different pole locations in the complex plane [46].

As already mentioned, the poles of the closed-loop transfer function, H, are determined by the zeros of the denominator, $(1 + h)$. Also, $(1 + h)$ will be a rational function if the original assumption holds, and will itself have poles and zeros that can be plotted in the complex plane. In a Nyquist diagram, the open-loop transfer function, h, is plotted in the complex plane with the frequency s as a variable. s is varied from zero to infinity, then minus infinity and back to zero. This will define a vector with its origin at (-1,0), and the value $(1 + h)$ is defined. This corresponds to the denominator of the closed-loop transfer function.

The Nyquist stability criterion then states that the number of RHP poles for the closed-loop system, H, equals the number of the RHP for the open-loop system, h, minus the number of net revolutions in positive rotational direction made by the vector $(1 + h)$. This is formulated mathematically in (D.2)

$$N_h = N_H - \frac{\Delta\angle(1+h)}{2\pi} \tag{D.2}$$

where N_h is the number of RHP poles for h the open-loop transfer function, N_H is the number of RHP poles for H the closed-loop transfer function, and $\Delta\angle(1 + h)$ is the net angular displacement by $(1 + h)$, which must be divided by 2π to get the net revolutions.

Another more intuitive but informal definition may be stated as: ”for a closed-loop system to be stable, the encirclement, if any, of the point (-1, 0) by the Nyquist plot of the open-loop transfer (as s moves along the Nyquist path) must be anti-clockwise, and the number of such encirclements must be equal to the number of poles of the open-loop transfer function that lie on the RHP" [49].

This implies that N_h in (D.2) must be equal to zero or negative for the closed-loop system, H, to be stable. This criterion is a simple but powerful tool to determine stability for a variety of systems.

D.2 MIMO Nyquist Stability criterion

This section of the appendix is based on [10] and [48].

The Nyquist Stability Criterion from the last section was applied to a SISO system, but it can also be extended to cover MIMO systems, which results in the Generalized Nyquist Criterion (GNC). This extension was first applied to power electronics in [20]. To guide the discussion, consider general block diagram in Figure D.3.

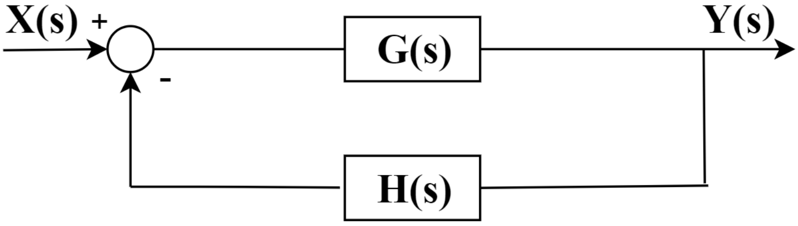

Figure D.3: General MIMO system for derivation of the GNC.

The expression in (D.3) relates the input vector $\mathbf{X}$ to the output vector $\mathbf{Y}$, with the closed-loop transfer matrix $\mathbf{M(s)}$. The argument s is dropped to ease notation, for all transfer matrices from now on.

$$\mathbf{M} = (\mathbf{I} + \mathbf{GH})^{-1}\mathbf{G} \tag{D.3}$$

Compared to SISO systems where stability is determined by the poles of the closed-loop transfer function, stability is determined by the poles of $det(\mathbf{M})$ for MIMO systems. Furthermore, define the so-called return-ratio matrix **L=GH**. **L** is also called the minor-loop gain. The determinant of the expression in (D.3) can then be defined as

$$det(\mathbf{I} + \mathbf{L}) = \frac{N}{S} \tag{D.4}$$

where it is assumed that the minor loop gain $\mathbf{L}$ has *P* number of RHP poles. The eigenvalue loci of $\mathbf{L}$ can also be defined:

$$det(\mathbf{I} + \mathbf{L}) = \prod_i (1 + \lambda_i(s)) \tag{D.5}$$

where $\lambda_i(s)$ is the i-th eigenvalue of L. From then the GNC it follows directly:

"if we assume that the minor loop gain has P *RHP poles, then the closed-loop system is stable if the number of counter-clockwise encirclements of (-1,0) in the complex plane made by the combined loci of all* $\lambda_i(s)$ *is P.*

more informally this can be rephrased as

"if the minor loop gain $\mathbf{L}$ *has no RHP poles, then the closed-loop system is stable if the combined loci*

of all $\lambda_i(s)$ do not encircle (-1,0) in the complex plane"

One of the advantages of the GNC is the simplicity of the graphical stability conclusion. But similar to the SISO case, the closed-loop can be looked at directly to determine stability. If the general system in Figure D.3 still is considered, the poles and zeros of the closed-loop transfer function matrix $\mathbf{M(s)}$ in (D.3) can be directly calculated. The stability is the same as the SISO case:

"The closed-loop transfer function matrix $\mathbf{M(s)}$ is stable if, and only if, all the poles are located in the Left Half Plane (LHP)"

Depending on the application it varies if the GNC or the poles of $\mathbf{M(s)}$ is most useful to use, but as discussed in the main part of this thesis, looking directly at the poles of $\mathbf{M(s)}$ is much more useful for adaptive control, at least this thesis.

D.3 MIMO Poles and Zeros, Multiplicity and Minimal Realization

One would think that the rather straight forward definition of poles and zeros in SISO systems extends directly to MIMO systems, but that is not the case. In this thesis, this has to be considered, because both the converter and grid are modeled as MIMO systems, and without taking proper care in the analysis, the approach of for example analyzing the dd or qq channel separate the other channels may be flawed.

Also, this part of the appendix serves as a fundamental background for the minimal realization, and model reduction considered in this thesis. Therefore, the material in this appendix has to be included in this thesis, and the theory is based on [47] and [48]. In this entire section, 2x2 transfer function matrices are used, but the analysis extends for all other dimensions as well, and this is only done to exemplify. All SISO transfer function is in this appendix in lowercase form, and MIMO transfer function matrices are in uppercase and/or bold to separate the two.

As as short reminder of poles and zeros in a SISO system, as well as to compare it to MIMO systems, consider the general transfer function on factorized form below.

$$h(s) = \frac{n(s)}{d(s)} = K\frac{(s-z_1)(s-z_2)....(s-z_m)}{(s-p_1)(s-p_2)....(s-p_n)} \tag{D.6}$$

$n(s)$ and $d(s)$ are the numerator and denominator polynomials of $h(s)$, and the poles and zeros are defined directly from this:

- system zeros are solutions to n(s)=0, and are denoted z_1 to z_m where m is the order of the numerator polynomial.
- system poles are solutions to d(s)=0 and are denoted p_1 to z_n where n is the order of the numerator polynomial.

Another way to define poles and zeros, without looking directly at the factorized form of $h(s)$ is to look at values for s when $h(s)$ goes to zero or is unbounded, respectively, formally defined as

$$\lim_{s\to z_i} h(s) = 0 \tag{D.7}$$

$$\lim_{s\to p_i} h(s) = \infty \tag{D.8}$$

In this case, when $s = z_i$, s is a zero for $h(s)$, and when $s = p_i$, s is a pole for $h(s)$. Naturally these two definitions are two ways of expressing the same principle.

This gets a bit more complicated when dealing with MIMO systems. To guide the discussion, consider the general 2x2 transfer function matrix $\mathbf{H}(\mathbf{s})$ in D.9.

$$\mathbf{H}(\mathbf{s}) = \begin{bmatrix} h_{11}(s) & h_{12}(s) \\ h_{21}(s) & h_{22}(s) \end{bmatrix} = \begin{bmatrix} \frac{n_{11}(s)}{d_{11}(s)} & \frac{n_{12}(s)}{d_{12}(s)} \\ \frac{n_{21}(s)}{d_{21}(s)} & \frac{n_{22}(s)}{d_{22}(s)} \end{bmatrix} \tag{D.9}$$

The definition of a MIMO pole is covered first, as this is very similar in MIMO and SISO systems.

- **Definition MIMO pole**: $\mathbf{H}(\mathbf{s})$ has a pole at a frequency p_0 is *some* entry of $\mathbf{H}(\mathbf{s})$ has a pole at $s = p_0$ [47]

So MIMO-poles are essentially the same as SISO poles. But this simple definition gives no information about the multiplicity of each pole, therefore a more complete MIMO pole definition is found in [48]. However, to avoid getting get to technical, a pragmatic approach is taken in this thesis for determining pole multiplicity. It can be shown [47] that if $\mathbf{H}(\mathbf{s})$ is written on its state-space form as in equation (D.10),

$$\mathbf{H}(\mathbf{s}) = \mathbf{C}(s\mathbf{I} - \mathbf{A})^{-1}\mathbf{B} + \mathbf{D} \tag{D.10}$$

The poles of $\mathbf{H}(\mathbf{s})$ are precisely equal in both location and multiplicity to the reachable and observable eigenvalues of the matrix $\mathbf{A}$. The reason for not diving deeper than this is that conversion between transfer function representation and state-space representation can easily be done in for example Matlab, and also it can be certain that the system is a minimal realization by internal Matlab commands and verification. On the topic of minimal realization, $\mathbf{H}(\mathbf{s})$ is defined to be a minimal realization if matrix $\mathbf{A}$ has the smallest possible dimension, i.e. the system has the fewest number of states. This implies that if a minimal realization of $\mathbf{H}(\mathbf{s})$ is obtained, the poles and zeros of $\mathbf{H}(\mathbf{s})$ is the minimal, and sufficient, to represent the full dynamics of the system. Therefore the discussion on MIMO poles end here, as both poles and their multiplicity easily can be found, at least to the extend needed in this thesis. In addition, Matlab ensures that it is always the minimal realization of the system that is used, which brings consistency to the analysis.

For MIMO zeros, it is not sufficient to state that zeros in any entries in $\mathbf{H}(\mathbf{s})$ translates to a zero for $\mathbf{H}(\mathbf{s})$. A zero should not be defined where all entries of $\mathbf{H}(\mathbf{s})$ have a zero either [47]. Instead consider the definition below:

- **Definition MIMO zero**: $\mathbf{H}(\mathbf{s})$ has a zero at a frequency z_0 of $\mathbf{H}(\mathbf{s})$ *drops rank* at $s = z_0$

As it is generally not wanted to go to deep intro not relevant background theory, as this is a thesis on power electronics and not control theory or mathematics, it is still necessary to make this definition. This definition corresponds to what is called a $transmission\ zero$ in the literature. If the system is a minimal realization, the transmission zeros is equal to the *invariant zeros*. As a reminder $rank(A)$ of a matrix A is the dimension of the vector space spanned by is columns, and if A is quadratic, A has full rank if $rank(A)$=m where m is the amount of rows/columns. In this thesis matrices that are not quadratic are of no interest. A more refined MIMO zero definition is as follows:

- **Definition MIMO zero (refined)**: A rational transfer function matrix $\mathbf{H}(\mathbf{s})$ of full rank has a zero at $s = z_1$ if there is a rational vector $\mathbf{u}(\mathbf{s_1})$ such that $\mathbf{u}(\mathbf{s_1})$ is finite and nonzero, and $\lim_{s \to s_1}[\mathbf{H}(\mathbf{s})\mathbf{u}(\mathbf{s})] = 0$.

It should be noted that with the definitions of MIMO zeros and poles $\mathbf{H}(\mathbf{s})$ can have poles and zeros at the same frequency, which differs from the SISO case where they just cancel each other. In general, this also means that if $\mathbf{H}(\mathbf{s})$ is invertible, the zeros of $\mathbf{H}(\mathbf{s})$ does equals the poles of $\mathbf{H}^{-\mathbf{1}}(\mathbf{s})$. This is related to the *direction* of the pole or zero, which is another concept not present in SISO systems. In general it can be said that the MIMO system can have a pole and zero for the same frequency for a minimal realization as long as the direction is different. To illustrate these results consider the simple transfer function matrix $\mathbf{G}(\mathbf{s})$ in (D.11).

$$G(s) = \begin{bmatrix} 1 & \frac{1}{s-3} \\ 0 & 1 \end{bmatrix} \tag{D.11}$$

It is clear from the definition of MIMO poles there is a pole at $s = 3$, but the reader can easily verify that for the input vector $\mathbf{u}(\mathbf{s}) = [-1, s-3]^T$, $\mathbf{H}(\mathbf{s})\mathbf{u}(\mathbf{s})$ approaches zero when s approaches 3. Therefore, by definition, there is also a zero at the frequency $s = 3$. This is summed up in Figure D.4 which shows that looking at the four entries individually is an invalid approach. It also shows that Matlab is able to handle the correct definition of transmission zeros, which is nice because Matlab is the main simulation software used in this thesis.

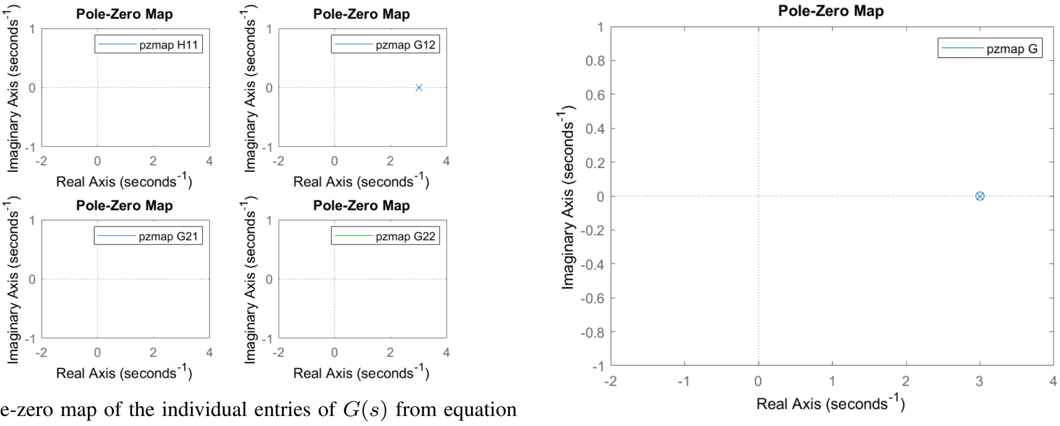

(a) pole-zero map of the individual entries of $G(s)$ from equation (D.11).

(b) pole-zero map of of G(s) from equation (D.11).

Figure D.4: Illustration of difference between poles and zeros in MIMO entries and MIMO full.

MIMO transmission zeros can also be directly solved from the minimal realization state-space representation of the system as in [48], where also the multiplicity then directly is defined. This can also be done directly in Matlab and therefore the details are not covered here. In general this thesis do not touch upon the formalities if the system is a minimal realization or not, because a great amount of effort was put into making sure that the numerical results in Matlab always gave a minimal realization. After it was established that it was possible for the systems under study in this thesis to always obtain minimal realization, no more emphasis were put on the subject. In general, the control theory presented in this appendix is used only as a tool, and is not of importance in itself, as long as no rules are broken, and it is useful.

Also, the topic of the pole and zero direction will not be covered here for brevity, but complete coverage of the topic is found in [48] for reference. This is also related to the statements in the paragraphs above, that in general it is put confidence in that the system representations in this thesis is minimal realizations, and therefore poles and zero at the same frequency that has the same direction is canceled in the minimal realization process, and poles and zeros at the same frequency with a different direction, are not canceled as this is invalid.

D.4 Motivation and Validity of MIMO System Decoupling

For several reasons, it would be advantageous to decouple the converter MIMO system presented in this thesis. But before that can be done, a justification for whether it is possible or not has to be presented. That is what this section of the appendix is dedicated to. Therefore, first, the motivation for decoupling is presented, thereafter an exploration for whether it is possible for the system under study in this thesis is explored.

In the initial phase of this thesis, it was of interest to explore the possibility to decouple the converter MIMO system, both for theoretical and practical reasons. To start with the theoretical, there are certain traits of a diagonal transfer function matrix that will greatly simplify the analysis of stability, traditionally related to the poles and zeros of the system.

The first reason is that for a diagonal transfer function matrix $\mathbf{H(s)}$ the poles and zeros are just the poles and zeros of the individual entries of $\mathbf{H(s)}$ [47]. Compared to the rather complicated definition of MIMO zeros in the last section of this appendix, this is a straight forward definition that is easy to understand and analyze.

The second reason is that keeping the off-diagonal entries of the converter impedance/admittance makes the already high order system explode in size. Consider the three different versions of the minor loop gain, where different elements of the converter and grid transfer function matrices are neglected:

$$\mathbf{L_1(s)} = \begin{bmatrix} Z_{g,dd} & Z_{g,dq} \\ Z_{g,qd} & Z_{g,qq} \end{bmatrix} \cdot \begin{bmatrix} Y_{oi,dd} & Y_{oi,dq} \\ Y_{oi,qd} & Y_{oi,qq} \end{bmatrix} = \begin{bmatrix} Y_{oi,dd}Z_{g,dd} + Y_{oi,qd}Z_{g,dq} & Y_{oi,dq}Z_{g,dd} + Y_{oi,qq}Z_{g,dq} \\ Y_{oi,dd}Z_{g,qd} + Y_{oi,qd}Z_{g,qq} & Y_{oi,dq}Z_{g,qd} + Y_{oi,qq}Z_{g,qq} \end{bmatrix} \tag{D.12}$$

$$\mathbf{L_2(s)} = \begin{bmatrix} Z_{g,dd} & Z_{g,dq} \\ Z_{g,qd} & Z_{g,qq} \end{bmatrix} \cdot \begin{bmatrix} Y_{oi,dd} & 0 \\ 0 & Y_{oi,qq} \end{bmatrix} = \begin{bmatrix} Y_{oi,dd}Z_{g,dd} & Y_{oi,qq}Z_{g,dq} \\ Y_{oi,dd}Z_{g,qd} & Y_{oi,qq}Z_{g,qq} \end{bmatrix} \tag{D.13}$$

$$\mathbf{L_3(s)} = \begin{bmatrix} Z_{g,dd} & 0 \\ 0 & Z_{g,qq} \end{bmatrix} \cdot \begin{bmatrix} Y_{oi,dd} & 0 \\ 0 & Y_{oi,qq} \end{bmatrix} = \begin{bmatrix} Y_{oi,dd}Z_{g,dd} & 0 \\ 0 & Y_{oi,qq}Z_{g,qq} \end{bmatrix} \tag{D.14}$$

The notation is the same as the rest of the thesis $\mathbf{Z_g}$ is the grid impedance transfer function matrix and $\mathbf{Y_{oi}}$ is the equivalent converter output admittance. There are some notes to be made about the difference in $\mathbf{L_1(s)}$, $\mathbf{L_2(s)}$ and $\mathbf{L_3(s)}$. $\mathbf{L_1(s)}$ is the full expression for the minor loop gain where no decoupling is done, in $\mathbf{L_2(s)}$ the converter admittance is decoupled, and in $\mathbf{L_3(s)}$ both transfer function matrices both are decoupled. It is obvious from the three equations that the decoupling will greatly simplify the analysis, however the validity of doing so is another question that will be discussed later.

Another theoretical argument is related to the MIMO converter model from Section 2.3.1 and its corresponding Bode plots were it was discussed that it is the qq-channel that shows negative resistive behavior in the low and medium frequency range. Therefore, it would be nice if this problem can be isolated as studied separately of other system dynamics that in the end may be of no relevance to system stability.

The final theoretical argument for using $\mathbf{L_3(s)}$ compared to $\mathbf{L_1(s)}$ and $\mathbf{L_2(s)}$ is the fact that the closed-loop transfer function $\mathbf{L_{cl}(s)}$ will be much simpler to study. For completeness, the final closed-loop system that is of concern with regards to stability is repeated in Figure D.5.

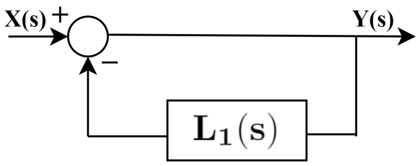

Figure D.5: MIMO closed-loop.

With the closed-loop transfer function matrix $\mathbf{L_{cl}}(\mathrm{s})$ as in (D.15).

$$\mathbf{L_{cl}}(\mathrm{s}) = (\mathbf{I} + \mathbf{L_1}(\mathrm{s}))^{-1} \tag{D.15}$$

If the same symbolic representation from (D.14) is used in can be shown that the expression for $\mathbf{L_{3,cl}}(\mathrm{s})$ is equal to the expression in D.16

$$\mathbf{L_{3,cl}}(\mathrm{s}) = \begin{bmatrix} \frac{1}{Y_{dd}Z_{dd}+1} & 0 \\ 0 & \frac{1}{Y_{qq}Z_{qq}+1} \end{bmatrix} \tag{D.16}$$

The same can be done for $\mathbf{L_1}(\mathrm{s})$ and $\mathbf{L_2}(\mathrm{s})$, but then it can be useful with a symbolic representation software, such as Maple of Matlab. They are not listed here, because the expressions become quite long, but the point is clear anyway. Both $\mathbf{L_{1,cl}}(\mathrm{s})$ and $\mathbf{L_{2,cl}}(\mathrm{s})$ are more complicated systems where it will be more difficult to analyze the stability behavior by looking at the poles of the closed-loop transfer function. With $\mathbf{L_{3,cl}}(\mathrm{s})$ however, it is easier to relate certain poles directly to individual transfer functions. And if $\mathbf{L}(\mathrm{s})$ is diagonal $\mathbf{L_{cl}}(\mathrm{s})$ is also diagonal, so all poles and zeros of $\mathbf{L_{cl}}(\mathrm{s})$ are poles and zeros in the entries in $\mathbf{L_{cl}}(\mathrm{s})$ which will make the analysis easier. Also this expression will make it possible to relate the converter qq-channel admittance, which is of concern, to the closed-loop stability.

A more practical concern that also has to be considered is the fact that very large MIMO systems are difficult to study and even difficult to compute and evaluate correctly for many software simulation packages such as Matlab and Simulink used in this thesis. Earlier thesis work at the Department within the same topic [11] reported that numerical issues plagued the work in all stages of the project. Therefore a lot of effort was spent at the beginning of this thesis work to ensure that the model used was of as low order as possible without losing any important information. A lot can be done directly in Matlab to minimize this problem by use of various internal functions and commands, but also working with a symbolic system representation is critical for not getting a numerical error that creates transfer functions of order that cannot be used for anything. Nevertheless, even though all precautions are taken, the expression in (D.12) will be of a very high order, and it can be difficult to study what is wanted to study, and end up with an adaptive control that works. Therefore, the rest of this section is dedicated to exploring if the system under study in this thesis can represent as in (D.13) or (D.14) compared to (D.12). It should be noted that this thesis is not the first attempt to investigate if it is valid to decouple d and q axis for a similar system and MIMO representation, as similar argumentation was presented in [57].

To explore the possibility for system reduction, an example system was chosen and as only one complete example was found in the literature [13], to compare the results to, this was used. The methodology here is to make reductions /simplifications/ decoupling and see how that effects the dynamical performance in terms of bode plots, pole-zero plots step responses and so on. The starting point would naturally be to build complete converter and grid models, and then calculate $\mathbf{L(s)}$ with no simplifications, i.e. to get a model exactly like that paper, and then try see how decoupling affect the system. Therefore, to start the discussion, consider two bode plots in Figure D.6.

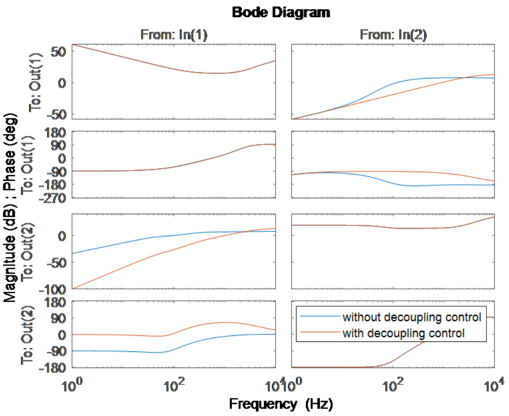

Figure D.6: Converter output impedance with and without decoupling control.

The figure shows the equivalent converter output impedance, $\mathbf{Z_{oi}}$ calculated according to the transfer function matrix derived in Section 2.3.1, with and without decoupling control. The term decoupling control should in this case not be mixed with system decoupling and decoupling control referes to the actual taken on the control side, and system decoupling means decoupling the d and q-axis in general. The effect of the decoupling control results is lower amplitude in the dq and qd channels within the current controller bandwidth, as expected as this is the job of the decoupling term. Another result worth mentioning is the the dd and qq channels are identical regardless of decoupling control or not. Naturally the system with decoupling control is further considered, both because it gives better system performance, but also this correspond to the control system in the laboratory setup, and the system without is discarded.

Now, the next thing to consider is how the system is affected when the dq and qd terms of the transfer function matrix is neglected, and then compare it to the full system. But it will be of more interest to study the equivalent converter admittance instead of the converter impedance, as it is the converter admittance that is used in the stability criterion. Therefore, in the simulation model, first the dq and qd entries of $\mathbf{Z_{oi}}$ is removed, and then $\mathbf{Z_{oi}}$ is inverted to form $\mathbf{Y_{oi,dec}}$. So now $\mathbf{Y_{oi}}$ and $\mathbf{Y_{oi,dec}}$ can be compared. Two comparisons are considered in Figure D.7.

Naturally, there are no entries in the dq and qd channel of $\mathbf{Y_{oi,dec}}$, but the figure clearly show that there is a very good match in the frequency response in the dd and qq channels. As a reminder of what the relevant frequency range is, the system switching frequency is 20 kHz in this example, and since an average converter model is used, only up to about half the switching frequency is relevant, therefore the Bode plot is only plotted for frequencies up to 10 kHz.

In D.7b, the step response of the two systems is shown, and naturally, the dd and qq-channel step response is nearly identical, as the step response is strongly connected to the frequency response representation in the bode plot. Another detail about the plot that shown that the d and q channel is weakly coupled is the low amplitude and short settling time of the dq and qd step responses. This is another indication that it is a good

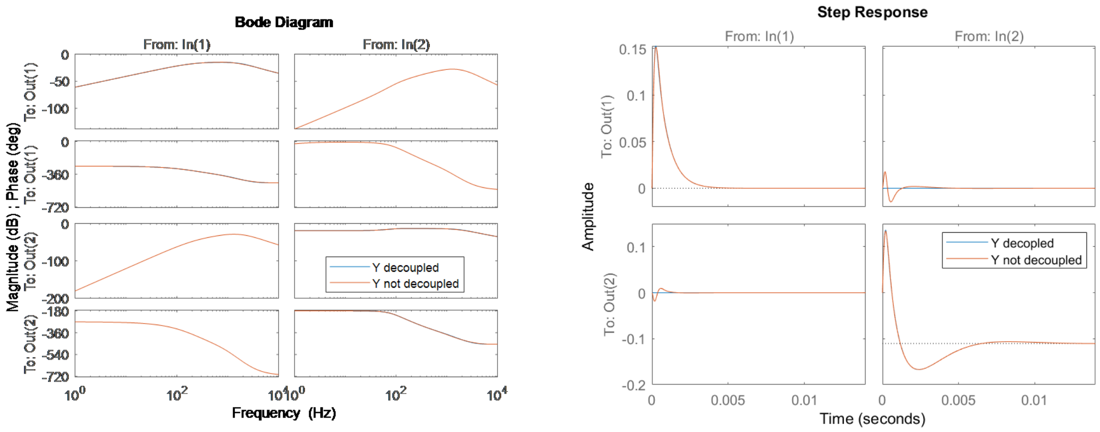

(a) Bode plot of $\mathbf{Y_{oi}}$ vs $\mathbf{Y_{oi,dec}}$.

(b) Step response of $\mathbf{Y_{oi}}$ vs $\mathbf{Y_{oi,dec}}$.

Figure D.7: Comparisons of $\mathbf{Y_{oi}}$ and $\mathbf{Y_{oi,dec}}$.

approximation to decouple the converter impedance. The same conclusion was reached in [65], where a similar small-signal model was created, and the result showed that the cross-coupling impedance was very small and that it can be ignored for unity power factor, which is the case in this thesis.

Even though the bode plot and step response show that the decoupling is a good approximation when it comes to the system response, it gives no information about the placement of poles and zeros. Therefore, consider the two pole-zero plots in Figure D.8, where D.8a is the full system and D.8b the decoupled one. It should be mentioned that both systems have more poles and zeros longer into the LHP, but they are not of interest, and therefore they are not included in the plot.

It is difficult to say anything concrete about the two plots, other than that both are stable since there are no RHP poles for the closed-loop system, and some of the poles and zeros are equal in the two plots. A very nice trait about the pole-zero plot of the decoupled system is that the complete pole-zero information is directly available by just considering the transfer function, as it was derived in the last section that for diagonal transfer function matrices the poles and zeros correspond to the poles and zeros of the entries in Y. Another fact worth mentioning is that there does not need to be a relation between some of the poles and zeros in the two plots at all, because $\mathbf{Y_{oi}}$ is a result of the inversion of $\mathbf{Z_{oi}}$, while $\mathbf{Y_{oi,dec}}$ is a result of the inversion of $\mathbf{Z_{oi,dec}}$, and the inversion process of the MIMO system, in general, have no relation between the poles in $\mathbf{G(s)}$ and the zeros in $\mathbf{G(s)^{-1}}$ as also defined in the last section. Therefore the pole-zero plot is no reliable method to say if the decoupling is valid or not and the only tool that can be used to assess this is the frequency and time-domain responses.

As discussed in the paragraphs above, it seems that it is a valid approach to use the decoupled version of the converter admittance, $\mathbf{Y_{oi,dec}}$. But as discussed in the main part of this thesis it is of little interest to study the converter impedance or admittance on its own, as the converter is connected to the grid. Therefore $\mathbf{L(s)}$ has to be studied, for the three different cases presented in equations D.12, D.13 and D.14 earlier in this section. Consider the bode plots of the three different versions of $\mathbf{L(s)}$ in Figure D.9

The conclusion to draw from this is that the frequency response is nearly identical for the three different

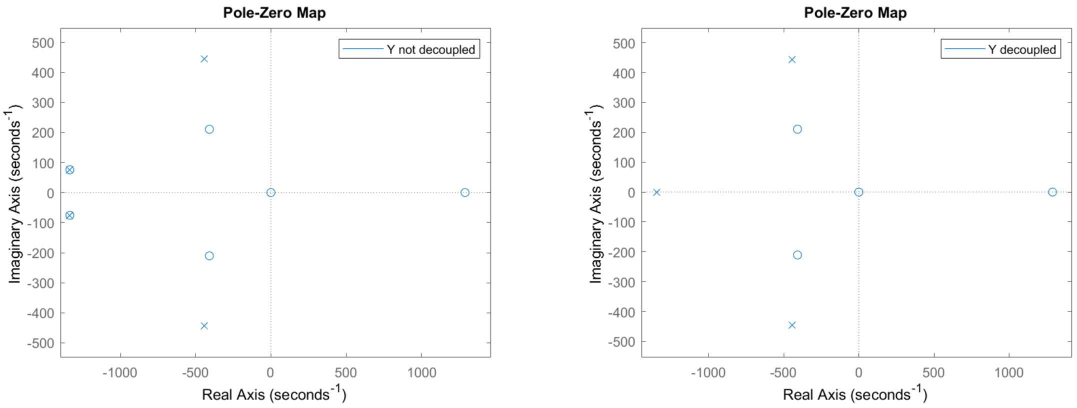

(a) pole-zero plot of $\mathbf{Y_{oi}}$. **(b)** Pole-zero plot of $\mathbf{Y_{oi,dec}}$.

Figure D.8: pole-zero plot of $\mathbf{Y_{oi}}$ and $\mathbf{Y_{oi,dec}}$.

versions of $\mathbf{L(s)}$ in the dd and qq channels. Obviously the entries in $\mathbf{L(s)}$ for when the dq and qd channels in the grid and the converter are zero, and therefore there is no frequency response either. Also the step response for $\mathbf{L(s)}$ in Figure D.10 seems to give the same conclusion. All three systems are also stable, which is nice. Also the pole-zero plot can be studied, but the same issue as earlier arises, even though some poles as zeros seem to be the same in the three versions of $\mathbf{L(s)}$ there is generally no relationship between the three, from the definition. However, it should be noted that for all three systems there are no RHP poles, and one RHP zero in all three systems, and this time only from $\mathbf{L_3(s)}$ the complete pole and zero information can be read from the transfer function directly as $\mathbf{L_3(s)}$ is diagonal, while $\mathbf{L_1(s)}$ and $\mathbf{L_2(s)}$ are not diagonal.

The final part to look at regarding the validity of the decoupling would be the characteristic loci of $\mathbf{L(s)}$ described in the appendix D.2. As $\mathbf{L(s)}$, in this case, is a 2x2 transfer function matrix, there is will be two GNC plots, as $\mathbf{L(s)}$ generally will have two eigenvalues for each frequency it is evaluated at. Also this time Matlab is used to calculate and plot the loci, and the results for $\mathbf{L_1(s)}$, $\mathbf{L_2(s)}$ and $\mathbf{L_3(s)}$ is available in Figure D.11, in the same order.

The GNC plots for the different systems fall under the same category as the pole-zero plots; it is difficult to say anything general about the plots, other that all three indicates that the systems are stable. Also, the shapes of the loci look similar for the three systems, although it could be that there is some numerical bug in $\mathbf{L_1(s)}$ because this system is of a very high order. Another thing worth noting is that the loci of $\mathbf{L_2(s)}$ and $\mathbf{L_3(s)}$ looks very similar which could be another indication that it is valid to consider both a decoupled converter transfer function matrix and a decoupled grid transfer function matrix.

Based on the motivation for a ”simple” system early in this section and thereafter the justification for why decoupled versions of $\mathbf{Y_{oi}}$ and $\mathbf{Z_g}$ can be used later in the section, the version of $\mathbf{L(s)}$ that are to be used for the adaptive control part of this thesis is $\mathbf{L_3(s)}$. It should be noted that using an example to justify the approach always will be flawed because there is no guarantee that it holds in the general case. When that being said, a general approach would be outside the scope of this thesis, and therefore cannot be considered.

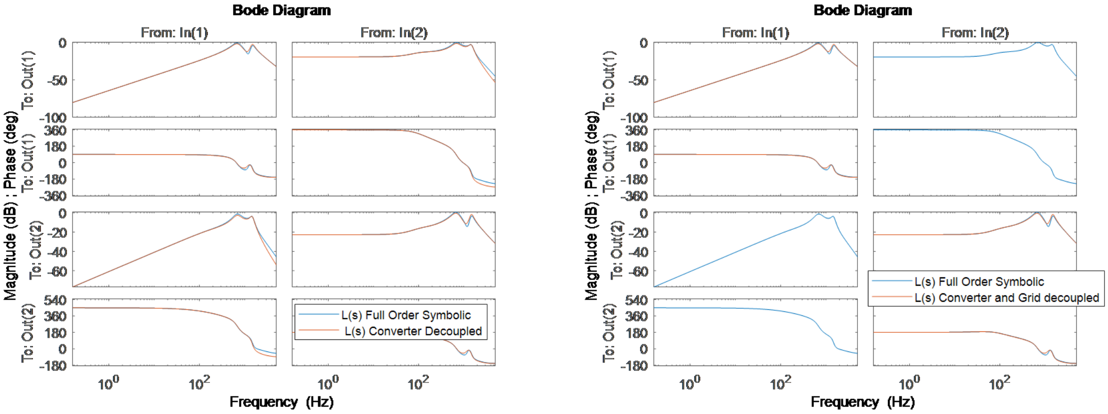

(a) Comparison of $\mathbf{L(s)}$ with no decoupling and $\mathbf{L(s)}$ converter decoupling. **(b)** Comparison of $\mathbf{L(s)}$ with no decoupling and $\mathbf{L(s)}$ with grid and converter decoupling.

Figure D.9: Bode plots of different variants of $\mathbf{L(s)}$.

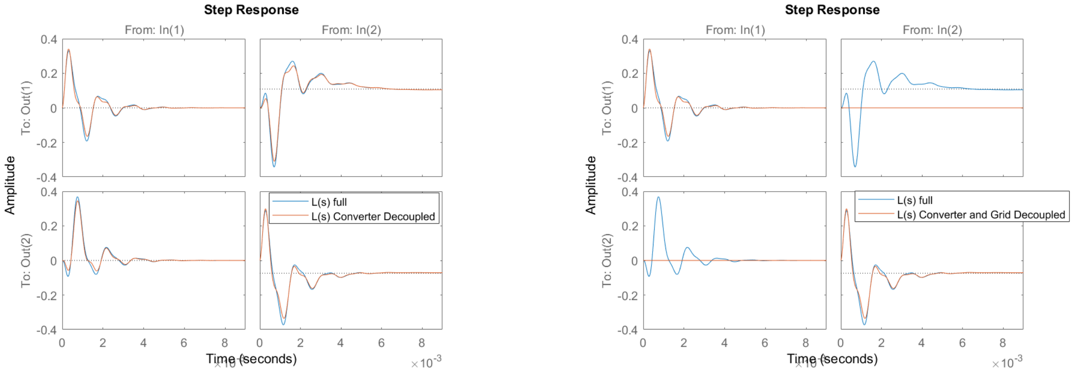

(a) Step response comparing $\mathbf{L_1(2)}$ and $\mathbf{L_2(s)}$. **(b)** Step response comparing $\mathbf{L_1(2)}$ and $\mathbf{L_3(s)}$.

Figure D.10: Step responses of $\mathbf{L_1(2)}$, $\mathbf{L_2(2)}$ and $\mathbf{L_3(s)}$.

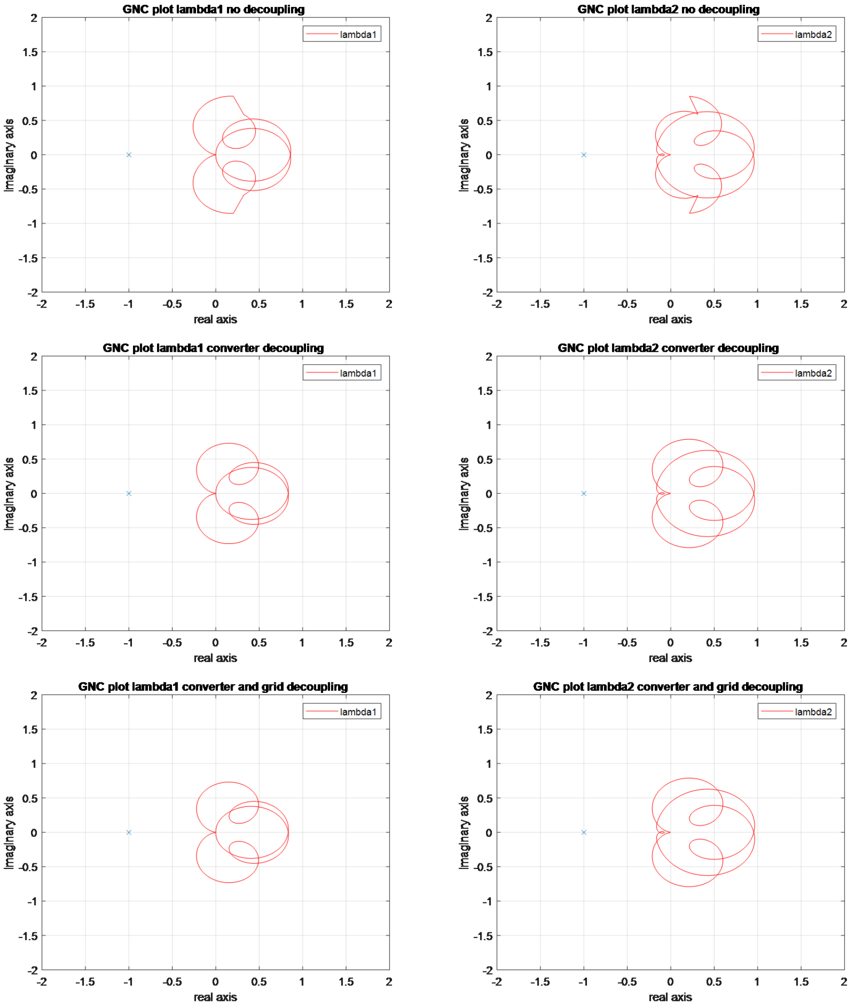

Figure D.11: Numerical bug in the top one makes new figure by using method 3, and the three plots will be even more similar also consider changing to the one that is above stability limit.

Appendix E

Derivation MIMO transfer function Matrices for Converter Modeling

In Subsection 2.3.1, three transfer function matrices $\mathbf{G^v_{PLL}}$*,* $\mathbf{G^d_{PLL}}$ *and* $\mathbf{G^i_{PLL}}$ *were defined, but not derived. therefore this appendix will show that the definitions comes from straightforward small-signal modeling. Like Subsection 2.3.1, this appendix is also heavily based on [13]*

The rotation matrix $\mathbf{T_{\Delta\theta}}$ was defined as:

$$\mathbf{T_{\Delta\theta}} = \begin{bmatrix} cos(\Delta\theta) & sin(\Delta\theta) \\ -sin(\Delta\theta) & cos(\Delta\theta) \end{bmatrix} \tag{E.1}$$

and the relation between the voltages, currents and duty cycles in the system reference frame and controller reference frame as

$$\mathbf{v^c} = \mathbf{T_{\Delta\theta} v^s}, \mathbf{i^c} = \mathbf{T_{\Delta\theta} i^s}, \mathbf{d^c} = \mathbf{T_{\Delta\theta} d^s} \tag{E.2}$$

to show that the expressions in Subsection 2.3.1 is correct, it is enough to consider one of the systems, as the two others are derived in the same manner. Therefore consider the initial angle to be zero and add a small-signal perturbation $\Delta\tilde{\theta}$ for example to the relation between system voltage and controller voltage:

$$\begin{bmatrix} V^c_d + \tilde{v}^c_d \\ V^c_q + \tilde{v}^c_q \end{bmatrix} = \begin{bmatrix} cos(0+\Delta\tilde{\theta}) & sin(0+\Delta\tilde{\theta})) \\ -sin(0+\Delta\tilde{\theta})) & cos(0+\Delta\tilde{\theta})) \end{bmatrix} \begin{bmatrix} V^s_d + \tilde{v}^s_d \\ V^s_q + \tilde{v}^s_q \end{bmatrix} \tag{E.3}$$

As it is assumed that $\Delta\tilde{\theta}$ is a small angle, a small angle approximation of the rotation matrix is shown in (E.4).

$$\begin{bmatrix} V^c_d + \tilde{v}^c_d \\ V^c_q + \tilde{v}^c_q \end{bmatrix} \approx \begin{bmatrix} 1 & \Delta\tilde{\theta} \\ -\Delta\tilde{\theta} & 1 \end{bmatrix} \begin{bmatrix} V^s_d + \tilde{v}^s_d \\ V^s_q + \tilde{v}^s_q \end{bmatrix} \tag{E.4}$$

To get a relation between the PLL and voltage disturbance, the PLL controller transfer function has to be considered. In this thesis the controller for the PLL is a standard PI controller, defined by its transfer function H_{pll}.

$$H_{PLL} = K_{p,PLL} + \frac{K_{i,PLL}}{s} \tag{E.5}$$

From Figure B.3, that shows the transfer function for a PLL, it is evident that the output angle of the PLL is equal to the relation is (E.6).

$$\Delta\tilde{\theta} = \tilde{v}_q^s H_{PLL} \frac{1}{s} \tag{E.6}$$

If the expression for $\Delta\tilde{\theta}$ from (E.6) is substituted into (E.5), the relation between PLL output angle and q-channel voltage is defined as:

$$\Delta\tilde{\theta} = \frac{H_{PLL}}{s + V_d^s H_{PLL}} \tilde{v}_q^s \tag{E.7}$$

To simplify the expression, G_{PLL} is defined as

$$G_{PLL} = \frac{H_{PLL}}{s + V_d^s H_{PLL}} \tag{E.8}$$

and

$$\Delta\tilde{\theta} = G_{PLL} v_q^s \tag{E.9}$$

Finally this gives a relation between the controller frame voltage vector and the system frame voltage vector, with the closed-loop PLL dynamics captured:

$$\begin{bmatrix} \tilde{v}_d^c \\ \tilde{v}_q^c \end{bmatrix} \approx \begin{bmatrix} \tilde{v}_d^s + V_q^s G_{PLL} \tilde{v}_d^s \\ -V_d^s G_{PLL} \tilde{v}_q^s + \tilde{v}_q^s \end{bmatrix} = \begin{bmatrix} 1 & V_q^s G_{PLL} \\ 0 & 1 - V_d^s G_{PLL} \end{bmatrix} \begin{bmatrix} \tilde{v}_d^s \\ \tilde{v}_q^s \end{bmatrix} \tag{E.10}$$

It then follows from Subsection 2.3.1 that $\mathbf{G_{PLL}^{v}}$ is the transfer function matrix with controller frame voltage as output and system voltage frame as input, so:

$$\mathbf{G_{PLL}^{v}} = \begin{bmatrix} 1 & V_q^s G_{PLL} \\ 0 & 1 - V_d^s G_{PLL} \end{bmatrix} \tag{E.11}$$

The same method can be done to get relation between current system and controller frame, and duty cycle controller and system frame, and they are defined below.

$$\begin{bmatrix} \tilde{d}_d^s \\ \tilde{d}_q^s \end{bmatrix} \approx \begin{bmatrix} 0 & -D_q^s G_{PLL} \\ 0 & D_d^s G_{PLL} \end{bmatrix} \begin{bmatrix} \tilde{v}_d^s \\ \tilde{v}_q^s \end{bmatrix} + \begin{bmatrix} \tilde{d}_d^c \\ \tilde{d}_q^c \end{bmatrix} \tag{E.12}$$

which results in

$$\mathbf{G_{PLL}^{d}} = \begin{bmatrix} 0 & -D_q^s G_{PLL} \\ 0 & D_d^s G_{PLL} \end{bmatrix} \tag{E.13}$$

and

$$\begin{bmatrix} \tilde{i}_d^c \\ \tilde{i}_q^c \end{bmatrix} \approx \begin{bmatrix} 0 & I_q^s G_{PLL} \\ 0 & -I_d^s G_{PLL} \end{bmatrix} \begin{bmatrix} \tilde{v}_d^s \\ \tilde{v}_q^s \end{bmatrix} + \begin{bmatrix} \tilde{i}_d^s \\ \tilde{i}_q^s \end{bmatrix} \tag{E.14}$$

which results in

$$\mathbf{G^i_{PLL}} = \begin{bmatrix} 0 & I^s_q G_{PLL} \\ 0 & -I^s_d G_{PLL} \end{bmatrix} \tag{E.15}$$

The reader should notice that $\mathbf{G^i_{PLL}}$ and $\mathbf{G^v_{PLL}}$ has controller frame as output and system frame as input, and $\mathbf{G^v_{PLL}}$ has system frame as output and controller frame as input. The reason for this is clear from Figure 2.14, which is illustrated again for clarity. The PLL clearly affect the voltage and current reference frames in the input stage i.e. with system reference frame as input and controller reference frame as output. The opposite is the case for the duty cycle behavior i.e the transfer function has system reference frame as output and controller reference frame as input.

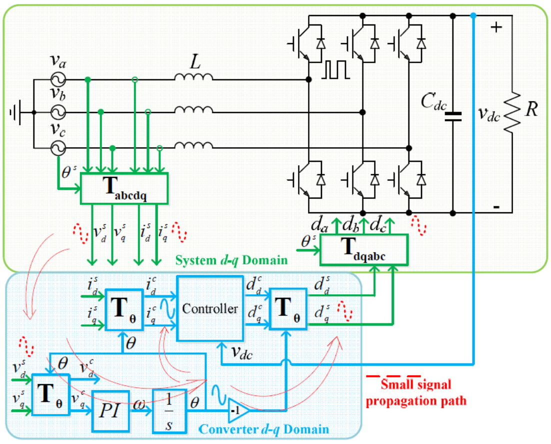

Figure E.1: Illustration of system and controller dq-frame [23].

In (E.13) the steady state duty cycle values in the dq-frame, D_d and D_q were defined, without any further information on how to find these for a certain operating point. This can be defined directly from the small-signal circuit equivalent itself, in Figure 2.11, which is repeated below for completeness.
More specifically, in steady state the d and q channels have a corresponding steady-state circuit equivalent, where KVL can be applied directly to find the expression for D_d and D_q, as seen in (E.16) and (E.17).

$$D_d = \frac{V_d + R_c I_d - \omega L_c I_q}{V_{dc}} \tag{E.16}$$

$$D_q = \frac{V_q + R_c I_q + \omega L_c I_q}{V_{dc}} \tag{E.17}$$

Naturally in this expression the inductor currents are equal to the current reference, and all other variables and parameters are known as well, so therefore it is straight forward to calculate the duty cycles.

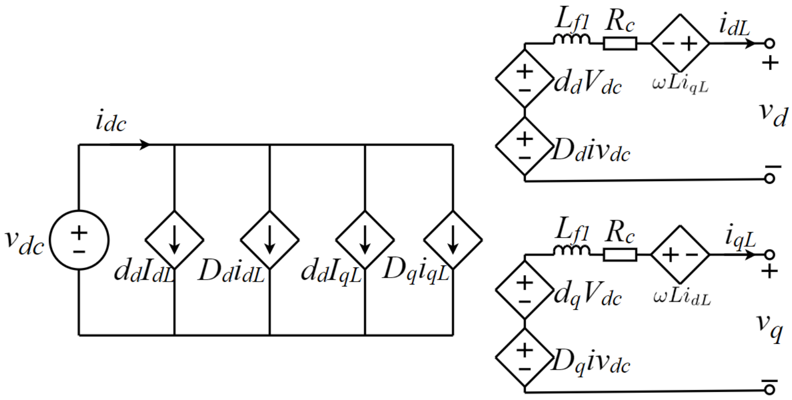

Figure E.2: Small-signal model.

Appendix F

Control Parameter Selection and Tuning for Base-Case

An initial problem in the simulation phase of this thesis was to find suitable control parameters to use as a base-case. The main reason for this comes from the fact that in own previous work, a per-unit control structure was used. However, when the complete MIMO converter model from Section 2.3.1 is to be used, this one is nice to work with when all transfer functions are in real values. This means that also the control variables have to be valid for a not per-unit control system.

Also, for the adaptive control method in Chapter 3 it is very useful if both the PLL and the current controller can be represented with one parameter i.e. the bandwidth. There are many ways to make a controller with a specific bandwidth so this appendix will try and clear up how the controllers are represented.

After appropriate initial control variables are found, the system is tuned and the complete model is validated in the last section of this appendix.

F.1 PLL Control Parameters

As one of the main contributions in this thesis is the adaptive selection of the PLL control parameters, it is important to define good base-case control parameters that are supposed to work for a wide range of operating conditions. A natural starting point would be to consider the small-signal PLL transfer function, repeated in (F.1).

$$G_{pll} = \frac{G_{c,pll}}{s + V_d^s G_{c,pll}} \tag{F.1}$$

where $G_{c,pll}$ is the PLL PI controller transfer function. The transfer function in (F.1) is expanded to form a more complete expression, and the result can be seen in (F.3)

$$G_{pll} = \frac{K_{p,pll}\frac{1+T_{i,pll}s}{T_{i,pll}s}}{s + V_d^s K_{p,pll}\frac{1+T_{i,pll}s}{T_{i,pll}s}} \tag{F.2}$$

The denominator expression is a second-order transfer function, which can be written on standard form represented by its relative damping coefficient ζ and the cutoff frequency ω_c:

$$s^2 + V_d^s K_{p,pll} s + \frac{V_d^s K_{p,pll}}{T_{i,pll}} = s^2 + 2\zeta\omega_c s + \omega_c^2 \tag{F.3}$$

solving this equation for $K_{p,pll}$ and $T_{i,pll}$ where ω_c and ζ is selected based on wanted behavior the final expressions for the control parameter are listed in (F.4) and (F.5) and in (F.6) is found as the ratio of $K_{p,pll}$ and $T_{i,pll}$, or directly where the variables are substituted in.

$$K_{p,pll} = \frac{2\zeta\omega_c}{V_d^s} \tag{F.4}$$

$$T_{i,pll} = \frac{2\zeta}{\omega_c} \tag{F.5}$$

$$K_{i,pll} = \frac{K_{p,pll}}{T_{i,pll}} = \frac{\omega_c^2}{V_d^s} \tag{F.6}$$

As the selection of the parameter, ζ will result in a compromise between overshoot and settling time, a fairly standard value of $\zeta = \frac{1}{\sqrt{2}}$ is selected for this thesis. This was also selected in [13] for a similar small-signal PLL parameter selection. Now to the important part, which is what bandwidth the PLL should have. Before selecting the bandwidth for the system under study in this thesis, it is important to remember what the function of the PLL is. The PLL should give an accurate estimate of the grid frequency at all times, where the bandwidth should be low enough to work as a low pass filter for unwanted noise, but high enough that variations in grid frequency are picked up. Also from Subsection 2.3.1 it was shown that a high PLL bandwidth is beneficial for faster dynamic response to disturbances, but that it may lead to resonance problems between the grid and converter, especially when the grid impedance increases. This was shown directly in [12] and indirectly in [13] as well as countless times in this thesis. So for the base-case that should be a compromise between fast dynamic response and robustness to increased grid impedance. In [59] the bandwidth range is specified to be within approximately 800 Hz and 50Hz for a similar setup, where it was suggested that a high bandwidth was to be used for initial lock, while a low bandwidth can be used for steady-state conditions. In this thesis, it is assumed that online grid measurements are available, and therefore the PLL can be operated at a bandwidth that meets the grid conditions. In normal grid conditions, this allows for a higher PLL bandwidth than one would normally use if only robust control were applied.

One important thing that should be noted in the expressions in (F.4) and (F.6) is that ω_c is not the same as the bandwidth of the PLL controller. From background theory, the bandwidth is known as the value where the magnitude is -3dB lower than the dc response, while ω_c is the cutoff frequency of the transfer function. However, if ζ is kept constant, as it is in this thesis, there is a linear relationship between the two approximately equal to the expression in (F.7). This linear relation is not general, and the constant depends on the components in the small-signal PLL transfer function G_{pll} and the selected ζ value. Therefore this cannot be used if ζ is changed, and if this is the case the user should use the cutoff frequency directly instead.

$$\omega_{bw} = 2.0557\omega_c \tag{F.7}$$

And naturally the same relation in Hertz. This can easily be verified in for example Matlab with a Bode plot.

Most of the Bode plots in this thesis in frequency unit Hz because it is easier to have a relation to. Also for the adaptive control implemented in Chapter 3. To further clarify it is the bandwidth that is of interest, not the cutoff frequency. Therefore, care should be applied when using the cutoff frequency for calculating the control parameters in (F.4)-(F.6), and the easiest solution to this is substituting the expression for bandwidth directly in.

Other more conventional methods can be used to derive PLL bandwidth, for example by using the large-signal representation of PLL the closed-loop transfer function. This is done in early work in [59] and [64] and later work in [12]. If this is the case, then T_{pll} from Section 2.3.1 is used instead of G_{pll}, But both the methodology and results are the same, where the control parameters are directly derived from the two input variables ω_c and ζ.

One common theme occurring in the literature is that the PLL bandwidth for the large-signal PLL transfer function should not be below the fundamental grid frequency, so this is also the case for the small-signal PLL bandwidth. This should also be kept in mind for the adaptive part so that the bandwidth, in this case, is not reduced to be lower than 50 Hz. It should be verified if the MIMO converter model captures this dynamic, and if this is not the case, then there should be applied a lower limit to the PLL bandwidth, for example, 50 Hz. It is not like the bandwidth of 50 Hz is some ”magic limit” and the PLL is completely dysfunctional for bandwidths below this, but for simplicity, bandwidths lower than 50 Hz is not considered. One might argue that for example if the bandwidth is set to 40 Hz, the attenuation and phase delay of a 50Hz signal is -5dB and -72.4° respectively compared to a bandwidth of 50 Hz, where attenuation and phase delay is -3dB and -66.9°. It is possible that the PLL can function at lower bandwidth than the fundamental grid frequency, but for simplicity, this is not considered in this thesis.

For this thesis, the luxury of having a very detailed model allows for testing a range of different PLL bandwidths, and investigating the result is several different ways. Therefore consider the two plots in Figure F.1

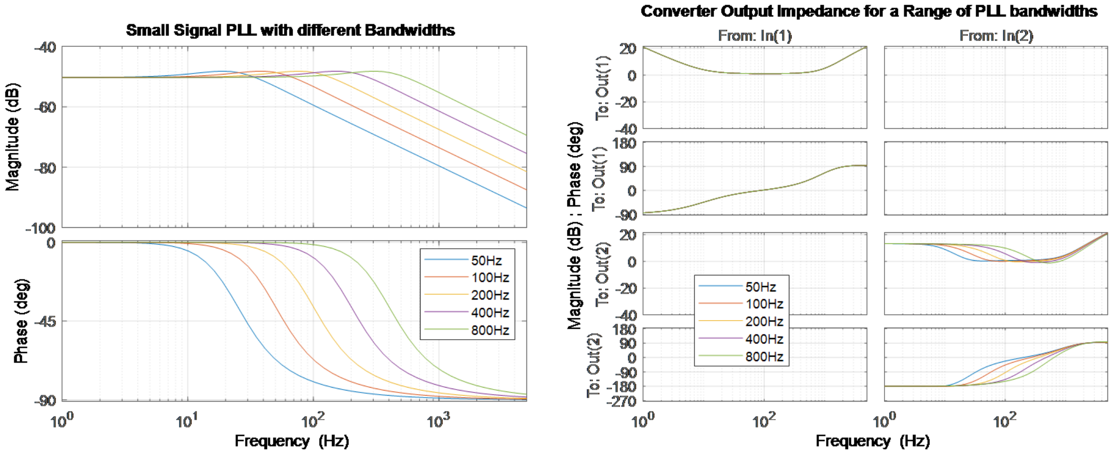

(a) Small Signal PLL for a range of PLL bandwidths. **(b)** Converter output impedance for a range of PLL bandwidths.

Figure F.1: Small Signal PLL Bode plots are resulting in PLL output impedance.

As expected, the dd-converter impedance is unchanged for the different PLL bandwidths, in line with presented theory in the main part of this thesis and other similar results from the literature, for example, [13].

Higher PLL bandwidth results in a larger frequency range of negative incremental resistive behavior in the qq-channel.As mentioned before it is limited how much information that can be extracted from the Bode plot of the converter impedance alone. Therefore, to investigate the closed-loop stability, when the grid is taken into account, and $\mathbf{L}(\mathbf{s})$ and $\mathbf{L_{cl}}(\mathbf{s})$ is formed for the five different PLL controllers. In all cases, the grid impedance is set to a low value, because for the base-case it is assumed that the converter operates under strong grid conditions. But to illustrate the importance of selecting an appropriate PLL bandwidth, another simulation case with a higher grid impedance is done, and the step response $\mathbf{L_{cl}}(\mathbf{s})$ for the six different PLL controllers, with a negligible and medium level of grid impedance is shown if Figure F.2

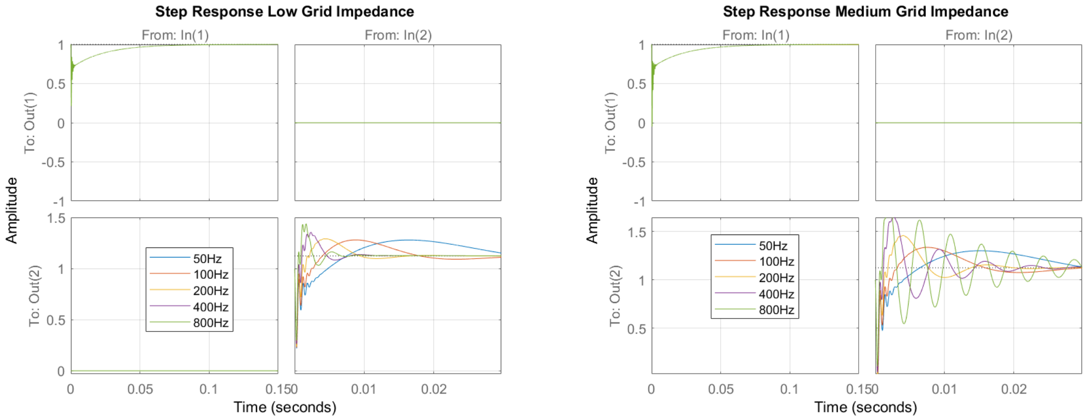

(a) Step response of $\mathbf{L_{cl}}(\mathbf{s})$ low grid impedance.

(b) Step response of $\mathbf{L_{cl}}(\mathbf{s})$ medium grid impedance.

Figure F.2: Step response of $\mathbf{L_{cl}}(\mathbf{s})$ for a range of PLL controllers under low and medium grid impedance.

The amplitude axis is the same in the two plots for comparison. For the first case, when the grid impedance is neglectable, the result is as expected. The step response in qq-channel is faster for higher PLL bandwidth, and the step response in dd-channel is the same for all cases. But for the other case, in Figure F.2b, this is not the case. The first thing that stands out is that the performance is significantly worse for the 800 Hz bandwidth controller compared to the other. This is related to the theory presented in the main section of the thesis and will therefore not be covered here. Naturally, this trend will continue for higher grid impedance, where the system eventually goes unstable. In this thesis, the luxury of adaptive control is present, so hopefully cases like this will be picked up and handled swiftly by the control system. For now, it should only be noted that for the base-case it could seem like selecting a very high PLL bandwidth is a reasonable choice, but care has to be taken if there is no plan of implementing a control system that takes grid impedance into account.

With this in mind, the base-case PLL controller for this thesis is selected to have a bandwidth of 500 Hz, i.e. ten times the grid frequency. With this choice, there will be a fast dynamic response in the closed-loop system, and since adaptive measures will be implemented there is no need to worry about instability for medium to high grid impedance values. Using the formulas derived earlier in this section, this results in control parameters with a value of $K_{p,pll} = 6.6175$, and $K_{i,pll} = 7151$.

F.2 Current Control Parameters

For the current controller, a more pragmatic approach is taken compared to the one above. The current controller is not the center of interest, at least not for the first adaptive method presented in this thesis. Values should be chosen such that the current controller interferes as little as possible with the rest of the system. However, some guidelines have to be followed, for example, that the current controller bandwidth should be much lower than the switching frequency, and that the bandwidth should be high enough to follow requested changes in reference fast enough. However, even though the current controller is not the center of interest, the control parameters have to be selected with great care, because they affect system stability. In [14] this is discussed in detail, and also what effect the current controller has in a weak grid situation. Also, own previous work in [16] suggested that tuning of the current controller for weak grid condition can keep the system stable for a higher grid impedance value.

In [13] a very similar inverter setup is discussed with similar current, voltage, and current ratings. The control parameters used there was reported to be $K_p = 0.0105$ and $K_i = 1.15$. For comparison, the setup in the NSGL has a per-unit control system where the control parameters used are $K_{p,pu} = 0.5$ and $K_{i,pu} = 65$. to transfer this to a not per-unit system, one possible approach is to simply divide by the base current, which is 142.89A, which results in $K_p = 0.0035$ and $K_i = 0.45$. This can indicate that starting parameters can be in this range, depending on how high or low bandwidth that is chosen.

A more analytical approach would be to do the same as for the PLL controller in the previous section, find approximate low order open-loop transfer function and then find control parameters with methods such as Symmetrical optimum or Modulus Optimum. This is discussed in another appendix, Appendix B.3, where the standard simplified current-control open-loop is presented, and where control parameters easily can be found with Modulus Optimum. If this is done for the system under study in this thesis, the parameters that come out are $K_p = 0.0093$ and $K_i = 0.6739$, so this is a natural starting point. Also, it should be noticed that the Modulus Optimum gives control values quite close the control parameters from the laboratory setup when divided by the base value.

It should be noted that for this thesis a higher bandwidth on the current controller than what would normally be used should be considered. The reason for this is that with this choice the approximation of decoupled d and q channel inverter impedance is better because the coupling effect is suppressed for a larger frequency range. However, the current controller bandwidth should not be pushed artificially high for the base-case, as too high bandwidth will lead the system to be closer to the stability limit.

The initial parameters for the full system were initially selected as the parameters output from this modulus optimum. With these two parameters, the system was unstable. This was no surprise, as this method unusually does not leave enough margins compared to a more realistic system such as the MIMO converter model presented in this thesis. The gain and bandwidth was simply too high, and after some minor modifications, a stable operating point was found with $K_p = 0.0016$ and $K_i = 0.1007$.

As for the PLL, it is generally preferred to have one variable to represent the current controller, especially in this thesis where adaptive current control is to be implemented. This can be done with the use of a modified version of the Modulus Optimum method, which was done in this thesis. The Modulus Optimum applied on a grid-connected inverter consisted of an open-loop transfer function with three blocks, the controller, a time delay PWM block, and the plant/process block. This is covered for example in [14]. As the method itself is not of interest it will not be repeated here. If the method in [14] is used in can be shown that the expression in (F.8) holds.

$$\omega_{cc} = \sqrt{\frac{K_{p,cc}}{LT_{del}}} \tag{F.8}$$

L is, in this case, the first filter inductor, T_{del} is the time delay time constant in the PWM block. If numerical values for ω_{cc} is computed for the base-case, a measure for the current controller bandwidth is obtained, which is what is wanted. But the expression so far has no information about the integral gain. In the normal Modulus Optimum method, T_i is selected to cancel out the dominant time constant, but another approach was selected in this thesis, where increasing K_i with a proportional amount for changing K_p, with the base-case as reference. This may sound like the same thing, but the results are slightly different. If the base-case is poorly defined, this is not a good approach, but for this thesis, the base-case was confirmed to work fine. The result is that for increasing K_p, which is only affecting the magnitude of the open-loop current controller, the cutoff frequency should also be increased. In practical terms this can be solved for example in Matlab, where first a vector of ω_{cc} is generated, then (F.8) is solved for $K_{p,cc}$, then for all values of $K_{p,cc}$ the proportionality factor is used to obtain values of $K_{i,cc}$. An example can be seen in Figure F.3

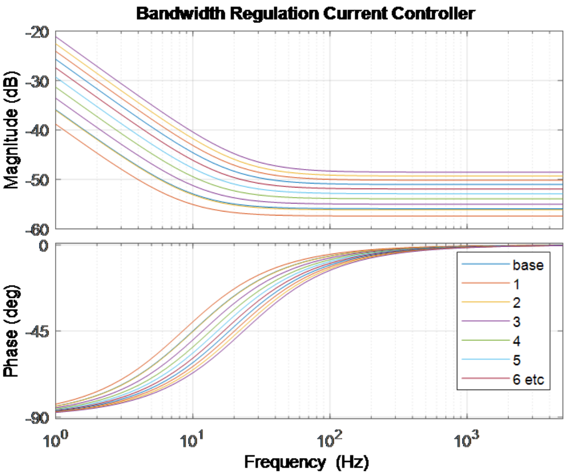

Figure F.3: Bode plot of open-loop current controllers generated by the variable ω_{cc} with the modified modulus optimum method.

The main advantage of this simple and pragmatic method is that the shape of the base-case current controller is kept, which again results in an easier study of the system dynamics when the current controller is adapted to grid condition. Also, it is very handy to just tweak on on variable, and that this variable, ω_{cc} represents a property of the current controller, rather than the "meaningless" numerical values K_p and K_i. It also ensures that when the system is to be simulated over a large range of current control parameters, the user can make sure the base-case is represented by having the base-case ω_{cc} somewhere in the current controller vector.

Some more comments need to be made of the selected way of representing the current controller by ω_{cc}. First of all, the numerical value in rad/s or Hertz, may not represent the actual numerical value of the bandwidth at all. For example, for the base-case of $K_p = 0.0016$ and $K_i = 0.1007$, ω_{cc} computes to 163.2 rad/s, which in hertz is 26 Hz. In no way should this "bandwidth" be directly translated to other large-signal models, because it is just a measure that seems to work well for the models in this thesis, and the numerical value should for the entirety of this thesis be taken with a grain of salt.

F.3 Verification of Base-Case

Luckily, it is quite easy to test if the base-case system parameters make sense, at least as a simulation exercise when laboratory equipment is not available. The reason for this is that there is very similar models in the literature, and therefore the approach is to get results that makes sense compared to these. After some tuning of the PLL and current control parameters from the last two sections the base-case control parameter were selected to be as in Table F.1 below. The resulting converter impedance with the above control parameters

Parameter	Value
K_p	0.0016
T_i	15.9 ms
K_i	0.1007
$f_{bw,pll}$	500 Hz
$f_{c,pll}$	243.23 Hz
$K_{p,pll}$	6.62
$T_{i,pll}$	0.925 ms
$K_{i,pll}$	7151

Table F.1: Base-case control parameters.

and the other system parameters from Appendix G is plotted in Figure F.4a and compared with a similar laboratory setup from the literature in Figure F.4b. In F.4b the bode plot of grid impedance is also included marked in black, but this is not of interest for now.

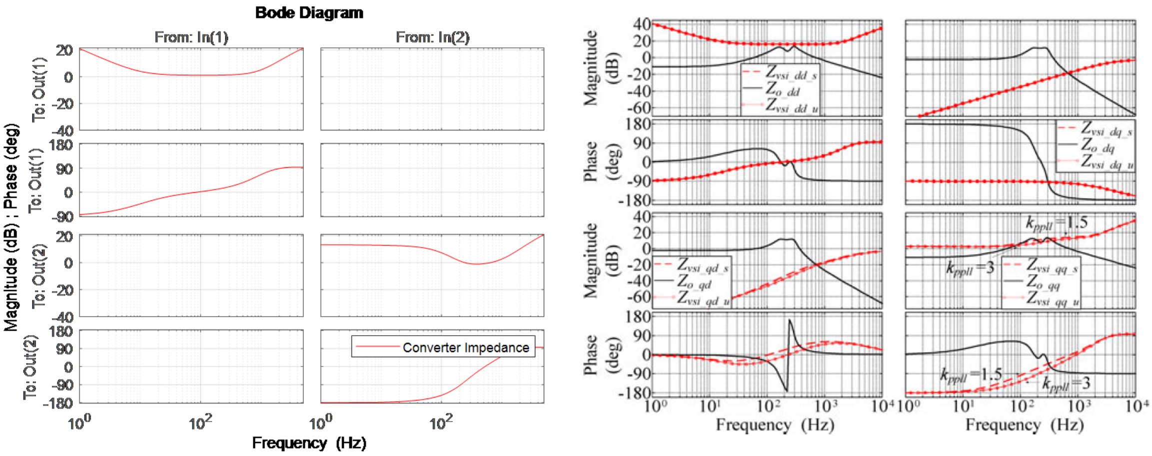

(a) Base-Case Impedance dq Bode plot.

(b) dq impedance plot from the literature [13].

Figure F.4: Comparing base-case impedance plot from a similar case from the literature

As the dq and qd channels will be neglected anyway, in accordance with the theory presented in Appendix D.4, only dd and qq channel similarities and differences are of interest in the bode plots. As explained earlier, the dd amplitude is formed by the current controller at low frequencies, which is clearly visible in both figures. How long it takes before the slope flattens out, and the degree of the slope depends on K_i and K_p, and also the relation between them, but in general the two dd amplitudes are quite similar. One clear distinction between the two dd-plots is the the much lower gain in the base-case. Bigger current control integral gain results in bigger dd-channel amplitude [25], but this again is tied to the behavior of the system. K_i is tuned with this is mind, but tuning showed that increasing K_i even more than what is specified in Table F.1 just results in poorer dynamic performance. For high frequencies the power stage impedance dominates the amplitude, which is the case for both system.

In the qq-channel negative resistive behavior can be observed for both systems, as expected, and a difference in the two plots is the noticeable higher PLL bandwidth for the base-case. The reason for is that in the converter model in F.4b the grid impedance is very high, and therefore the PLL bandwidth is reduced a lot to make sure there is no resonance between the grid at the converter. This topic is discussed more in depth in Chapter 3. Based on this, the converter model looks to be a good base-case, but before it can be certain that this operating point is sufficient, the minor-loop gain $\mathbf{L}(\mathbf{s})$ stability also has to be considered. As discussed earlier, both the GNC where $\mathbf{L}(\mathbf{s})$ is used, and the pole placement in $\mathbf{L_{cl}}(\mathbf{s})$ can be used to determine closed-loop stability. In this case where the analysis is not of interest, only the stability conclusion for normal grid condition the latter is used. In F.5b The base-case converter model is used to calculate the minor loop gain closed-loop $\mathbf{L_{cl}}(\mathbf{s})$ for two grid impedance values, one low and one high.

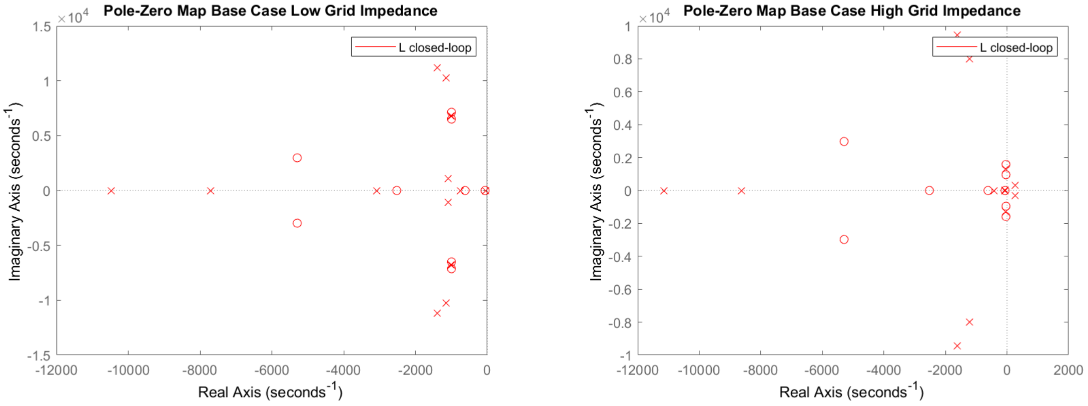

(a) Pole-Zero Map of $\mathbf{L_{cl}}$ Low Grid Impedance.

(b) Pole-Zero Map of $\mathbf{L_{cl}}$ High Grid Impedance.

Figure F.5: Pole-Zero Plots of $\mathbf{L_{cl}}$ for Low and High Grid Impedance Values

The plot indicate that the selected base model is stable for the nominal grid impedance value and unstable for very high grid impedance. The same conclusion was drawn from the open-loop transfer function $\mathbf{L}_(\mathbf{s})$ and the eigenvalue loci plots also moderately high values of grid impedance values were tested and the base-case worked up to a high value of grid impedance, but this is discussed more in Chapter 3 and will not be touched more upon here.

Therefore it can be said with a high level of confidence that the base-case control parameter is well thought out and will serve as a good starting point for the adaptive control in Chapter 3.

Appendix G

Per-unit system, System Parameters and Operating Point

In general, a per-unit system is adopted when it is convenient to scale equations and variables so that most of the values lie in the range 0 to 1, or slightly above. The definition of a per-unit value for an arbitrary variable X is given in (G.1).

$$X_{pu} = \frac{X_{actual}}{X_{base}} \tag{G.1}$$

For the selection of base values for this thesis, they were selected to be in accordance with the experimental setup in the National Smart Grid Laboratory (NSGL) and previous work in [11]. By selecting the base voltage and base apparent power, all other base values can be derived. The base voltage, V_b, is selected to be equal to the system phase-to-neutral peak voltage, $V_{phase,peak}$, and the apparent power to be equal to the rated power to the system:

$$V_b = V_{phase,peak} = \sqrt{\frac{2}{3}} V_{LL,RMS} = \sqrt{\frac{2}{3}} 400V \tag{G.2}$$

$$S_b = 70KVA \tag{G.3}$$

As mentioned all the other base values can be derived from these two values, which is done below. Numerical values are listed in table G.1.

$$I_b = I_{phase,peak} = \frac{2}{3}\frac{S_b}{V_b} \tag{G.4}$$

$$Z_b = \frac{V_b}{I_b} \tag{G.5}$$

Furthermore, the base angular frequency, ω_b, is defined to be equal to the grid angular frequency, i.e. $\omega_b = 2\pi f_g$, where f_g is the grid frequency. Then base values for inductance and capacitance can also be defined.

$$L_b = \frac{Z_b}{\omega_b} \tag{G.6}$$

$$C_b = \frac{1}{z_b \omega_b} \tag{G.7}$$

From the base values defined Table G.1 the specific system under study in this thesis can also be defined. To

Base Quantity	Symbol	Value
Power	S$_b$	70 KVA
Voltage	V$_b$	326.60 V
Current	I$_b$	142.89 A
Angular frequency	ω_b	100π rad/s
Impedance	Z$_b$	2.29 Ω
Inductance	L$_b$	728.9 mH
Capacitance	C$_b$	139.0 mF

Table G.1: Numerical base values used in this thesis.

not repeat theory covered in the main part of the thesis and other appendices, all relevant parameters are only listed here, and not derived and explained again. For example the duty cycle parameters D_d and D_q are only valid for this specific operating point, and the d and q-axis current references, which is a input to the MIMO converter model. When it comes to control parameters these are only valid for the base-case, and does not hold anymore for changing grid conditions, when the adaptive control system kicks in. How the base-case control parameters are found and validated is available in Appendix F. The system parameters are selected to be in line with a specific laboratory setup at the NSGL, but some of the parameters are exclusive for the simulation cases. This includes the damping resistor of the filter, and the equivalent converter resistance.

Quantity	Symbol	Value
DC voltage	V_{dc}	700 V
AC RMS phase-phase grid voltage	V_g	400 V
d-channel grid voltage	V_d^s	326.6 V
q-channel grid voltage	V_q^s	0 V
Grid frequency	f_g	50 Hz
Grid inductance	L_g	0.1 mH
Switching frequency	f_{sw}	10 kHz
Filter inductor 1	L_{f1}	400 μH
Filter inductor 2	L_{f2}	350 μH
Filter capacitor	C_f	60 μF
Equivalent grid resistance	R_g	0.5 Ω
Equivalent converter resistance	R_c	0.029 Ω
Filter damping resistance	R_d	0.3 Ω
d-channel current reference	$I_{d,ref}$	71.45 A
q-channel current reference	$I_{q,ref}$	0 A
Duty cycle d-channel	D_d	0.4695
Duty cycle q-channel	D_q	0.0128
Proportional gain, current controller	K$_p$	0.016
Integral gain, current controller	K_i	0.1007
Proportional gain, PLL controller	$K_{p,pll}$	6.62
Integral gain, PLL Controller	$K_{i,pll}$	7151

Table G.2: Parameters used in the base-case for this thesis.

Appendix H

Adaptive Control Fundamentals

In line with the objectives and scope of this thesis, and the work methodology presented in Chapter 3, this thesis aims to implement an adaptive control system. This appendix will aim at explaining some fundamental background theory to highlight why the choices taken in this thesis are like they are. Furthermore, at the end of the appendix, the presented theory will be applied to the system under study in this thesis,

The area of Adaptive control has grown to be one of the biggest fields on the control when it comes to algorithms, design techniques, analytical tools, and modifications [36]. This Appendix will in no way try to cover this topic, but merely serve as an introduction to some concepts, and how they can be relevant for this thesis. For a complete guide, [36] and [37] are books that cover the topic of adaptive control in great depth.

First of all, the term *adaptive control* has to be defined, to separate adaptive control and a non-adaptive control. A possible way to separate the two is:

A non-adaptive controller is based solely on a priori information whereas an adaptive controller is based also on a-posteriori information [35].

This definition is also what is to be expected from the word adaptive, something is done after new information is obtained. In other words, an adaptive control system can change the control law based on new information, while a non-adaptive control system does not. This means that for an adaptive controls system, relevant system parameters have to be estimated in real-time. therefore parameter estimation is a core topic in adaptive control.

Furthermore, there is a broad range of different categories of adaptive control techniques, and possibly the simplest form of adaptive control is called *gain scheduling*. The term involves the process of splitting up the dynamic system in operating point or intervals and having predefined actions for each operating point or interval. An example of this is having different levels of grid impedance that is estimated, at depending on the numerical value the control parameters of the converter are updated from a predefined lookup table. This was done in own previous work in [16]. The advantage of this method is its simplicity, but there are several downsides as well. Frequent changes of the controller gains can lead to instability, and also there is no adjustment mechanism of the controller gains as everything is predefined in the lookup table. Naturally, this depends on the nature of the plant and the application in general, but this technique is a popular method and used widely in the industry [36].

Other categories of methods include direct and indirect adaptive control, model reference adaptive control (MRAC), adaptive pole placement control (APPC) and many more, and also there is a distinction between SISO and MIMO adaptive control, but before any of these methods are further considered, it would be useful to examine what would be fitting for the system under study in this thesis.

As explained in the main part of this thesis, MIMO transfer function matrices are formed to model both the grid and the converter, which then can be used to form the minor loop gain $\mathbf{L}(\mathbf{s})$ and the closed-loop transfer function, $\mathbf{L_{cl}}(\mathbf{s})$. Available tools are online grid impedance estimates, so this is the parameter estimation part of the adaptive control. In total, four parameters can be changed based on the grid impedance estimate, namely the proportional and integral gain of the two PI controller. This means that the system dynamics can be examined for different levels of grid impedance and different control parameters to form the adaptive control law, whatever that might be. To not go into to much detail, as the rest of the discussion is covered in Chapter 3, a promising method to examine is to form a grid impedance intervals, and for each interval sweep over a large range of parameter value to get the optimal form of control. This can, for example, be measured with pole placement. To relate this to the methods mentioned earlier in this appendix that would be a mix of gain scheduling and adaptive pole placement.

Adaptive control can be done both incredibly theoretical and complex, but that completely depends on the mindset and purpose of the control system. In this thesis, pragmatism is put in front of all other concerns, both in line with the scope of the thesis and the control objective from Section 3.1. Therefore, if the reader comes from a control background, the theory part in Chapter 3 may seem incredibly informal and practical compared to standard literature on adaptive control methods. Also, the choice of critical pole tracking and correction may seem like a naive approach, which also includes loss of generality since there is no general control algorithm. However, once again this can be related to the control objective. When it comes to a loss of generality, further work could quite easily generalize the control approach in this thesis for other systems and other operating points. The method selected in this thesis is maybe the simplest way of achieving this control objective, and therefore it is done the way it is. Other adaptive control methods are also considered out of the scope of this thesis.

Appendix I

Modifications for Time-Domain Implementation

It turned out that time-domain implementation of the results from the two adaptive control methods was not straightforward. Therefore, some details about the Simulink model and necessary adjustments to the controllers will be presented here, to support the time-domain analysis in Section 4.3.

To verify that the results from the MIMO converter and grid models make sense, a complete switched converter model was developed in Simulink, based on own previous work in [16]. Figure I.1 shows the overall topology of the model.

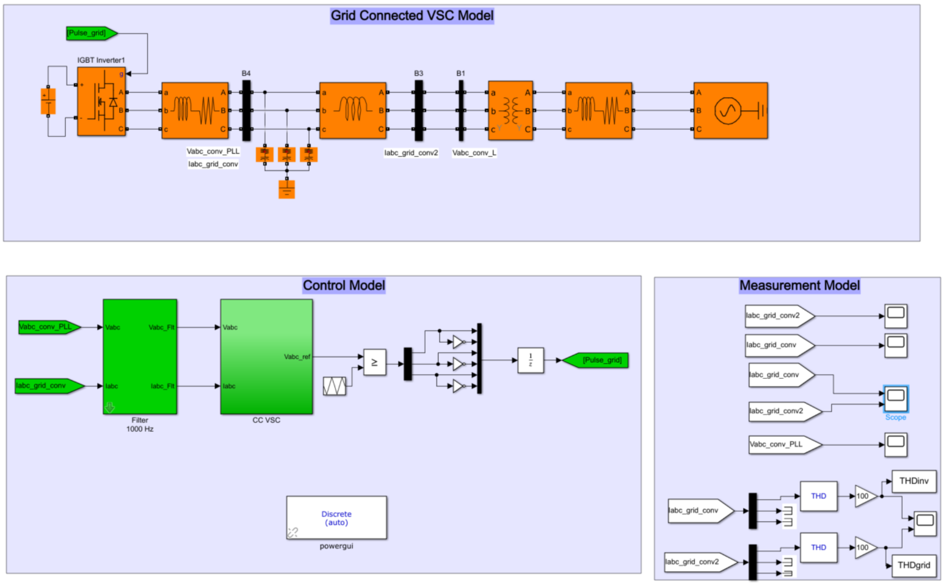

Figure I.1: Overview of Simulink converter-grid model.

Both the converter and the grid are exactly as described earlier in this thesis, with an LCL-filter and passive damping in the form of damping resistors in series with the filter capacitor. The converter is connected to the grid via a transformer. In accordance with the rest of this thesis, the current is measured before the v_0 node, and here the voltage also is measured. These two measurements are used in the control model, and inside the block called "CC VSC" the actual dq-current control takes place, and the output of this controller is the inverter terminal voltage reference, which is compared to the carrier wave to create the PWM signals that are applied at the six transistor gates. The measurements after the LCL-filter, seen from the converter, are just for measurement and plotting purposes.

In the rest of this thesis, there was no concern whether to have a per-unit control system or not, as both should work fine, and it is not interesting which one of them is used. In the MIMO converter model, a not-per-unit control system was used. It was decided when the Simulink model was created that it would be more useful to have the control system in per-unit, to compare to previous own work in a similar model, but also because it was generally easier to implement a per-unit control system versus a non-per-unit control system for the system in the figure above. The only challenge by doing this is that the gain schedules developed in the main part of this thesis cannot be used directly, and have to be converted to per-unit values. In general, this is not a problem, as there are ways to do this quite easily, by simply scaling the parameter values.

But even when this was done, it was difficult to get a direct translation between the numerical values derived from the two gain schedules to per-unit control parameters that made the system behave as expected earlier in this thesis. There could be many different reasons for this, and some of them will be discussed in Chapter 5, as it is pretty significant that the expected result from one model does not seem to fit very well in another model, but for now it is noted and accepted. So instead of trying to use the numerical values from the gain schedule directly, and then transfer them to per-unit control variables, it was decided to use the *trends* from the gain schedule instead. An example of a trend observed in the adaptive control method was that the PLL bandwidth decreased with increased grid inductance. The same trend was observed in the multivariable method. If this is taken one step further, the trend was that the multivariable method suggested a lower bandwidth than the adaptive method did. Another trend was that in general high current controller bandwidth increases the stability limit, but if it is too high, the dynamic performance at low grid inductance levels was very poor. To create control parameters that followed a certain trend, the original not-per-unit control variables was first scaled, and then some minor tweaks was applied. Naturally, the same scaling and tweaks was applied in all cases, to get comparable results.

Based on the comparison of the four different adaptive methods and three static methods in Section 4.2, four cases were selected for the time-domain implementation, based on the trends observed. First of all, a system that has the same trend as the multivariable method must be used, because it was shown that this produced nice dynamic performance over the full grid inductance range. The main trend in this method was that is started with moderate CC bandwidth and high PLL bandwidth, and then ended with minimum PLL bandwidth and maximum CC bandwidth. The second case of interest would be the original adaptive PLL controller, which has a static moderately high CC bandwidth, and a PLL that pushes the limit for how high PLL bandwidth is possible.

The last two cases were selected to be two static cases, one with the trend of balanced control parameters i.e. both moderately high CC and PLL bandwidths, and finally an aggressive static control with very high CC bandwidth and very low PLL bandwidth. The rationale behind this is that the balanced case is expected to perform well in the low grid inductance area, and later go unstable and that the aggressive static controller would generally have bad dynamic performance, but have a very high stability limit.

The goal of defining the four cases above like they are defined is naturally to link it to the analysis in Section 4.2, and hopefully observe the same trends. Therefore, also the three previously chosen grid inductance levels were chosen 0.1mH, 1.2 mH, and 2.5 mH. Also, a case of 5.0 mH was chosen as it is expected that at least on of the four cases, namely the balanced static case, would go unstable at this high grid inductance levels.

Therefore, when Section 4.3 presents a case as the ”multivariable method” or the ”adaptive PLL method”, there has been a significant translation between the original control parameters that were the output of the adaptive control algorithms, and the parameters used in the Simulink model. The numerical values are not interesting in itself, what is interesting is if the same trends from the MIMO modeling can be observed, to verify the methodology used in this thesis.

Appendix J

Grid Impedance Estimation Method

In Chapter 2, both SISO and MIMO stability criteria were derived based on converter and grid impedance. While converter modeling is straightforward, the grid impedance has to be estimated, because there is no straightforward way to measure it directly. As the estimation part itself is not the main objective in this thesis, as this has been done in previous master and Ph.D. work in [11], [10] for a similar laboratory setup, this appendix is kept brief. The appendix is based on own previous work in [16].

J.1 Overview of Grid Impedance Estimation Methods

There are several approaches to estimate the real-time impedance of the grid, which roughly can be divided in two, passive, and active methods [11]. Both methods are based on the idea that any perturbation in grid voltage will cause a response in grid current. By comparing the change in grid voltage and grid current, ΔV_g and ΔI_g, the grid impedance can be determined as $Z_g = \frac{\Delta V_g}{\Delta I_g}$.

J.1.1 Passive Methods

The passive methods used for estimating grid impedance utilize disturbances already present in the grid, i.e. no additional perturbations are added. Two methods commonly used are discussed in [29] and [30], and are called *Linear Regression Method* and *Error Function Method* respectively. The main advantage all passive methods have is that they are non-intrusive to the grid i.e. they do not disturb operation in any way. The methods are also quite simple. The main drawback is that these methods have proven to be ineffective under strong grid conditions, and therefore ineffective under small grid disturbances [31].

J.1.2 Active methods

Compared to the passive methods, the active methods actively inject signals to the grid to estimate the impedance. The signals could be either voltage or current signals. The two main categories are Transient Methods and Steady-State Methods [31].

Transient Methods

The transients methods inject transient signals into the grid to estimate the grid impedance. The goal is to estimate the grid impedance based on a few signal injections into the grid. There are several methods proposed, two of them being *Switching of Load* and *Pulse Injection*. The first method is based on switching a known load into the network and by the voltage and current transients estimate the impedance. The second method is based on injecting a known current or voltage pulse into the network. This can be done by the converter itself by manipulating the control system, or for example, by another parallel-connected VSC, injecting the signal [32].

Steady-State Methods

Compared to the transient methods, which inject few or sometimes a single signal to estimate the grid impedance, the steady-state methods inject repeated periodic perturbations. This includes methods such as *Sinusoidal Sweep*, *Exciting LCL filter Resonance*, *Switching of loads* and *Pseudo-Random Binary Sequences* [31].

Methods based on sinusoidal sweep inject sinusoidal signals of different frequencies for extended periods. This gives a very accurate estimate of the grid impedance, but takes very long evaluation times compared to other methods [31].

As discussed in Appendix B, the LCL-filter is a common way to connect the converter to the grid, which also is used in this thesis. One of the steady-state methods is based on injecting signals to excite the LCL filter and by that estimate the grid impedance. However, this method is limited to produce grid impedance estimates at the resonance frequency, and not a wider spectrum, which is a major disadvantage.

Switching of loads may also be used as a steady-state method, switching a load in and out, and observe the voltage and current changes.

The last group of methods described here is based on Pseudo-Random Binary Sequences (PRBS). The converter outputs a binary sequence to emulate white noise. This is a promising method, as it has low evaluation time, requires little to no extra hardware, it has multiple injection periods, low level of intrusion, and high signal-to-noise ratio [31].

Quasi-Passive Methods

A third possible approach is the Quasi-Passive methods, which are a combination of active and passive methods. They combine the advantages of the two methods and try to eliminate their weaknesses. As mentioned, both methods have drawbacks, the passive methods do not operate effectively under strong grid conditions, and the active methods are intrusive to the grid. A grid dominated by grid-connected converters that use active methods for grid estimation could lead to degradation of the power quality due to the injected perturbations.

By combining the two methods, and operating with passive methods in strong grid conditions and active methods in weak grid conditions (i.e. disturbances below a certain threshold), the weaknesses of both methods can be limited to a certain degree.

J.1.3 Comparison and Conclusion on Impedance Estimation

The different methods for estimating grid impedance described briefly in Section J.1.1 and J.1.2 each possesses advantages and disadvantages, and a comparison is necessary to find the best-suited method for an eventual laboratory implementation for the methods discussed in this thesis. In [11] and [31] and this was done for a similar laboratory setup. Therefore, the analysis done there is not repeated and referring to the scope of this thesis no detailed explanation for the choice of method will be provided. The comparison was made based on the four parameters below.

1. *Accuracy*. The selected method must provide an accurate estimate for a wide frequency range.
2. *Evaluation time*. The estimate must be evaluated in a short enough time to adapt to grid changes for ensuring the stable operation of the converter.
3. *Costs and modifications*. If the method selected method requires extra hardware or other costs, this will be a negative aspect.
4. *Ready to use capability*. Methods that possess ”plug-and-play” capabilities, i.e. suitable for operation in an unknown environment as the grid is.

The conclusion was that the PRBS, which is one of the active methods was best suited for the project, and this will be the method used in an eventual laboratory implementation for this thesis as well. Therefore a more detailed description of this specific method follows below.

J.2 Maximum Length Binary Sequence

There are several methods based on PRBS, and one of these is the Maximum Length Binary Sequence (MLBS) method. This is a commonly used method [8], and in recent years its use has become popular in a range of electronics applications [51]. Like all other PRBS methods, MLBS is a binary sequence. The sequence is deterministic, i.e. if the value of the current element is known, then all future element values are also known. The sequence also creates signals with an average close to zero, so the intrusion level in the grid is low. The method is not limited to a low-frequency spectrum such for example the sinusoidal sweep method because PRBS methods emulate white noise, and therefore cause excitation over a wide spectral range [31]. In [33] it was showed that the pulse injection method would require a bigger amplitude of the injected signal compared to MLBS to achieve the same accuracy. [8] shows that the MLBS method can be implemented in hardware with a feedback shift register circuit, which does not bring significantly extra costs or complexity. Based on this, the MLBS is a suitable method for this project due to its low intrusion level, flexibility to be implemented under any grid condition, low cost, and little added complexity.

As the name implies, the MLBS is a binary sequence, yielding an output of either 1 or 0. When the state is 1, the amplitude must be appropriately mapped to the application i.e. there is no general rule for the amplitude of the signal. The most common way to generate this sequence is by the use of linear feedback shift registers, which will be described later in this appendix. If the shift register has n bits, the length of the MLBS, N, is

$$N = 2^n - 1 \tag{J.1}$$

The sequence is also deterministic i.e. if the first element is known, all other elements are known as well. After the sequence is finished, it will start repeating itself. Another defining feature is that each combination will appear exactly one time in one complete sequence. Therefore, during a full sequence, the output will be $\frac{N-1}{2}$ in one state and $\frac{N+1}{2}$ in the other state. If then the amplitude of the signal is selected in such a way that it is symmetrical about zero, the average of a full sequence will be close to zero. This explains why the MLBS has such a low intrusion level to the grid as stated earlier in this appendix. To illustrate what this actually means with an example, consider the 4-bit shift register with XOR feedback in Figure J.1. The XOR, short for Exclusive OR, computes its output from Table J.1 of two inputs A and B. As table J.1 shows, the XOR outputs 0 if A and B is equal and 1 otherwise. The four blocks in Figure J.1 is each a memory unit passing the current value one step ahead, and stores the inputted value from the previous block for each time step. The first bit gets the value directly from the XOR function that takes the first and fourth bit and inputs.

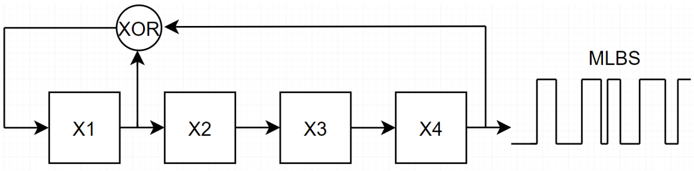

Figure J.1: 4-bit shift register with XOR feedback resulting in a 15 bit-length MLBS sequence.

A	B	Output
0	0	0
0	1	1
1	0	1
1	1	0

Table J.1: Input-output table of an XOR.

The initial memory value can be whatever as long as it is not (0,0,0,0). The reason for this becomes clear when considering the XOR function. If (0,0,0,0) is initially stored, the XOR will just keep on outputting 0, and no new values can be outputted. Below an example sequence is shown that demonstrates the key features of the MLBS. After $2^n - 1 = 15$ the sequence stats repeating itself, and the output is in state 0 $\frac{N-1}{2} = 7$ of the times and state 1 in $\frac{N+1}{2} = 8$ of the times. It also becomes clear that the only possible combination of states that does not occur is (0,0,0,0). Another important fact is that the average of the output closer to zero the longer the sequence is, so depending on the application it should be considered more than a four bit shift sequence.

The last thing to consider is the signal design with considerations for the application in mind. To guide this topic, a fundamental feature of the MLBS is related to the energy in the MLBS. In [11] it is stated that the MLBS has no energy at the generation frequency, f_{gen} and its multiples. Furthermore, the MLBS can only contain power at a certain type of frequencies. These frequencies are limited to

$$f = \frac{k}{T} = \frac{k}{P\Delta t_b} = \frac{k}{P} f_{gen} \tag{J.2}$$

where T is the period of a full sequence, Δt_b is the duration of one single pulse, k is all positive and negative integers (often called the spectral line number), and N is the length of the sequence, as before. Furthermore, this defines the power spectrum of the MLBS as [11]

$$\Phi_{MLBS}(f = \frac{k}{T}) = \frac{a^2(P+1)}{P^2} \frac{sin^2(\frac{\pi k}{P})}{(\frac{\pi k}{P})^2} \tag{J.3}$$

Timestep	**1**	**2**	**3**	**4**
1	1	1	1	1
2	0	1	1	1
3	1	0	1	1
4	0	1	0	1
5	1	0	1	0
6	1	1	0	1
7	0	1	1	0
8	0	0	1	1
9	1	0	0	1
10	0	1	0	0
11	0	0	1	0
12	0	0	0	1
13	1	0	0	0
14	1	1	0	0
15	1	1	1	0
1	1	1	1	1
2	0	1	1	1

Table J.2: Example output of a 4-bit shift register MLBS generator.

where a is the signal amplitude. Figure J.2 shows the power spectrum of the earlier example, which clearly shows that the energy of the MLBS is spread over the harmonics in a non-uniformly manner. In [51] it is stated that the excitation signal should have an approximately equal amount of energy at all frequencies where the system is to be identified. Figure J.2 clearly shows that this does not hold, but if the sequence is generated at a high enough frequency the spectrum can be considered flat. The part of the excitation signal that has not dropped by 3dB or more is thus considered as the *effective frequency band*. This band should cover the frequency band for the full system identification. In the application for this thesis, this is from around 1 Hz until about half the switching frequency, i.e 5000 Hz.

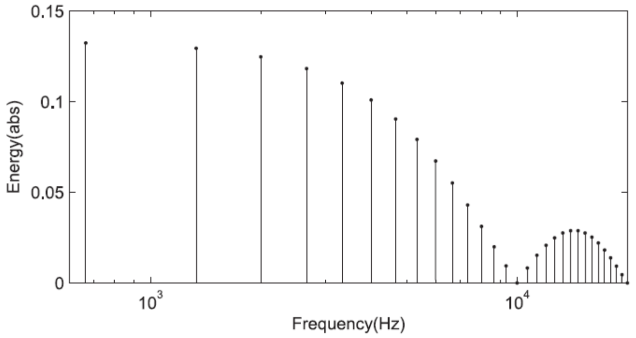

Figure J.2: Power spectrum of 15-bit length MLBS [51].

The three other design parameters are the length of on period N, the number of injection periods P, and the amplitude a. The period length should be selected based on the following rule:

$$N = 2^n - 1 \geq f_{gen}T \tag{J.4}$$

where T is the settling time of the system. This rule has to be followed for time aliasing reasons [51]. P can be selected based o the external noise in the system, i.e. experimentally, and finally, a should be selected based on the general rule that is should be low enough to avoid big effects but high enough to provide high enough Signal-to-Noise Ratio (SNR). Summed up, a general design procedure is listed below with an example at the end of the Appendix.

- Select f_{gen}. The upper limit is controller bandwidth
- Select N. Based on the expression in (J.4).
- Select P. It should be selected based on desired accuracy and memory limitations. Typically between 2-8.

Finally, some considerations should be taken for the application in this thesis. As reviewed in Section 2.3.1, the impedance is a 2x2 matrix, where four impedance elements have to be identified. A solution for this is to inject be pure d or q axis components, as these two signals will be original in the dq-domain, and the four elements of $\mathbf{Z_{g,dq}}$ can be identified. This can be handled practically in the current controlled VSC by adding the MLBS signals to the d and q axis current reference. This process is described in detail in [3].

In [51] two experiments was performed, one for weak grid and one for strong grids and their values are listed below in table J.3.

MLBS parameter	**Weak grid**	**Strong grid**
amplitude, a	0.1pu	0.1pu
length bit register, n	10	9
length MLBS, N	1023	511
Periods, P	5	5

Table J.3: Example of MLBS parameters from the literature.